2007

A COMMUNICATION LINK RELIABILITY STUDY FOR SMALL UNMANNED AERIAL VEHICLES

Alicia K. Mylin
University of Kentucky, akmyli0@engr.uky.edu

Recommended Citation

Mylin, Alicia K., "A COMMUNICATION LINK RELIABILITY STUDY FOR SMALL UNMANNED AERIAL VEHICLES" (2007). *University of Kentucky Master's Theses*. 483.
https://uknowledge.uky.edu/gradschool_theses/483

ABSTRACT OF THESIS

A COMMUNICATION LINK RELIABILITY STUDY FOR SMALL UNMANNED AERIAL VEHICLES

Dependable communication links for unmanned aerial vehicles (UAV) are crucial to operational reliability and mission success. This study is focused on evaluating the probability of successful communication links for small UAVs. A program based on the Friis Transmission Equation was developed to calculate the power received in a line-of-sight communication link. The program was used to evaluate the probability of success for a variety of flight paths.

KEYWORDS: Unmanned Aerial Vehicle, UAV, Communication Link,
Friis Transmission Equation, Reliability

Alicia K. Mylin

9/17/07

A COMMUNICATION LINK RELIABILITY STUDY FOR SMALL UNMANNED AERIAL VEHICLES

By

Alicia K. Mylin

William T. Smith

Director of Thesis

YuMing Zhang

Director of Graduate Studies

9/24/2007

RULES FOR USE OF THESES

Name	Date

THESIS

Alicia K. Mylin

The Graduate School

University of Kentucky

2007

A COMMUNICATION LINK RELIABILITY STUDY FOR SMALL UNMANNED AERIAL VEHICLES

THESIS

A thesis submitted in partial fulfillment
of the requirements for the degree of
Master of Science in Electrical Engineering
at the University of Kentucky

By
Alicia K. Mylin
Lexington, KY
Director: Dr. William T. Smith, Assistant Professor of Electrical Engineering
Lexington, KY
2007

ACKNOWLEDGEMENTS

I would like to thank my advisor, Dr. Bill Smith, for encouraging me to pursue my Master's degree and helping me to achieve that goal. I am very grateful for his patience and guidance while completing this study. I appreciate all his assistance during the editing process of this thesis.

Thanks to Dr. Stephen Gedney and Dr. Robert Adams for serving on my thesis committee. I would like to thank Dr. Suzanne Smith, Dr. Jamie Jacob, and Dr. Jim Lumpp for their assistance with this research. I would also like to thank William Fuqua for his expertise in the radio frequency arena. Thanks to Chong Luo for all of his advice.

I would like to acknowledge the Kentucky Science and Technology Corporation for funding this study. I would also like to thank Lexmark, Inc. and the Institute of Electrical and Electronic Engineers for sponsoring fellowships which funded my education. A 'thank you' is also due to Richard and Karen Hackney for supporting the BIG BLUE project through the Kentucky Space Grant Consortium.

I would like to thank my mother, my sister and her husband, and my brother for their support and encouragement. Special thanks must be given to my mother for doing everything she could to help me get a higher education. I appreciate all the help and encouragement from Mr. Steve Ellis. Thanks also to John for keeping me sane while I finished this thesis.

TABLE OF CONTENTS

LIST OF TABLES

LIST OF FIGURES

LIST OF FILES

thesis_akm.pdf	7.76 MB

CHAPTER 1 - INTRODUCTION

1.1 Background

The U.S. military has been developing unmanned aerial vehicles (UAV) since the 1950's. During the Vietnam War, an Air Force drone called *Lightning Bug* was used successfully for tactical reconnaissance, flying over 3,000 missions during the conflict. Defense spending was cut following the end of the Vietnam War, and UAV programs development slowed dramatically until the early 1980's. In 1982, Israeli forces used UAVs to track Syrian radar and missile sites in the Bekaa Valley, enabling manned aircraft and missiles to take out Syria's air defenses. Following this successful combat demonstration of Israeli UAVs, the U.S. bought some unmanned systems from Israel and started developing new programs. [1]

Today, the U.S. military has numerous UAV programs ranging from micro air vehicles (MAV) weighing less than one pound to aircraft weighing over 40,000 pounds [2]. Two programs on the high end of that spectrum, *Predator* and *Global Hawk*, have provided support in recent operations. *Predator* has not only flown numerous surveillance missions over Iraq, Bosnia, Kosovo, and Afghanistan, but was also used to track and attack Taliban and Al Qaeda forces [1] [3] [4]. Similarly, *Global Hawk* has logged many hours of high altitude flight in combat operations over Iraq and Afghanistan and provided 55% of the time-sensitive targeting against enemy air defenses during Operation Iraqi Freedom [1].

Unmanned aircraft systems (UAS) technology continues to mature under military development. Numerous large UAV programs currently exist and have demonstrated advanced capability. However, small UAV technology remains in the developmental stage, and has the potential for extensive military and commercial development during the next two decades.

The class of small UAVs is defined in [3] as follows:

a. *For UAVs designed to be employed by themselves – any UAV system where all system components (i.e. air vehicles, ground control/user interface element, and communication equipment) are fully transportable by foot-mobile troops*
b. *For UAVs designed to be employed from larger aircraft (manned or unmanned) – any UAV system where the air vehicle can be loaded on the larger aircraft without the use of mechanical loaders (i.e. - two man lift, etc.)*

Small UAVs can be further classified as mini UAVs or micro air vehicles (MAV). This study will focus on UAVs which fall under the former classification.

Current mini UAV programs of the U.S. military are briefly summarized in Table 1.1 to familiarize the reader with a few examples.

Table 1.1 Mini UAV Programs of U.S. Military [2]

	Weight [lbs]	Length [ft]	Wingspan [ft]	Ceiling [ft]	User Service
Dragon Eye	4.5	2.4	3.8	1,000	Marine Corps
FPASS	7	2.7	4.3	1,000	Air Force
Pointer	8.3	6	9	1,000	SOCOM, Air Force
Raven	4	3.4	4.3	1,000	Army, SOCOM, Air Force
Buster	10	3.42	4.13	10,000	Army
Silver Fox	20	4.8	7.8	16,000	Navy
ScanEagle	39.6	3.9	10	19,000	Marine Corps
Aerosonde	33	5.7	9.4	20,000	Navy

The *Pointer*, shown in Figure 1.1a, was used in the Gulf War and is currently employed by SOCOM in Afghanistan and Iraq. In addition, *Pointer* has been used in operations of the Drug Enforcement Agency and the National Guard. The *Raven*, shown in Figure 1.1c, and the *ScanEagle*, shown in Figure 1.1b, are both currently deployed in Iraq. [2]

In addition to the military development presented above, there are a growing number of companies who are introducing their own small UAVs into the market.

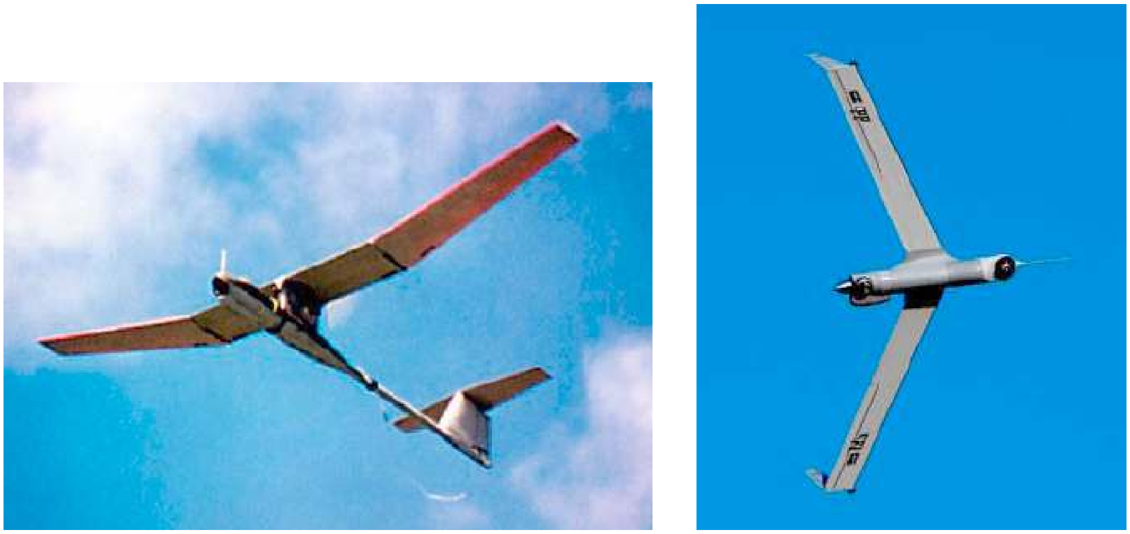

(a) Pointer, **© UAS Roadmap 2005**

(b) ScanEagle
© UAS Roadmap 2005

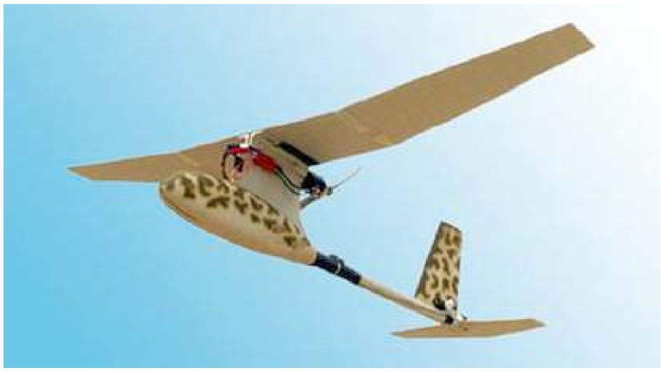

(c) Raven, **© UAS Roadmap 2005**

Figure 1.1: Mini UAVs of U.S. Military

1.2 Motivations

By virtue of their size, “small” UAVs offer flexibility in operational employment that larger, more logistically complex and intense UAVs do not [3]. There are many service requirements in both military and civilian spheres which could potentially be fulfilled by small UAVs. Mission applications of the military include the following [3]:

- Local security, reconnaissance and surveillance, and target acquisition for ground forces and Special Forces operations
- Perimeter security for individual naval vessels in foreign ports
- Local security for airfields, port complexes, and building operations
- Biological and chemical agent detection
- Precise bomb damage assessment
- Critical re-supply

The U.S. Department of Homeland Security (DHS) is investigating roles which unmanned aircraft (UA) could fulfill, and has identified the following functional capabilities in which UA are potential contributors [2]:

- Visual and non-visual monitoring
- Suspect/item geo-location
- Communications interception
- Tactical situational awareness
- Pursuit management and prevention
- Intelligence support to command
- Visible security systems
- Specialized enforcement operations
- Use of safety and emergency equipment

Two primary DHS organizations, Customs and Border Protection (CBP) and the Coast Guard, are conducting experiments with small UAVs to evaluate their utility for operations [2]. In addition, the UAV Collaborative demonstrated a small UAV providing airborne surveillance data as part of a Homeland Security scenario in which terrorist activity was simulated in an urban setting [5].

Small UAVs may also hold potential for civil and commercial uses, such as search and rescue operations, police patrol, and environmental, agricultural, or educational studies. For instance, Eisenbeiss [6] utilized a mini UAV helicopter system to demonstrate a photogram-metric flight over an ancient settlement near Palpa, Peru. Murphy *et al.* [7] presented the concept of a vertical take-off and landing (VTOL) small UAV sensor mobility system for support of law enforcement operations. Johnson *et al.* [8] demonstrated the use of a small UAV to collect digital RGB (red-green-blue) and hyperspectral imagery over vineyards for the purpose of crop vigor studies. Tindall [9] has proposed a small UAV platform for plant de-convolution remote sensing, which has applications for law enforcement, wildfire recovery, reservoir protection, and agriculture.

While small UAV technology has great potential, improvement of the reliability of small UAVs is necessary for successful operation in the capacities outlined in the preceding paragraphs. Dependable UAV communication links are crucial to operational reliability and mission success. Factors inherent to UAVs, such as sudden attitude changes and power limitations can lead to decreased signal strength, degraded signal quality, or complete loss of communication with the ground [3]. Additionally, communication links for small UAVs face special challenges because of the size, weight, and profile constraints on the system components (i.e. antennas, power source). The communication link must become more reliable to improve the overall operational reliability of small UAVs.

UAV communication links are generally either radio frequency (RF) or lasercom (optical). Both types currently suffer from bandwidth limitations. Data rates for RF links have traditionally been restricted due to limited spectrum and minimization of communication system size, weight, and power. Lasercom will potentially offer data rates two to five orders of magnitude greater than those of the best future RF systems [3]. Although lasercom could surpass RF in terms of airborne data transfer rate, RF will continue to dominate at the lower altitudes for some time into the future because of its better all-weather capability [3]. Additionally, RF links have the advantage of being much more efficient and usually much less complex than lasercom links [10].

1.3 Research Objective

The ultimate goal of this research is to evaluate the reliability of communication links for small UAVs. This study will focus on RF communication links based on the reasoning outlined in the preceding section. The particular objective of this thesis was to investigate the probability of success for the line-of-sight link between a small UAV and the ground station. To accomplish this goal, a computer program was developed to predict the probability of link success for planned flight paths.

1.4 Thesis Outline

This thesis consists of six chapters. Chapter One gave a brief background on UAV technology of the U.S. military, outlined the motivations for this research, and stated the research objective.

Chapter Two presents the theory from which the computer program was derived. The Friis Transmission Equation is introduced as the method of communication link analysis. The relevant antenna parameters are defined and the tools for performing the geometrical calculations are presented.

Chapter Three addresses the implementation of the computer program based upon the theory of Chapter Two.

Chapter Four describes the program algorithm, the flight path data, and the simulation data generated by the computer program.

Chapter Five discusses the probability of success predicted by the computer program.

The summary and conclusions of the study are presented in Chapter Six. Ideas for future study based on this work are also discussed.

CHAPTER 2 - THEORY

2.1 Introduction to Line-of-Sight Communication

Radio waves are a form of electromagnetic radiation with frequencies ranging from 3 kHz to 300 GHz. The main characteristics of the radio frequency spectrum are summarized in Table 2.1. The size and profile constraints of small UAVs cannot facilitate communication links on the low-frequency (large wavelength) end of the spectrum. Atmospheric attenuation as well as attenuation by rain, both exponential in character, becomes a serious limiting factor to the link distance in the millimeter wavelength region [11]. Due to these limitations, small UAV communication links are restricted to the very high frequency (VHF), the ultrahigh frequency (UHF), and the super-high frequency (SHF) bands.

The propagation characteristics of electromagnetic waves used in wireless channels are highly dependent on frequency [12]. Line-of-sight (LOS), which is a mode in which the electromagnetic wave propagates in a straight line, is the dominant propagation mode for frequencies above 30 MHz [12]. Therefore, the scope of this study will be restricted to communication links which have a direct LOS visibility between the aircraft and the ground station.

The following sections of this chapter cover a variety of topics related to analyzing general LOS communication links and airborne LOS links. These background sections are overviews of the various subjects.

Table 2.1 Radio Frequency Spectrum [12]

Band Designation	Frequency Band	Wavelength	Propagation Characteristics
Very low frequency (VLF)	3 – 30 kHz	100 km – 10 km	Ground wave; low attenuation day and night; high atmospheric noise level
Low frequency (LF)	30 – 300 kHz	10 km – 1 km	Similar to VLF, slightly less reliable; absorption in daytime
Medium frequency (MF)	300 – 3,000 kHz	1 km – 100 m	Ground wave and night sky wave; attenuation low at night and high in day; atmospheric noise
High frequency (HF)	3 – 30 MHz	100 m – 10 m	Ionospheric reflection varies with time of day, season, and frequency; low atmospheric noise at 30 MHz
Very high frequency (VHF)	30 – 300 MHz	10 m – 1 m	Nearly LOS propagation, with scattering because of temperature inversions; cosmic noise
Ultrahigh frequency (UHF)	0.3 – 3 GHz	1 m – 100 mm	LOS propagation; cosmic noise
Super-high frequency (SHF)	3 – 30 GHz	100 mm – 10 mm	LOS propagation; rainfall attenuation above 10 GHz, atmospheric attenuation because of oxygen and water vapor, high water vapor absorption at 22.2 GHz
Extremely high frequency (EHF)	30 – 300 GHz	10 mm – 1 mm	Same as SHF; high water vapor absorption at 183 GHz and oxygen absorption at 60 and 119 GHz

2.2 Friis Transmission Equation

The general LOS communication scenario is illustrated in Figure 2.1, where P_T is the power incident on the input terminals of the transmitting antenna and P_R is the power collected by the receiving antenna. The Friis Transmission Equation describes the power transferred in line-of-sight communication links. A derivation of this relationship can be found in [13]. A very general form of the Friis Transmission Equation is given by

$$P_R = \frac{P_T G_T\left(\theta_T,\phi_T\right) G_R(\theta_R,\phi_R)\lambda^2 \varepsilon_Z \varepsilon_P \varepsilon_A}{\left(4\pi R\right)^2} \tag{2.1}$$

where λ is the wavelength of the transmitted signal and R is the distance between the transmitting antenna and the receiving antenna. The gain of the transmitting antenna, G_T, is a function of the direction in which the antenna is pointing, given by the spherical angles θ_T and ϕ_T; and similarly for the receiving antenna gain G_R.

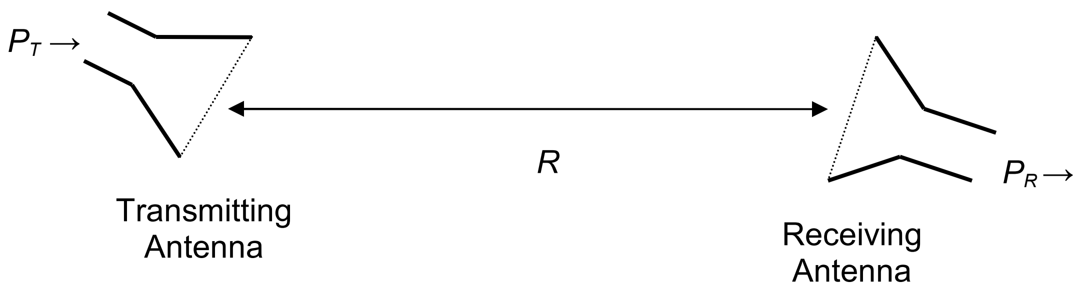

Figure 2.1: LOS Communication Link

Non-ideal conditions existing in the communication link are accounted for by the ε terms, which represent efficiencies having values ranging from zero to one ($0 \leq \varepsilon \leq 1$). The impedance mismatch factor ε_Z corrects for the power loss incurred from reflections on transmission lines connecting the antennas to the transceivers. The polarization efficiency ε_P accounts for discrepancies in the polarization of the antennas, including the angular dependence of the polarization of the transmitting and receiving antennas. Losses due to atmospheric attenuation of the signal are included by the attenuation factor ε_A. Additional efficiencies could be added for other propagation effects, but were not considered in this study.

2.3 Introduction to Antenna Theory

Antennas are required system components for mobile communications of all types, TV and radio broadcast, remote sensing applications such as radar and radiometry, and industrial applications such as cooking and drying with microwaves [14]. For wireless communication systems, the antenna is one of the most critical components, and a good antenna design can relax system requirements and improve system performance [13].

An antenna is a structure that has been designed to have a shape and size such that it will radiate electromagnetic power in an efficient manner [11]. Antennas are designed in a broad range of geometrical configurations and sizes, depending upon the intended use. While a large variety of models exist, antennas can be divided into four basic categories by their performance as a function of frequency: electrically small antennas, resonant antennas, broadband antennas, and aperture antennas [14].

The performance of antennas is described through evaluation of certain fundamental parameters. A detailed account of these parameters, which is beyond the scope of this study, can be found in [13]. The performance parameters which are of interest in this study are the radiation pattern, the directivity, the gain, and the polarization. Before these parameters can be defined precisely, it is necessary to introduce the concept of the antenna far field and define several radiation properties.

The space surrounding an antenna is usually subdivided into three regions [13]. The approximate boundaries between these regions are the distance from the antenna as a function of the antenna dimensions and wavelength of transmission. During normal operation, the distance from the antenna of interest usually surpasses the third boundary. This outer region of the surrounding space is generally referred to as the *far-field region*, and is defined as “that region of the field of an antenna where the angular field distribution is essentially independent of the distance from the antenna [13]”. In other words, at sufficiently large distances from an antenna, the radiated fields exhibit localized plane wave behavior.

The radiation intensity in a given direction is defined as “the power radiated from an antenna per unit solid angle” [13]. The radiation intensity *U* can be expressed in terms of the antenna’s electric field in the far-field zone as

$$U(\theta,\phi)=\frac{1}{2\eta}\left(\left|E_{\theta}^{ff}(\theta,\phi)\right|^{2}+\left|E_{\phi}^{ff}(\theta,\phi)\right|^{2}\right) \tag{2.2}$$

where E_{θ}^{ff} and E_{ϕ}^{ff} are the spherical components of the far-zone electric field and η is the intrinsic impedance of the medium.

The total power radiated by an antenna, P_{rad}, is found by integrating the radiation intensity U over a closed sphere, or complete solid angle of 4π steradians [13]. Therefore P_{rad} is given by

$$P_{rad}=\int_{0}^{2\pi}\int_{0}^{\pi}U(\theta,\phi)\sin\theta d\theta d\phi \tag{2.3}$$

The radiation pattern, directivity, gain, and polarization will now be defined. In addition, the theory for linear antenna arrays will be visited briefly, as it will be useful in the following chapter.

2.4 Radiation Pattern

An antenna radiation pattern is defined as “a mathematical function or graphical representation of the radiation properties of the antenna as a function of space coordinates”, which in most cases “is determined in the far-field region and is represented as a function of the directional coordinates” [13]. The far-field radiation pattern is generally normalized such that its maximum value is unity. The normalized radiation pattern is given by

$$F(\theta,\phi)=\frac{\left|E^{ff}(\theta,\phi)\right|}{\left|E^{ff}(\theta,\phi)\right|_{\max}} \tag{2.4}$$

where $\left|E^{ff}(\theta,\phi)\right|_{\max}$ is the maximum value of the magnitude of the far-zone electric field.

Radiation patterns are classified as isotropic or directional. The radiation is distributed equally in all directions in an isotropic pattern, which is purely hypothetical. Therefore, all real antennas have directional radiation patterns. A special case of the directional pattern is an omni-directional pattern, which is defined as one “having an essentially non-directional pattern in a given plane and a directional pattern in any orthogonal plane” [13]. An example of an omni-directional pattern is that of a half-wave dipole, which is shown in Figure 2.2.

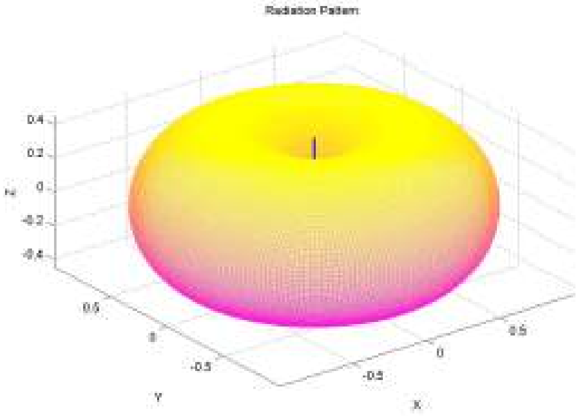

Figure 2.2: Half-wave Dipole Radiation Pattern

Antennas are often referred to based upon their radiation pattern characteristics. A broadside antenna is one for which the main beam maximum of the radiation pattern is in a direction normal to the plane containing the antenna [14]. An example of a broadside radiation pattern is shown in Figure 2.3a. An endfire antenna is one for which the main beam of the radiation pattern is in the plane containing the antenna [14]. Figure 2.3b illustrates an endfire radiation pattern.

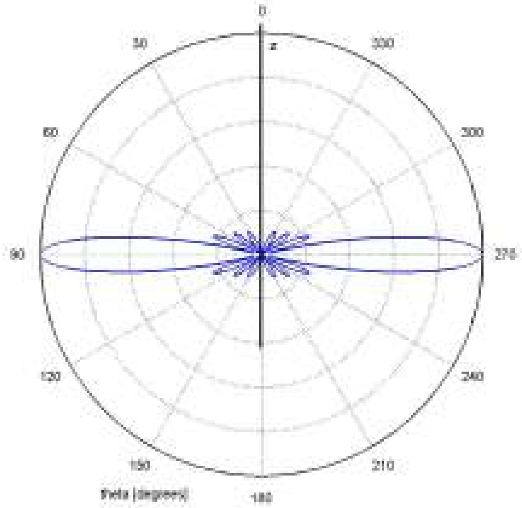

(a) Broadside

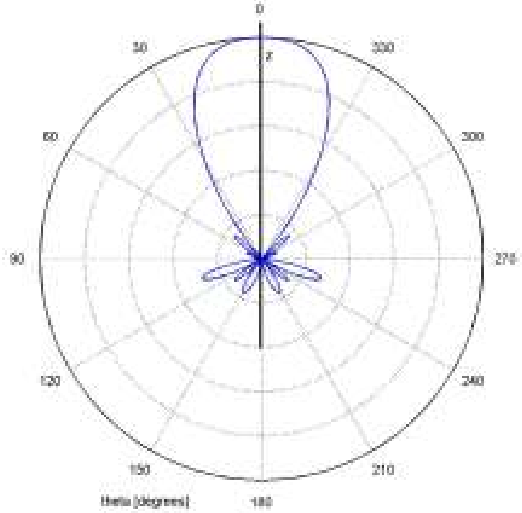

(b) Endfire

Figure 2.3: Polar Plots of Radiation Patterns (Antennas in plane of z-axis)

2.5 Directivity

Directivity describes how antennas focus energy in certain directions over others. The directivity of an antenna is defined as “the ratio of the radiation intensity in a given direction from the antenna to the radiation intensity averaged over all directions” [13]. The directivity can be expressed as

$$D(\theta,\phi) = 4\pi \frac{U(\theta,\phi)}{P_{rad}} \tag{2.5}$$

In addition, directivity is given by

$$D(\theta,\phi) = \frac{4\pi \left|F(\theta,\phi)\right|^2}{\Omega_A} = D\left|F(\theta,\phi)\right|^2 \tag{2.6}$$

where $D = \frac{4\pi}{\Omega_A}$ and the beam solid angle Ω_A is defined as

$$\Omega_A = \iint \left|F(\theta,\phi)\right|^2 d\Omega \tag{2.7}$$

where the element of solid angle $d\Omega = \sin\theta d\theta d\phi$.

2.6 Gain

The gain of an antenna compares the radiation intensity in a given direction to the radiation intensity of an isotropic source. Gain is a measure that takes into account the efficiency of the antenna as well as its directional capabilities [13]. It can be expressed in terms of the directivity as

$$G(\theta,\phi) = e_{cd} D(\theta,\phi) \tag{2.8}$$

where e_{cd} is the antenna radiation efficiency, which accounts for the conduction and dielectric losses in the antenna.

2.7 Polarization

Polarization is a description of the radiated electric field vector. The polarization of a radiated wave is defined as “that property of an electromagnetic wave describing the time varying direction and relative magnitude of the electric-field vector; specifically, the figure traced as a function of time by the extremity of the vector at a fixed location in space, and the sense in which it is traced, as observed along the direction of propagation” [15]. The tip of the instantaneous electric field vector will trace out a straight line, a circle, or an ellipse as time progresses. Thus polarization is classified as linear, circular, or elliptical, as illustrated in Figure 2.4.

The polarization of an antenna is the polarization of the wave radiated in a given direction by the antenna when transmitting [14]. The fields radiated by antennas of finite dimensions are spherical waves, but in the far field the waves appear locally as plane waves [13]. The polarization of antennas is a description of the local plane wave. Normally, the polarization of an antenna is specified as the polarization of the main beam maximum. But in practice, the polarization of the radiated energy varies with the direction from the center of the antenna, so that different parts of the pattern may have different polarizations [13].

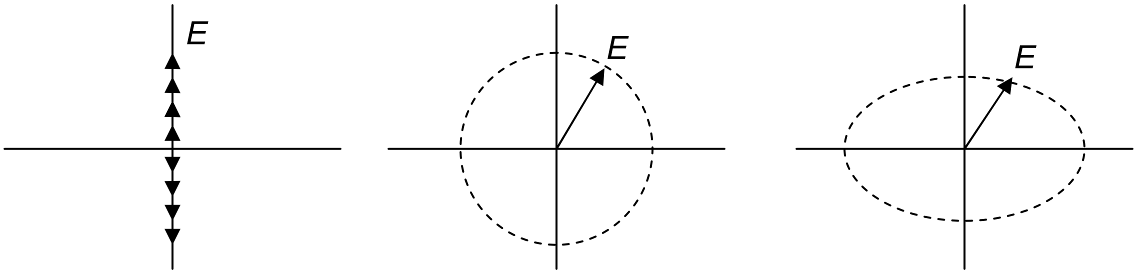

(a) Linear (vertical) (b) Circular (c) Elliptical

Figure 2.4: Wave Polarization

2.8 Polarization Efficiency

In general, the polarization of the receiving antenna will not be the same as the polarization of the incident wave, so the amount of power extracted by the antenna from the incident wave will not be the maximum [13]. The power loss due to polarization mismatch can be accounted for by defining a polarization efficiency.

The far-zone field radiated by an antenna with current I_{in} in its terminals can be written as [13]

$$\vec{E}^{ff} = -j\eta\beta I_{in}\frac{e^{-j\beta r}}{4\pi r}\left[\hat{\theta}l_{\theta}(\theta,\phi)+\hat{\phi}l_{\phi}(\theta,\phi)\right] \tag{2.9}$$

where l_{θ} and l_{ϕ} are complex. The field of (2.9) can also be expressed as

$$\vec{E}^{ff} = -j\eta\beta I_{in}\frac{e^{-j\beta r}}{4\pi r}\sqrt{\left|l_{\theta}\right|^{2}+\left|l_{\phi}\right|^{2}}\,\hat{e} \tag{2.10}$$

where $\hat{e}$ is the *unit polarization vector* given by

$$\hat{e} = \frac{l_{\theta}(\theta,\phi)}{\sqrt{\left|l_{\theta}\right|^{2}+\left|l_{\phi}\right|^{2}}}\hat{\theta}+\frac{l_{\phi}(\theta,\phi)}{\sqrt{\left|l_{\theta}\right|^{2}+\left|l_{\phi}\right|^{2}}}\hat{\phi} \tag{2.11}$$

Note that this unit vector can be complex.

The polarization efficiency is defined as

$$\varepsilon_{P} = \left|\hat{e}_{t}\cdot\hat{e}_{r}^{*}\right|^{2} \tag{2.12}$$

where $\hat{e}_{t}$ is the unit polarization vector of a wave radiated by the transmitting antenna and $\hat{e}_{r}$ is the unit polarization vector of a wave radiated by the receiving antenna. The complex conjugate of $\hat{e}_{r}$ is used in (2.12) because the receiving mode of the antenna is needed, and the polarization vector is by definition for the transmitting mode. The polarization efficiency varies from zero to unity as the incoming wave and receiving antenna vary from completely mismatched in polarization to completely matched [14]. The receiving antenna and the incident wave are said to be *co-polarized* when their polarization states are identical, and the receiving antenna will extract maximum power from the incident wave. When the receiving antenna and the incident wave are completely mismatched, they are said to be *cross-polarized*.

2.9 Linear Array Theory

An antenna array is formed by arranging several antenna elements in space and interconnecting them to produce a directional radiation pattern. The simplest array configuration is linear, where the antenna element centers lie along a straight line. An example of an N-element linear array of identical antenna elements is shown in Figure 2.5. Linear arrays are used widely in practice and their operating principles can be used to understand more complex array geometries [14].

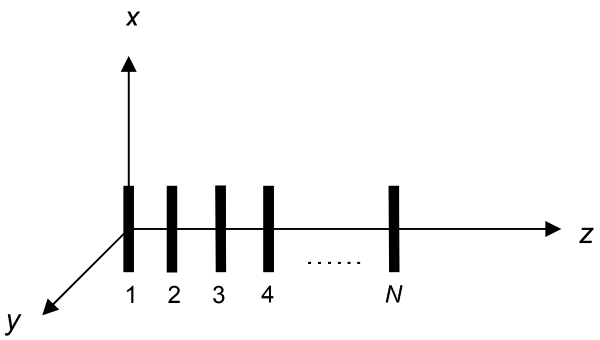

Figure 2.5: N-element Linear Array

The radiation pattern of an antenna array is found through the principle of pattern multiplication, which states that “the electric field pattern of an array consisting of similar elements is the product of the pattern of one of the elements and the pattern of an array of isotropic point sources with the same locations, relative amplitudes, and phases as the original array” [14]. The radiation pattern of an individual antenna element is referred to as the element pattern and the radiation pattern of the array of isotropic point sources is called the array factor.

The array factor of a linear array, such as that shown in Figure 2.5, is found by substituting an isotropic radiator with an equivalent excitation for each antenna element. An isotropic radiator, also called a point source, is a hypothetical, lossless antenna occupying a point in space and when transmitting radiates uniformly in all directions [14]. To find the array factor, it is assumed that the array is operating in the receiving mode. However, according to the principle of reciprocity, the result is also valid for the transmitting mode [13].

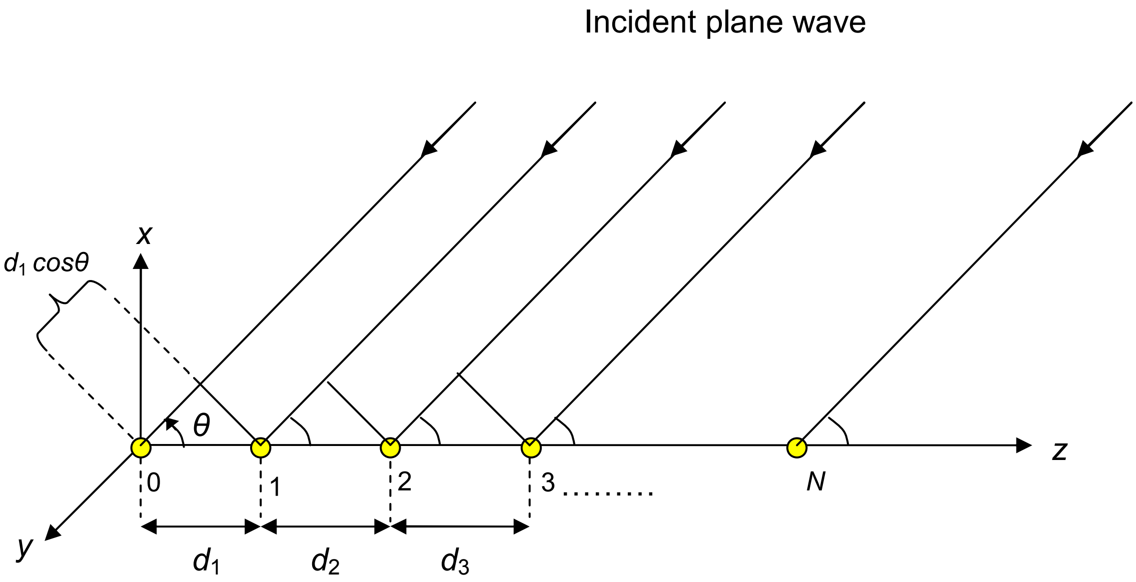

Figure 2.6: Array of Point Sources

The array of point sources in Figure 2.6 is receiving a plane wave at an angle of θ from the z-axis, and d is the separation between adjacent point sources. For simplicity, the wavefront arriving at the origin will be the reference and the excitation phase on that point source will be set to zero. The point sources one through N will have a phase shift corresponding to the distance between the reference wavefront and the point source. The phase shift of point source one is

$\beta d_1 \cos\theta$, as shown in Figure 2.6. The radiated fields of a point source located at the origin of a spherical coordinate system are proportional as

$$E \propto \frac{e^{-j\beta r}}{4\pi r} I_o \tag{2.13}$$

where I_o is the source current at the feed location. For dipole antennas, the feed location is typically at the center.

The array factor is a summation of the fields of the individual point sources. The fields of the individual elements are a product of the excitation from the plane waves and any source current connected to the elements (not shown in Figure 2.6). The array factor for an array represented by Figure 2.6 is given by

$$AF = I_0 + I_1 e^{j\beta d_1 \cos\theta} + I_2 e^{j\beta(d_1+d_2)\cos\theta} + I_3 e^{j\beta(d_1+d_2+d_3)\cos\theta} + ... \tag{2.14}$$

where I_N represents the complex source current of element *N*.

2.10 Geodesy

Geodesy is the study of the shape and gravity field of the earth [16]. One of the applications of geometrical geodesy is the determination of the coordinates of points on or near the earth's surface. In order to perform such calculations, a model must be adopted to approximate the shape of the earth.

2.10.1 Earth Models

The particular equipotential surface chosen to represent the shape of the earth is the *geoid*, a surface that, at sea, corresponds to within about 1-2 meters to the time-averaged ocean surface [16]. However, the geoid is unsuitable as a mathematical model for computations because it is defined by an infinite number of parameters [17]. A much simpler mathematical figure, the *ellipsoid of revolution*, has been adopted to model the figure of the earth in order to perform calculations. Because of mass excesses and deficiencies within the earth, the shape of the geoid is irregular and the ellipsoid of revolution which most nearly approximates the geoid must be found [17]. In other words, the ellipsoid of revolution is a mathematically simple approximation of the geoid, which is itself an approximation of the physical surface of the earth.

The ellipsoid of revolution, generally referred to simply as the ellipsoid, is produced by rotating an ellipse about its minor axis, with the major axis generating the equatorial plane [17]. An ellipse is shown in Figure 2.7. The major axis *EE′* has a length of *2a* and the minor axis *PP′* has a length of *2b*. Half of the major axis, *a*, is referred to as the semimajor axis, and half of the minor axis, *b*, is called the semiminor axis. The points *F* and *F′* are called foci, and they are the points of intersection on the major axis made by a circle with radius *a* and center *P* or *P′*.

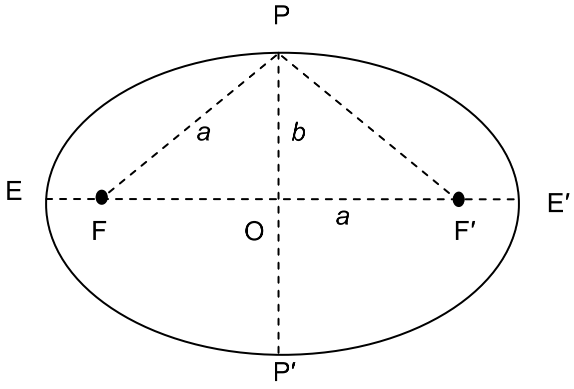

Figure 2.7: Ellipse

An ellipse has five principal parameters, but only two are needed to define the ellipse, provided one of these is linear [17]. The principal parameters of an ellipse are the semimajor axis *a*, the semiminor axis *b*, the flattening *f*, the first eccentricity *e*, and the second eccentricity *e′*. The second eccentricity is seldom used and will not be defined here. The flattening and the semimajor axis are almost universally used to define the ellipsoid [17]. The flattening of the ellipse is defined as

$$f = \frac{a-b}{a} = 1 - \frac{b}{a} \tag{2.15}$$

The first eccentricity of the ellipse is defined as

$$e = \frac{OF}{OE} = \frac{\sqrt{a^2 - b^2}}{a} \tag{2.16}$$

For practical purposes of a computational nature, the square of the eccentricity is used, or [17]

$$e^2 = \frac{a^2 - b^2}{a^2} = 1 - \frac{b^2}{a^2} \tag{2.17}$$

Ideally, the ellipsoid approximates the shape of the entire earth [17]. However, for certain applications it may be desirable to achieve a more precise fit for a particular region. Consequently, many different ellipsoids of revolution have been defined and are used in different parts of the world.

A geodetic datum is comprised of an ellipsoid of revolution fixed in some manner to the physical earth [17]. In general, geodetic datums may be classified as regional or global. A regional datum is used to achieve a more precise fit to the geoid in some local region. Here, the ellipsoid center may be offset from the center of the earth and the ellipsoid is then fixed to the surface at some point in the region [17]. In contrast, a global datum is comprised of an ellipsoid approximating the shape of the entire global geoid and having its origin at the earth’s center of gravity [17].

2.10.2 World Geodetic System WGS-84

The World Geodetic System, developed by the U.S. Department of Defense, is a geocentric system that provides a basic reference frame and geometric figure for the earth and the means for relating positions on various datums to an earth-centered, earth fixed coordinate system [18]. The definition of the World Geodetic System was last refined in 1984, and is commonly referred to as WGS-84. The WGS-84 represents the best global geodetic reference system for the earth available at this time for practical applications of mapping, charting, geopositioning, and navigation [19]. The Global Positioning System (GPS) uses WGS-84 as the reference to perform position calculations.

The WGS-84 ellipsoid is a geocentric equipotential ellipsoid of revolution which is defined as an equipotential surface with a specific theoretical gravity potential [19]. The theoretical gravity potential for the WGS-84 ellipsoid is uniquely determined using the four independent constants of Table 2-2. Several derived constants of interest are listed in Table 2-3.

Table 2.2 Defining parameters for WGS-84 Ellipsoid [19]

Parameter	Notation	Value
Semimajor axis	a	6378137.0 m
Reciprocal of flattening	$1/f$	298.257223563
Angular velocity of the earth	ω	$7292115.0 \times 10^{-11}$ rad/s
Earth's gravitational constant	GM	$3986004.418 \times 10^{8}$ m^3/s^2

Table 2.3 Derived Geometric Constants for WGS-84 Ellipsoid [19]

Constant	Notation	Value
Semiminor axis	b	6356752.3142 m
First eccentricity	e	$8.1819190842622 \times 10^{-2}$
First eccentricity squared	e^2	$6.69437999014 \times 10^{-3}$
Axis ratio	$\frac{b}{a}$	0.996647189335

2.11 Frames

It is impossible to calculate the position of objects in space without a frame of reference. Certain reference frames may be better suited for specific applications than others. Several useful coordinate systems are introduced in this section.

2.11.1 WGS-84 Coordinate System

The WGS-84 coordinate system, shown in Figure 2.8, is a right-handed, Earth-fixed orthogonal system [19]. It is an example of a world coordinate system. The system origin and axes are defined in [19] as follows:

- Origin = Earth's center of mass
- *Z*-axis = the direction of the IERS Reference Pole (IRP)
- *X*-axis = intersection of the IERS Reference Meridian (IRM) and the plane passing through the origin and normal to the *Z*-axis
- *Y*-axis = completes a right-handed, Earth-Centered Earth-Fixed (ECEF) orthogonal coordinate system

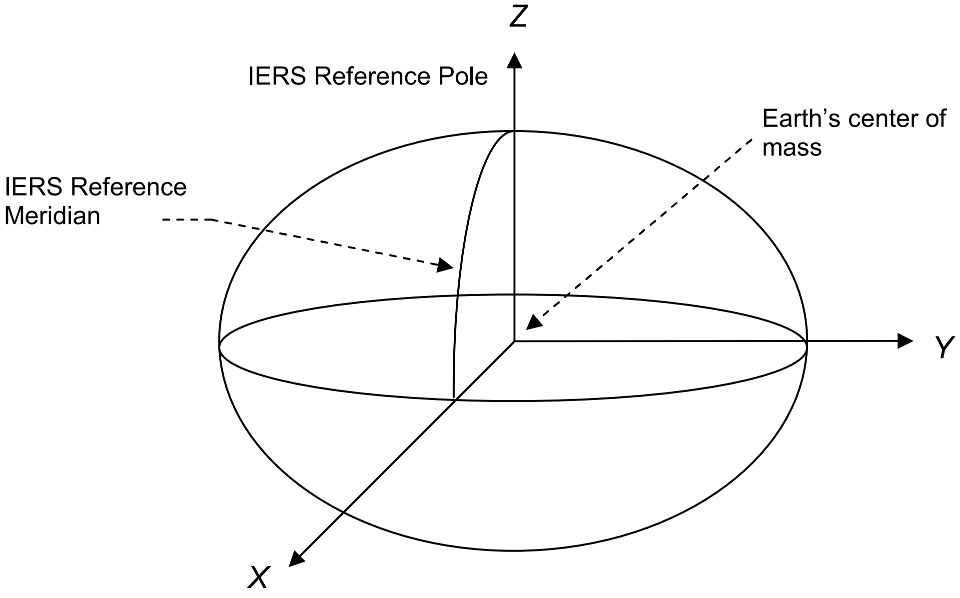

Figure 2.8: WGS-84 Coordinate System

2.11.2 Geodetic Coordinate Systems and Curvilinear Coordinates

Each datum requires its own geodetic coordinate system. An example of a geodetic coordinate system *uvw* along with a world coordinate system *xyz* is shown in Figure 2.9. Geodetic coordinate systems are defined in [20] as follows:

- Origin : at the center of the reference ellipsoid used for defining the datum in question
- *w*-axis: coincides with the semiminor axis of the reference ellipsoid
- *u*-axis: passes through the point where the geodetic latitude and longitude are both equal to zero
- *v*-axis: forms a right-handed triad with the *u*-axis and *w*-axis

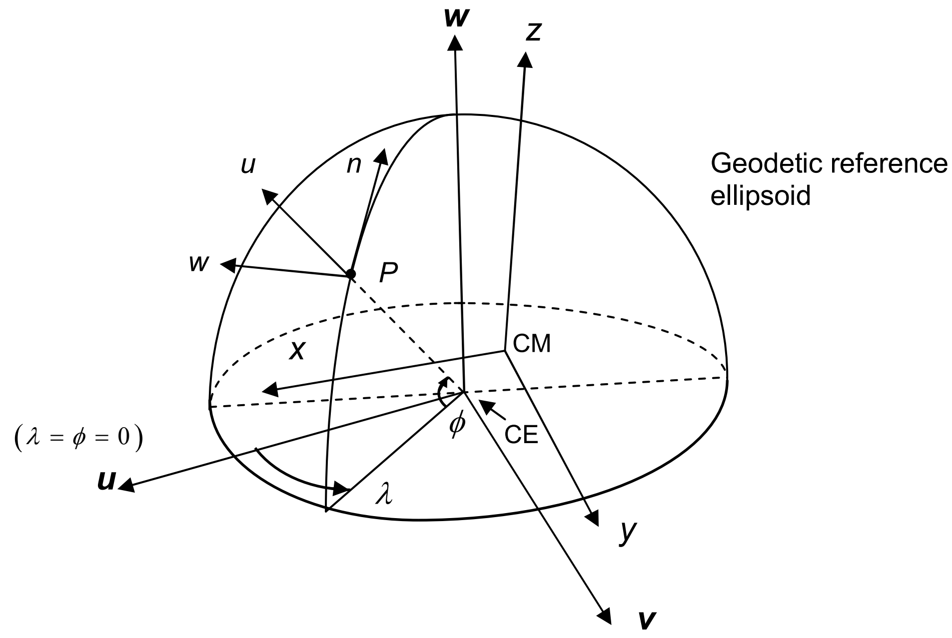

Figure 2.9: Geodetic, World, and *NWU* Frames

When dealing with a figure such as an ellipsoid, it is sometimes convenient to use curvilinear coordinates instead of rectangular. The set of curvilinear coordinates (λ, ϕ, h) denoting point *P* are illustrated in Figure 2.9 (note that the geodetic height h is zero in this example). The curvilinear coordinates are defined for a point *P* in [20] as follows:

- Geodetic longitude (λ): the angle between the *uw* plane and the geodetic meridian plane of *P*, usually measured positive in a right-handed sense; $0 \le \lambda \le 2\pi$
- Geodetic latitude (ϕ): the angle between the normal to the ellipsoid at *P* and the *uv* plane; $-\frac{\pi}{2} \le \phi \le \frac{\pi}{2}$
- Geodetic height (h): the distance along the normal to the reference ellipsoid between *P* and the surface of this ellipsoid

2.11.3 North-West-Up Coordinate System

The north-west-up frame is a local geodetic frame, meaning its origin is located at a point of observation. This coordinate system is useful to represent objects on the earth's surface which are not undergoing any translational motion with respect to the earth (i.e. they are free to rotate). Figure 2.9 includes an example of a *NWU* frame. It can be defined following from [20] as

- Origin: any point *P*(λ, ϕ, h) referred to a given ellipsoid
- *u*-axis: normal through *P* to the reference ellipsoid, positive in the outward, or geodetic zenith direction
- *w*-axis: normal to *u* and to the geodetic meridian plane, positive in the direction of decreasing longitude
- *n*-axis: perpendicular to *w* and *u* forming a right-handed triad, positive in the direction of increasing latitude

2.11.4 North-East-Down Coordinate System

The north-east-down frame is also a local geodetic frame. It is useful to represent objects which are moving freely with respect to the earth, such as an aircraft. An example of the *NED* frame is shown in Figure 2.10 below. The definition follows directly from that of the *NWU* coordinate system as

- Origin: any point *P*(λ, ϕ, h) referred to a given ellipsoid
- *d*-axis: normal through *P* to the reference ellipsoid, positive in the inward direction (opposite to geodetic zenith direction)
- *e*-axis: normal to *u* and to the geodetic meridian plane, positive in the direction of increasing longitude
- *n*-axis: perpendicular to *e* and *d* forming a right-handed triad, positive in the direction of increasing latitude

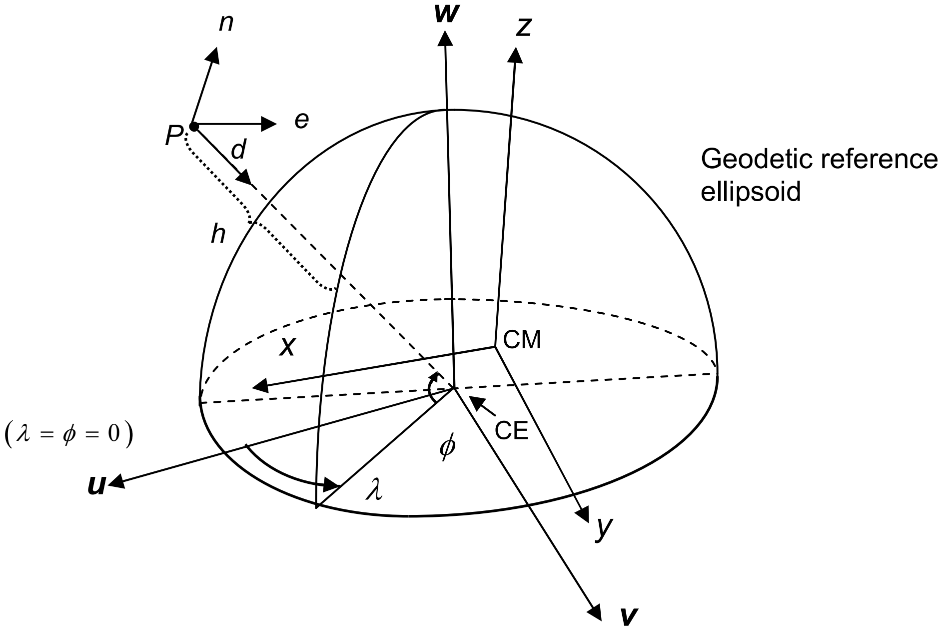

Figure 2.10: Geodetic, World, and *NED* Frames

2.11.5 Body-fixed Frame

A body-fixed frame is used to describe the motion of a rigid body relative to the earth. The origin and axes of this type of frame are fixed with respect to the geometry of the body. A common application of this type of frame is an aircraft. The origin of the body frame is the center of gravity (CG) of the aircraft [21]. A convenient right-handed, orthogonal system is shown in Figure 2.11. Here, the positive *x*-axis, or longitudinal axis, points outward through the nose of the airplane. The positive *z*-axis is directed downward through the bottom of the fuselage [20]. The positive *y*-axis, or transverse axis, is orthogonal to the *x*- and *y*-axes and proceeds roughly along the right wing (as viewed when facing from the tail towards the nose).

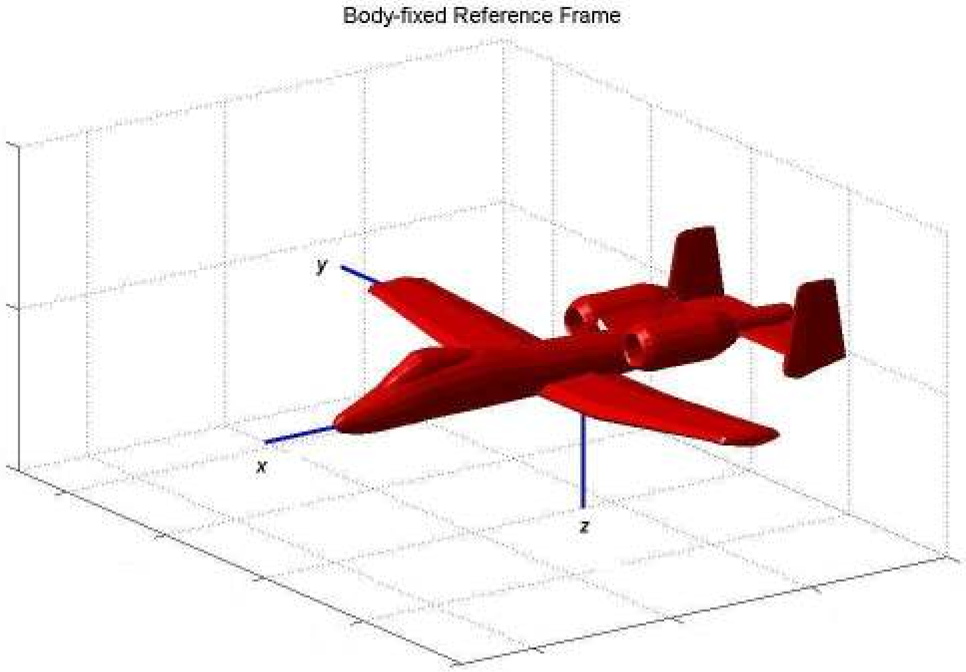

Figure 2.11: Body-fixed Frame

2.12 Euler Angles

A rigid body has three translational and three rotational degrees of freedom. Any motion of any complete body can be resolved into these six degrees of freedom [21]. Here, the rotational motion only will be considered. According to Euler's rotation theorem, any rotation may be described using three angles which are referred to as Euler angles [23]. In other words, a set of three Euler angles is used to specify the orientation of a rigid body.

An individual Euler angle specifies a rotation of the rigid body about a given axis of a coordinate system through a rotation matrix. Since matrix multiplication is not commutative, the order of rotations is a variable. Depending upon the rotation sequence, there are twelve different sets of Euler angles. The rotation sequences are usually denoted by the digits one through three, as shown in Table 2-4. The 321 and 323 sets will be introduced here. The angles are defined as positive according to the right-hand rule for right-handed coordinate systems.

Table 2.4 Euler Angle Sequences

Sequence	Axes	Sequence	Axes	Sequence	Axes
123	x-y-z	212	y-x-y	312	z-x-y
121	x-y-x	213	y-x-z	313	z-x-z
131	x-z-x	231	y-z-x	321	z-y-x
132	x-z-y	232	y-z-y	323	z-y-z

2.12.1 Z-Y-X Set

This sequence of Euler angles has been widely employed in aeronautical engineering and analysis of space vehicles [22]. The set will be defined as the angles which specify the orientation of the *xyz* coordinate system relative to the fixed *XYZ* frame. The system is defined in [22] as follows:

1) A positive rotation of ψ_e about the *Z*-axis, resulting in *x′y′z′*

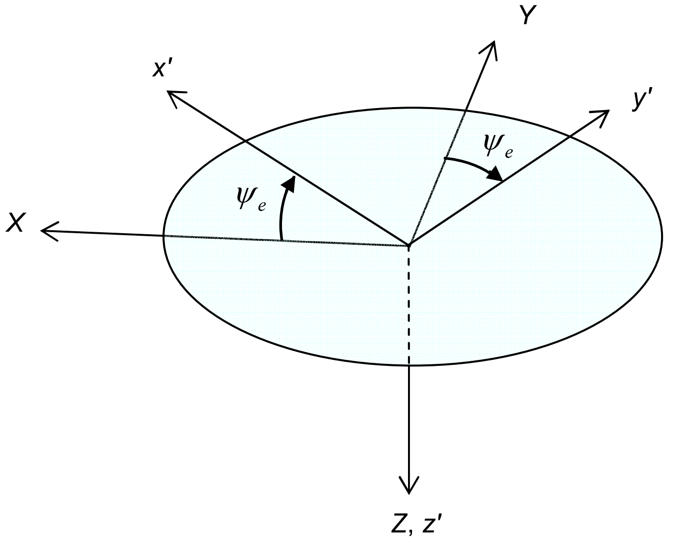

Figure 2.12: Rotation by ψ_e

2) A positive rotation of θ_e about the *y′*-axis, resulting in *x″y″z″*

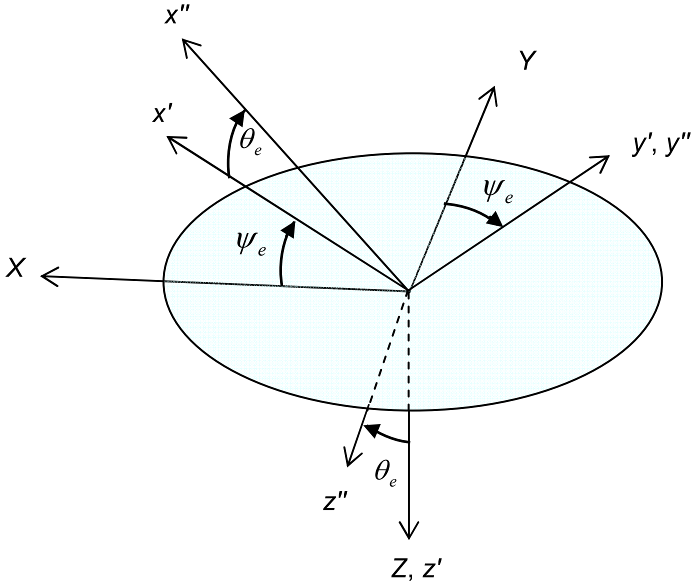

Figure 2.13: Rotation by θ_e

3) A positive rotation of ϕ_e about the *x″*-axis, resulting in *xyz*

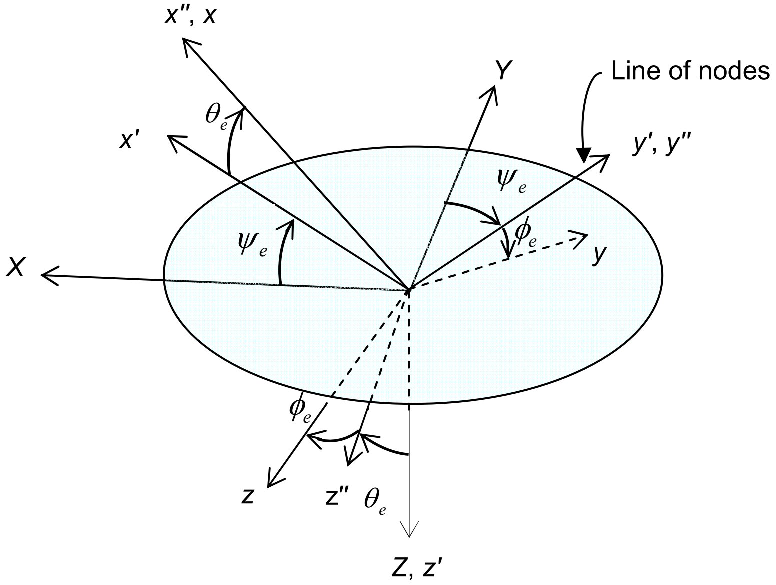

Figure 2.14: Rotation by ϕ_e

The series of rotations is progressively illustrated in Figures 2.12 – 2.14. The axis about which the θ_e rotation occurs (*y′* axis) is known as the *line of nodes*, as shown in Figure 2.14 [22]. The matrix equations which indicate the series of rotations are as follows:

$$\begin{pmatrix} x' \\ y' \\ z' \end{pmatrix} = \begin{bmatrix} \cos\psi_e & \sin\psi_e & 0 \\ -\sin\psi_e & \cos\psi_e & 0 \\ 0 & 0 & 1 \end{bmatrix} \begin{pmatrix} X \\ Y \\ Z \end{pmatrix} \tag{2.18}$$

$$\begin{pmatrix} x'' \\ y'' \\ z'' \end{pmatrix} = \begin{bmatrix} \cos\theta_e & 0 & -\sin\theta_e \\ 0 & 1 & 0 \\ \sin\theta_e & 0 & \cos\theta_e \end{bmatrix} \begin{pmatrix} x' \\ y' \\ z' \end{pmatrix} \tag{2.19}$$

$$\begin{pmatrix} x \\ y \\ z \end{pmatrix} = \begin{bmatrix} 1 & 0 & 0 \\ 0 & \cos\phi_e & \sin\phi_e \\ 0 & -\sin\phi_e & \cos\phi_e \end{bmatrix} \begin{pmatrix} x'' \\ y'' \\ z'' \end{pmatrix} \tag{2.20}$$

The Euler angles are limited to the range $0 \le \psi_e \prec 2\pi$, $-\frac{\pi}{2} \le \theta_e \le \frac{\pi}{2}$, $0 \le \phi_e \prec 2\pi$.

As mentioned previously, the Z-Y-X Euler set is widely used in aerospace. When applied to represent the orientation of an aircraft in space, the Euler angles can be considered as rotations from a reference frame fixed in space at the CG to a body-fixed coordinate system (as in Section 2.11.5). The angles are generally referred to as follows:

- ψ_e, or a rotation about the *z*-axis, is called the yaw angle
- θ_e, or a rotation about the *y*-axis, is called the pitch angle
- ϕ_e, or a rotation about the *x*-axis, is called the roll angle

Figure 2.15 shows the direction of positive rotation for the angles about the axes of a reference frame fixed in space.

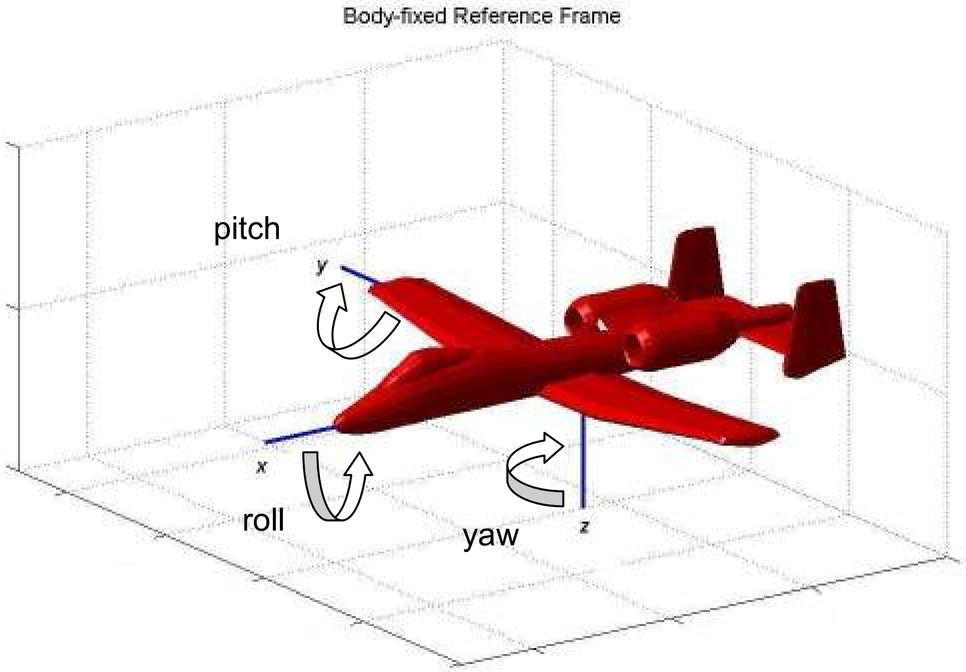

Figure 2.15: Rotations

A yaw rotation of 10° is shown in Figure 2.16 and a pitch rotation of 10° is shown in Figure 2.17.

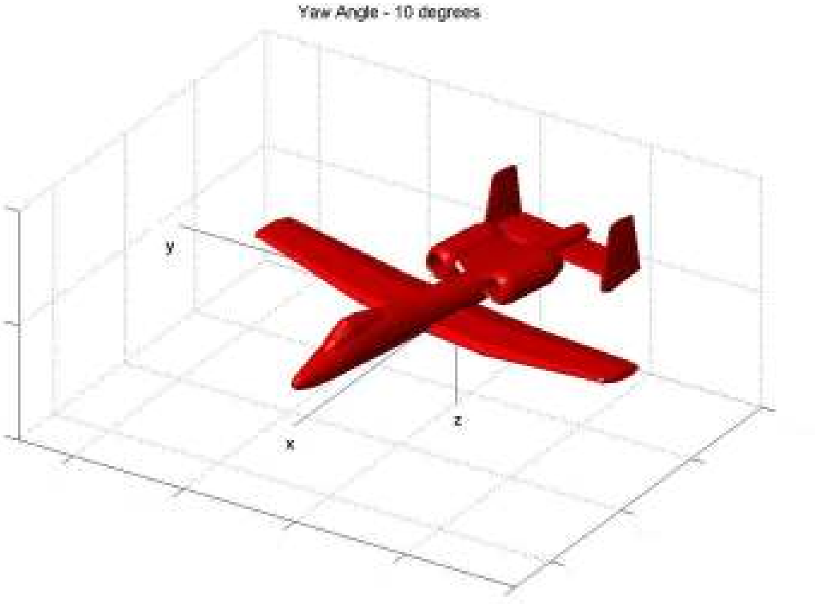

Figure 2.16: Yaw Rotation

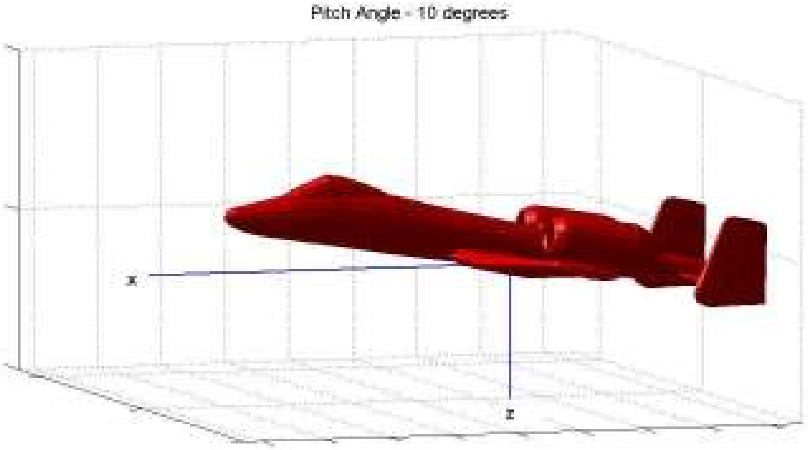

Figure 2.17: Pitch Rotation

A roll rotation of 10° is shown in Figure 2.18 below.

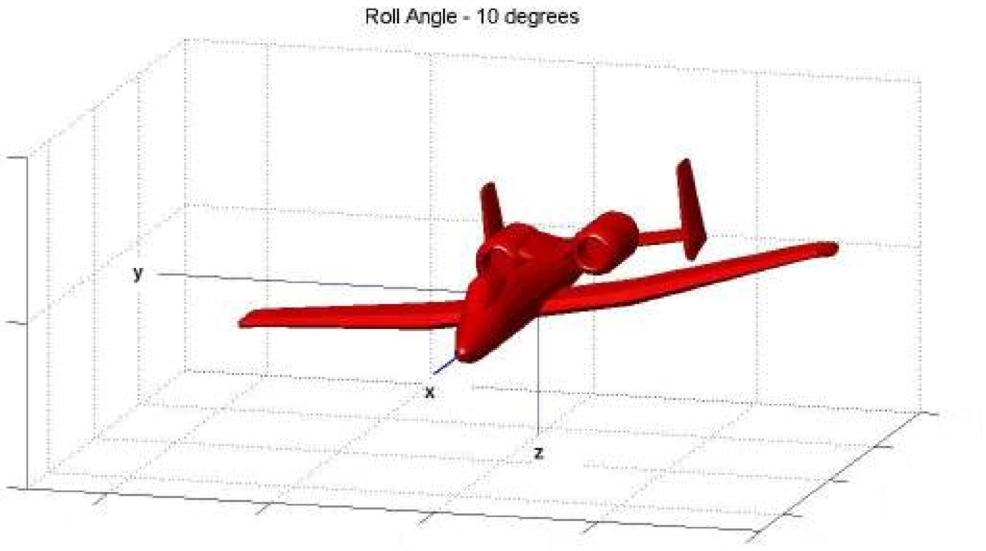

Figure 2.18: Roll Rotation

The matrix equations of (2.18)-(2.20) can be combined into one, yielding

$$\begin{pmatrix} x \\ y \\ z \end{pmatrix} = \begin{bmatrix} 1 & 0 & 0 \\ 0 & \cos\phi_e & \sin\phi_e \\ 0 & -\sin\phi_e & \cos\phi_e \end{bmatrix} \begin{bmatrix} \cos\theta_e & 0 & -\sin\theta_e \\ 0 & 1 & 0 \\ \sin\theta_e & 0 & \cos\theta_e \end{bmatrix} \begin{bmatrix} \cos\psi_e & \sin\psi_e & 0 \\ -\sin\psi_e & \cos\psi_e & 0 \\ 0 & 0 & 1 \end{bmatrix} \begin{pmatrix} X \\ Y \\ Z \end{pmatrix} \quad (2.21)$$

To simplify the notation, (2.21) can be written as

$$\begin{pmatrix} x \\ y \\ z \end{pmatrix} = \left[A\left(\psi_e, \theta_e, \phi_e\right) \right] \begin{pmatrix} X \\ Y \\ Z \end{pmatrix} \quad (2.22)$$

where $\left[A\left(\psi_e,\theta_e,\phi_e\right)\right]$ denotes the combined rotation matrix.

2.12.2 Z-Y-Z Set

The definition for the Z-Y-Z sequence of Euler angles follows naturally from that of the Z-Y-X set. The series of rotations, shown in Figure 2.19, is as follows:

1) A positive rotation of α about the *Z*-axis, resulting in *x'y'z'*
2) A positive rotation of β about the *y'*-axis, resulting in *x''y''z''*
3) A positive rotation of γ about the *z''*-axis, resulting in *xyz*

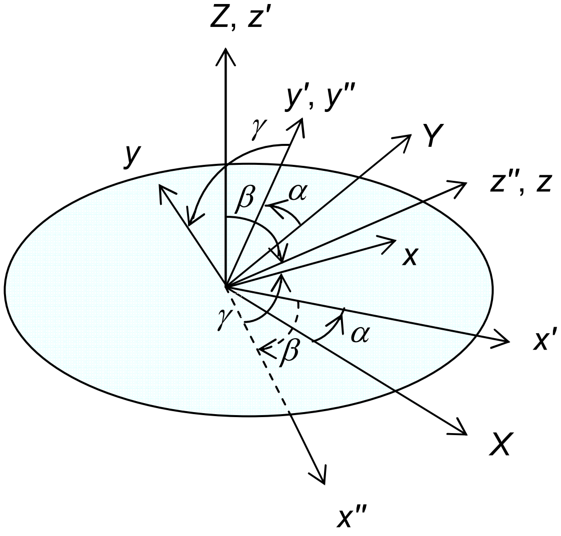

Figure 2.19: ZYZ Rotations

The matrix equations which indicate the series of rotations are given by

$$\begin{pmatrix} x' \\ y' \\ z' \end{pmatrix} = \begin{bmatrix} \cos\alpha & \sin\alpha & 0 \\ -\sin\alpha & \cos\alpha & 0 \\ 0 & 0 & 1 \end{bmatrix} \begin{pmatrix} X \\ Y \\ Z \end{pmatrix} \tag{2.23}$$

$$\begin{pmatrix} x'' \\ y'' \\ z'' \end{pmatrix} = \begin{bmatrix} \cos\beta & 0 & -\sin\beta \\ 0 & 1 & 0 \\ \sin\beta & 0 & \cos\beta \end{bmatrix} \begin{pmatrix} x' \\ y' \\ z' \end{pmatrix} \tag{2.24}$$

$$\begin{pmatrix} x \\ y \\ z \end{pmatrix} = \begin{bmatrix} \cos\gamma & \sin\gamma & 0 \\ -\sin\gamma & \cos\gamma & 0 \\ 0 & 0 & 1 \end{bmatrix} \begin{pmatrix} x'' \\ y'' \\ z'' \end{pmatrix} \tag{2.25}$$

The matrix equations of (2.23)-(2.25) can be combined to yield

$$\begin{pmatrix} x \\ y \\ z \end{pmatrix} = \begin{bmatrix} \cos\gamma & \sin\gamma & 0 \\ -\sin\gamma & \cos\gamma & 0 \\ 0 & 0 & 1 \end{bmatrix} \begin{bmatrix} \cos\beta & 0 & -\sin\beta \\ 0 & 1 & 0 \\ \sin\beta & 0 & \cos\beta \end{bmatrix} \begin{bmatrix} \cos\alpha & \sin\alpha & 0 \\ -\sin\alpha & \cos\alpha & 0 \\ 0 & 0 & 1 \end{bmatrix} \begin{pmatrix} X \\ Y \\ Z \end{pmatrix} \tag{2.26}$$

The simplified form of (2.26) is

$$\begin{pmatrix} x \\ y \\ z \end{pmatrix} = \left[A(\alpha, \beta, \gamma) \right] \begin{pmatrix} X \\ Y \\ Z \end{pmatrix} \tag{2.27}$$

where $\left[A(\alpha, \beta, \gamma) \right]$ denotes the combined rotation matrix.

CHAPTER 3 - IMPLEMENTATION

3.1 Overview of Problem

The general flight scenario consists of the ground station and the UAV, as shown in Figure 3.1 below. The ground station includes the autopilot interface and the communication link antenna. Here it is assumed that both the autopilot interface and the autopilot avionics (airborne) obtain position information through built-in Global Positioning System (GPS) receivers.

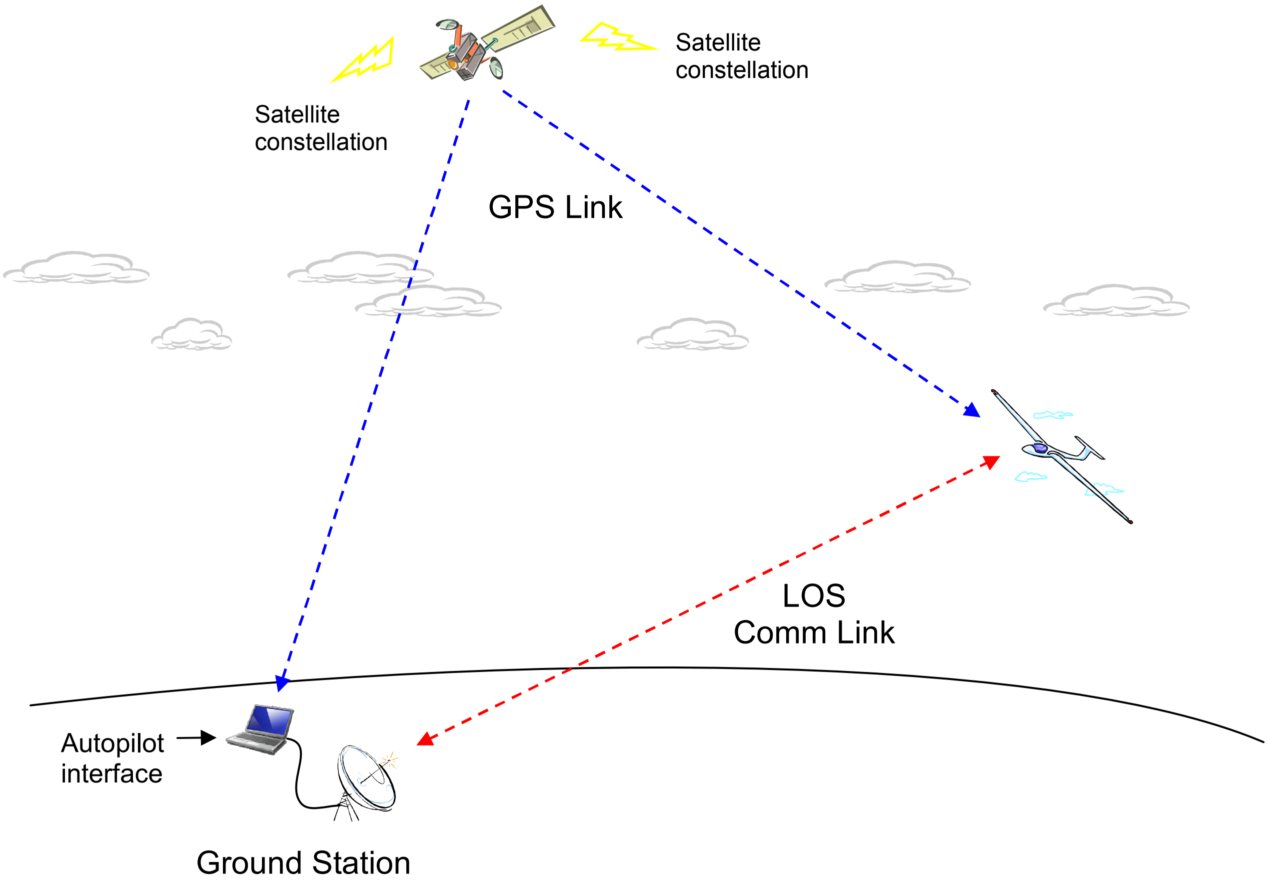

Figure 3.1: Flight Scenario

In order to analyze the LOS communication link, reference frames will be assigned to the autopilot interface, the UAV, the ground station antenna, and the UAV antenna. This is illustrated in Figure 3.2, where the necessary coordinate systems are denoted as follows:

- Ground station autopilot interface: $x^o y^o z^o$
- Ground station antenna: $x^{gs} y^{gs} z^{gs}$
- UAV: $x^u y^u z^u$
- UAV antenna: $x^a y^a z^a$

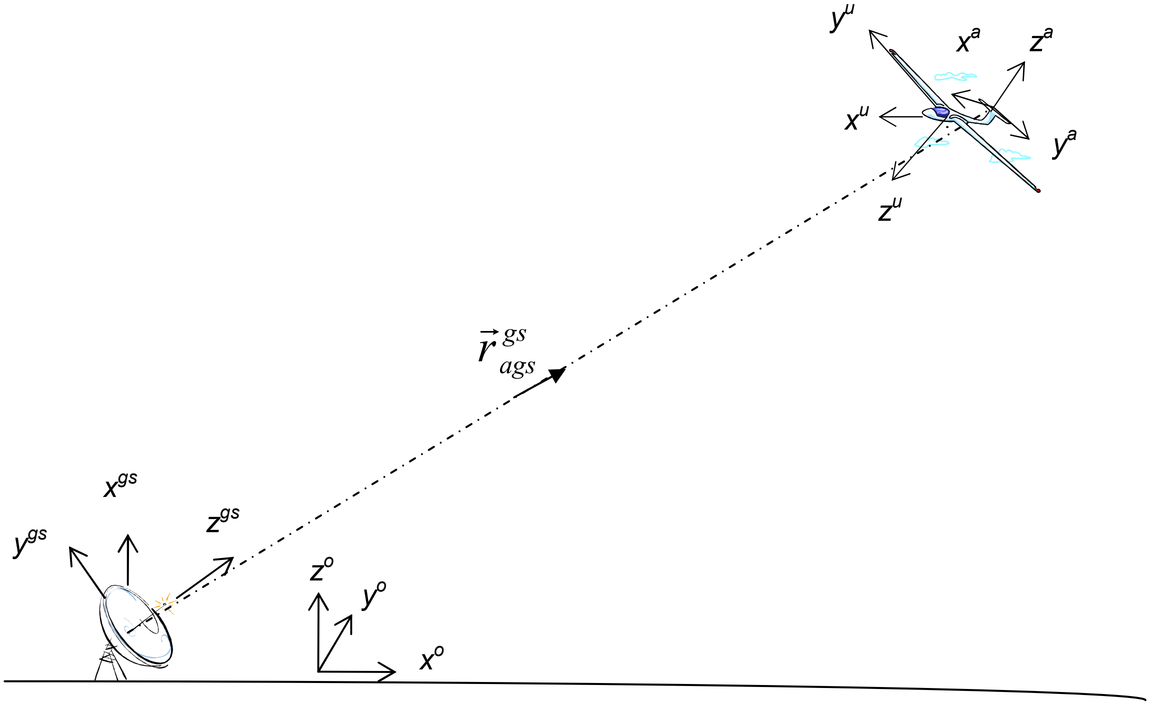

Figure 3.2: Communication Scheme

The Friis Transmission Equation introduced in Section 2.2 describes the power transferred in this LOS link. In order to evaluate (2.1), the vector between the ground station antenna and the UAV antenna ($\vec{r}^{gs}_{ags}$) must be calculated. All geometry-dependent variables of (2.1) can be derived from this vector.

3.2 Autopilot System

The Piccolo II Autopilot from Cloud Cap Technology is a complete integrated avionics system for small unmanned aircraft which consists of the avionics hardware and software and the ground station hardware and software [24]. The autopilot system data link operates on the UHF band, and is used for command and control, autopilot telemetry, and payload data transfer functions. All the telemetry from the avionics is automatically logged by the ground station for future reference. To analyze the LOS communication link, data giving the position of the ground station and UAV is needed. In addition, the orientation of the UAV in space must be known.

3.2.1 GPS Position

The avionics and the ground station autopilot interface each obtain measurements of position from integrated Motorola M12 GPS receivers. The GPS position data is in the form of curvilinear coordinates (i.e. latitude, longitude, height) and is in reference to the WGS-84 datum.

3.2.2 Aircraft Orientation

The aircraft orientation is described by the attitude data, which gives the estimated Euler angles (yaw, pitch, and roll) for the vehicle obtained by Kalman-filtering the rate gyro outputs and correcting the outputs using the attitude derived from GPS and other sensors [24]. The Euler angle readings are with respect to the avionics reference frame. Since the avionics has 3-axis gyros and accelerometers it can be installed in any orientation and the readings rotated to match the installation angles [24]. The natural installation for the avionics is according to English aircraft conventions, with the *x*-axis pointing through the nose, the *y*-axis out the right wing tip, and the *z*-axis pointing down [24]. The Euler angles logged are in reference to the body-fixed frame introduced in Section 2.11.5, which follows the English aircraft convention mentioned above.

3.3 Geometrical Calculations

The geometrical analysis of the flight scenario is presented here. A method for calculating the link range and the antenna pointing angles is given.

3.3.1 Coordinate Systems

The coordinate systems for the implementation are detailed here.

- $x^o y^o z^o$: the north-west-up frame defined in Section 2.11.3 was chosen to represent the ground station autopilot interface, with the origin located at the GPS position of the interface.
- $x^u y^u z^u$: the body-fixed frame defined in Section 2.11.5 was used to represent the UAV, with the origin located at the GPS position of the CG.
- $x^{gs} y^{gs} z^{gs}$: the ground station antenna was represented by a standard orthonormal Cartesian coordinate system. The axes are considered as fixed with respect to the antenna geometry.
- $x^a y^a z^a$: the UAV antenna was represented by a standard orthonormal Cartesian coordinate system. The axes are considered as fixed with respect to the antenna geometry.

3.3.2 Coordinate System Transformations

The transformations between the coordinate systems of Section 3.3.1 are given by the Euler angle matrices of Section 2.12. The individual and combined rotation matrices are all orthogonal matrices, so the inverse transformations may be obtained by transposing the corresponding matrices [22]. The rotation matrices will be denoted here as $\left[{}^{y}A^{x}\right]$, where the rotation is from frame *x* to frame *y*.

The ground station antenna frame is fixed with respect to the antenna geometry. If the ground station antenna has a unidirectional radiation pattern, such as a Yagi antenna, the antenna must be free to rotate in azimuth and elevation in order to track the UAV in flight. The initial orientation of the frame is defined relative to the $x^{o}y^{o}z^{o}$ frame by a Z-Y-Z set of Euler angles. The orientation of the frame at time *t* is determined by a rotation through the antenna azimuth and elevation angles. Then a vector in the $x^{gs}y^{gs}z^{gs}$ frame can be expressed as

$$\begin{pmatrix} x \\ y \\ z \end{pmatrix}^{gs} = \left[{}^{gs}A^{o}\right]\begin{pmatrix} x \\ y \\ z \end{pmatrix}^{o} \tag{3.1}$$

where the rotation matrix is given by

$$\left[{}^{gs}A^{o}\right] = \left[A(az,el)\right]\cdot\left[A(\alpha,\beta,\gamma)\right] \tag{3.2}$$

The antenna azimuth and elevation angles are defined relative to the antenna coordinate system. The Euler angle rotation sequence is then chosen to correspond with the azimuth and elevation angles. The rotation matrix $\left[A(az,el)\right]$ is then given by a sequence of two rotations about axes which are determined by the antenna coordinate system.

The UAV frame is body-fixed. The orientation of the frame is dependent upon the yaw, pitch, and roll angles measured by the autopilot avionics. The orientation of the frame is determined relative to the $x^o y^o z^o$ frame by a two-step rotation. The first rotation is from the $x^o y^o z^o$ frame to the *NED* frame, which represents the UAV parallel to the local horizon with the nose pointing in the direction of north. The *NED* frame is then rotated through the Euler angles (Z-Y-X set) measured by the autopilot avionics. Therefore, a vector in the $x^u y^u z^u$ frame can be expressed as

$$\begin{pmatrix} x \\ y \\ z \end{pmatrix}^u = \left[{}^u A^o \right] \begin{pmatrix} x \\ y \\ z \end{pmatrix}^o \tag{3.3}$$

where the rotation matrix is given by

$$\left[{}^u A^o \right] = \left[A\left(\psi_e, \theta_e, \phi_e\right) \right] \cdot \left[{}^{NED} A^o \right] \tag{3.4}$$

The definition of the rotation matrix $\left[{}^{NED} A^o \right]$ will follow from the transformation presented in Section 3.3.3.

The UAV antenna frame is fixed with respect to the antenna geometry and the aircraft body. The orientation of the frame is defined in reference to the UAV frame by the orientation in which the antenna is installed, and is given by a Z-Y-Z set of Euler angles. A vector in the $x^a y^a z^a$ frame can be expressed as

$$\begin{pmatrix} x \\ y \\ z \end{pmatrix}^a = \left[{}^a A^u \right] \begin{pmatrix} x \\ y \\ z \end{pmatrix}^u \tag{3.5}$$

where the rotation matrix is given by

$$\left[{}^a A^u \right] = \left[A\left(\alpha, \beta, \gamma\right) \right] \tag{3.6}$$

3.3.3 Transformation of Position Coordinates

GPS position data must be converted from curvilinear coordinates (i.e. latitude, longitude, height) to Cartesian coordinates in order to calculate the necessary vectors. In general, the curvilinear coordinates would be converted to Cartesian coordinates in a geodetic coordinate system *uvw* and then transformed to a world coordinate system *xyz*. However, the geodetic coordinate system and the world coordinate system $XYZ_{WGS\text{-}84}$ of the WGS-84 datum are coincident. Therefore, the GPS position data may be converted directly from curvilinear coordinates to Cartesian coordinates in the WGS-84 world coordinate system. The curvilinear and Cartesian coordinates of the GPS position are illustrated in Figure 3.3 below. The curvilinear to Cartesian conversion is given by

$$\begin{pmatrix} x \\ y \\ z \end{pmatrix}^{WGS-84} = \begin{pmatrix} (N+h)\cos\phi\cos\lambda \\ (N+h)\cos\phi\sin\lambda \\ \left(\frac{b^2}{a^2}N+h\right)\sin\phi \end{pmatrix} \tag{3.7}$$

where

$$N = \frac{a}{\sqrt{1-e^2\sin^2\phi}} \tag{3.8}$$

and the ellipsoidal parameters *a* and *b* were defined in Section 2.10.1.

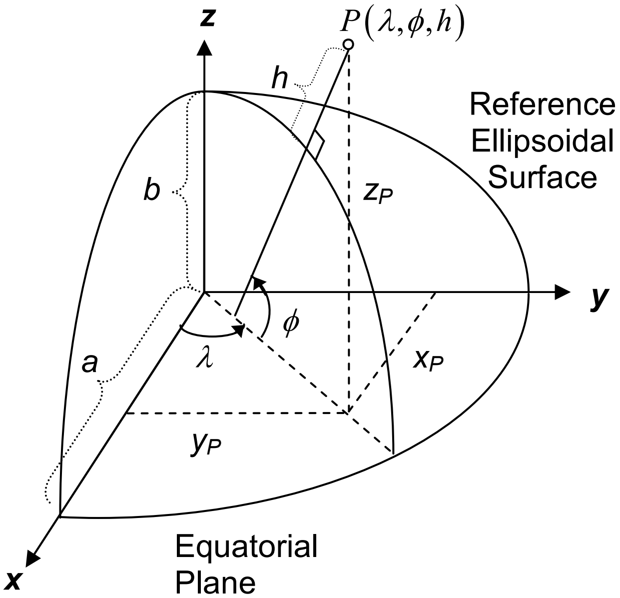

Figure 3.3: GPS Position Coordinates

With the GPS position data in Cartesian form, the vector between two positions of interest can be calculated and transformed to a convenient local reference frame. Figure 3.4 shows a global view of the flight scenario of Section 3.1, where the point o represents the position of the ground station autopilot interface and the point u represents the position of the UAV's center of gravity. The vector between points o and u in the WGS-84 frame is given by

$$\vec{r}_{uo}^{\,WGS-84} = \vec{r}_u - \vec{r}_o \tag{3.9}$$

The vector must be transformed to a local frame to complete the geometrical analysis. The vector can be expressed in the $x^o y^o z^o$ frame as

$$\vec{r}_{uo}^{\,o} = \left[{}^{o}A^{WGS-84} \right] \vec{r}_{uo}^{\,WGS-84} \tag{3.10}$$

where the rotation matrix $\left[{}^{o}A^{WGS-84} \right]$ is a transformation from the WGS-84 frame to the local geodetic frame specified by the definition of the $x^o y^o z^o$ frame.

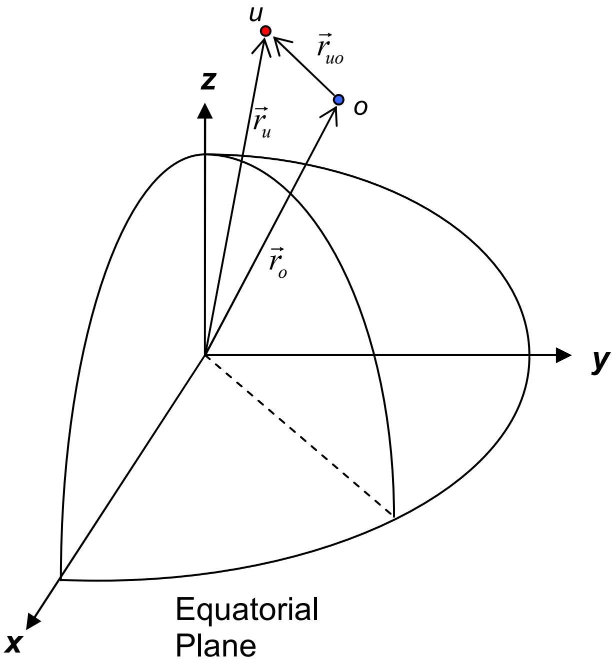

Figure 3.4: Global View of Flight Scenario

Cartesian coordinates in the WGS-84 frame can be converted to the *NWU* frame of Section 2.11.3 by three Euler rotations (Z-Y-X set) as follows:

1) Rotation about the z-axis by λ
2) Rotation about the y-axis by $\frac{3\pi}{2}-\phi$
3) Rotation about the x-axis by π

The combined rotation matrix is given by

$$\left[{}^{NWU}A^{WGS-84}\right]=\begin{bmatrix}-\sin\phi\cos\lambda & -\sin\phi\sin\lambda & \cos\phi \\ \sin\lambda & -\cos\lambda & 0 \\ \cos\phi\cos\lambda & \cos\phi\sin\lambda & \sin\phi\end{bmatrix} \tag{3.11}$$

where λ and ϕ are the longitude and latitude at the origin of the *NWU* frame and a vector in the *NWU* frame is expressed as

$$\begin{pmatrix}x\\y\\z\end{pmatrix}^{NWU}=\left[{}^{NWU}A^{WGS-84}\right]\begin{pmatrix}x\\y\\z\end{pmatrix}^{WGS-84} \tag{3.12}$$

In Section 3.3.1, the $x^o y^o z^o$ frame was defined as a *NWU* coordinate system. Therefore

$$\left[{}^{o}A^{WGS-84}\right]=\left[{}^{NWU}A^{WGS-84}\right] \tag{3.13}$$

A transformation that is closely related to the preceding one is the rotation of coordinates between the *NWU* frame and the *NED* frame defined in Section 2.11.4. Cartesian coordinates in the WGS-84 frame can be converted to the *NED* frame by the Euler rotations 1) and 2) given above. Therefore, *NWU* and *NED* coordinates are simply related by a rotation about the x-axis by an angle of π radians, which is expressed as

$$\begin{pmatrix}x\\y\\z\end{pmatrix}^{NWU}=\begin{bmatrix}1 & 0 & 0\\0 & -1 & 0\\0 & 0 & -1\end{bmatrix}\begin{pmatrix}x\\y\\z\end{pmatrix}^{NED} \tag{3.14}$$

3.3.4 Vectors

In order to evaluate the Friis Transmission Equation, an expression for the vector between the ground station and UAV antennas must be found. Figure 3.5 introduces the primary vectors along with notation of the flight scenario. The vector superscripts denote the coordinate system and the subscripts denote the direction of the vector, for example, $\vec{r}^{\,gs}_{ags}$ is the vector pointing from *gs* to *a*. The vector $\vec{r}^{\,u}_{au}$, shown in the inset, defines the position of the UAV antenna frame origin. The vector $\vec{r}^{\,o}_{gso}$ defines the position of the ground station antenna frame origin. Both of these vectors are assumed to be known. In addition, the vector $\vec{r}^{\,o}_{uo}$ was calculated in Section 3.3.3. The objective is to solve for the vector $\vec{r}^{\,gs}_{ags}$.

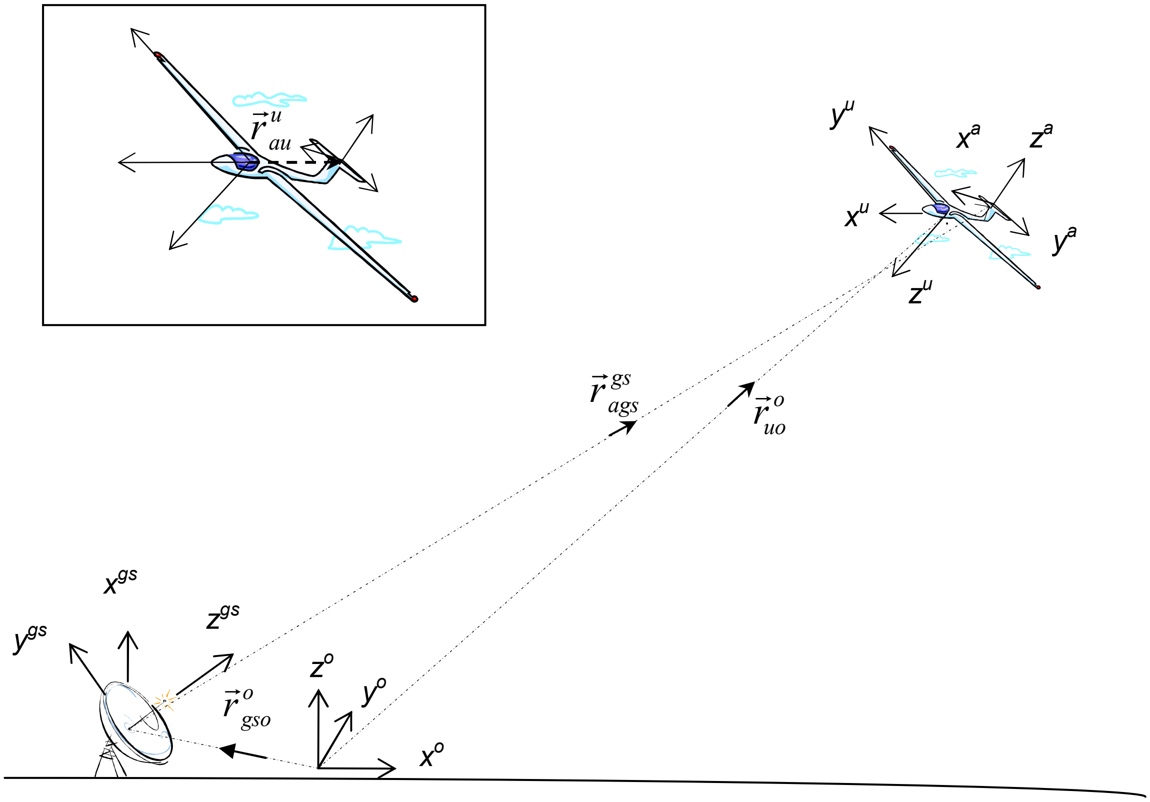

Figure 3.5: Flight Scenario Analysis

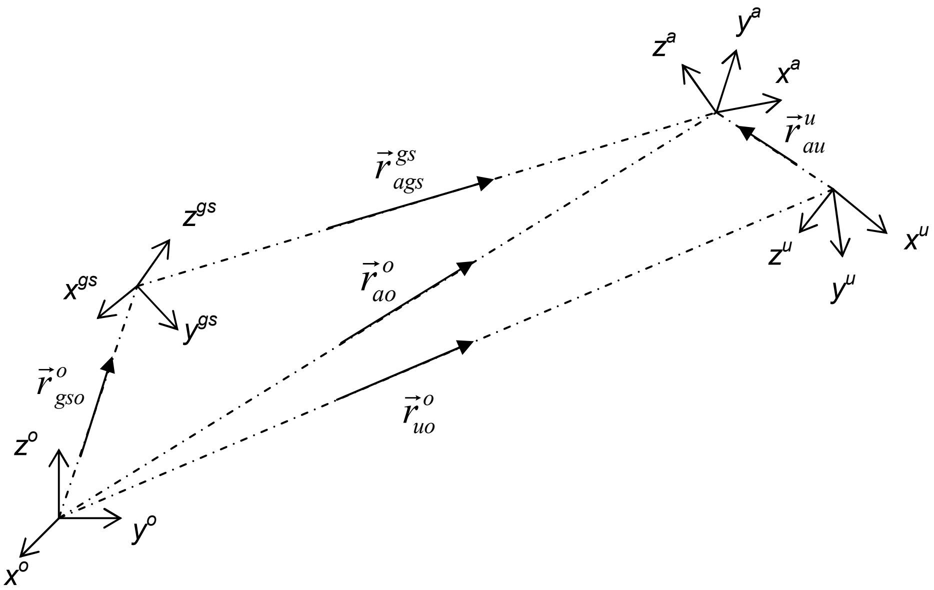

Figure 3.6: Vector Analysis

Figure 3.6 shows a more detailed diagram of the flight scenario; the vectors are purely representational and are not drawn to scale. The vector between the ground station autopilot interface and the UAV antenna can be expressed as

$$\vec{r}_{ao}^{\,o} = \vec{r}_{uo}^{\,o} + \left[{}^{o}A^{u}\right]\vec{r}_{au}^{\,u} \tag{3.15}$$

The vector pointing from the ground station antenna to the UAV antenna is given by

$$\vec{r}_{ags}^{\,gs} = \left[{}^{gs}A^{o}\right]\left(\vec{r}_{ao}^{\,o} - \vec{r}_{gso}^{\,o}\right) \tag{3.16}$$

And it follows from (3.16) that the vector pointing from the UAV antenna to the ground station antenna is given by

$$\vec{r}_{gsa}^{\,a} = \left[{}^{a}A^{u}\right]\left[{}^{u}A^{o}\right]\left(\vec{r}_{gso}^{\,o} - \vec{r}_{ao}^{\,o}\right) \tag{3.17}$$

3.3.5 Spherical Antenna Angles

In order to evaluate the gain of the UAV and ground station antennas, the spherical angles of the vectors between the antennas must be expressed in their respective coordinate systems. The vectors are first normalized as

$$\hat{r}_{ags}^{gs} = \frac{\vec{r}_{ags}^{gs}}{\left\|\vec{r}_{ags}^{gs}\right\|} = x'_{ags}\hat{x}^{gs} + y'_{ags}\hat{y}^{gs} + z'_{ags}\hat{z}^{gs} \tag{3.18}$$

and

$$\hat{r}_{gsa}^{a} = \frac{\vec{r}_{gsa}^{a}}{\left\|\vec{r}_{gsa}^{a}\right\|} = x'_{gsa}\hat{x}^{a} + y'_{gsa}\hat{y}^{a} + z'_{gsa}\hat{z}^{a} \tag{3.19}$$

The spherical angles for the ground station antenna are then given by

$$\theta_{gs} = \tan^{-1}\left(\frac{\sqrt{\left(x'_{ags}\right)^2 + \left(y'_{ags}\right)^2}}{\left(z'_{ags}\right)^2}\right) \tag{3.20}$$

$$\phi_{gs} = \tan^{-1}\left(\frac{y'_{ags}}{x'_{ags}}\right) \tag{3.21}$$

Similarly, the spherical angles for the UAV antenna are

$$\theta_{a} = \tan^{-1}\left(\frac{\sqrt{\left(x'_{gsa}\right)^2 + \left(y'_{gsa}\right)^2}}{\left(z'_{gsa}\right)^2}\right) \tag{3.22}$$

$$\phi_{a} = \tan^{-1}\left(\frac{y'_{gsa}}{x'_{gsa}}\right) \tag{3.23}$$

The elevation angle θ is calculated using the MATLAB function *atan* and the azimuth angle ϕ is calculated using the MATLAB function *atan2*.

3.4 Directional Antenna Gain

Methods for evaluating the directional gain of three popular antennas will be presented in this section. The gain of a half-wave dipole, a Yagi-Uda antenna, and a rectangular patch antenna are addressed. For this study, it is desirable to use approximate analytical expressions for the gain.

3.4.1 Half-wave Dipole Antenna

The half-wave dipole is an extensively used antenna. A simple half-wave dipole antenna consists of two quarter-wavelength sections of wire with a center feed point. The radiation pattern of a half-wave dipole was shown previously in Figure 2.2. An example of a half-wave dipole is shown in Figure 3.7. This dipole, which was constructed from flexible coaxial cable and designed for a 900 MHz communication link, is embedded in the seam of an inflatable wing airfoil.

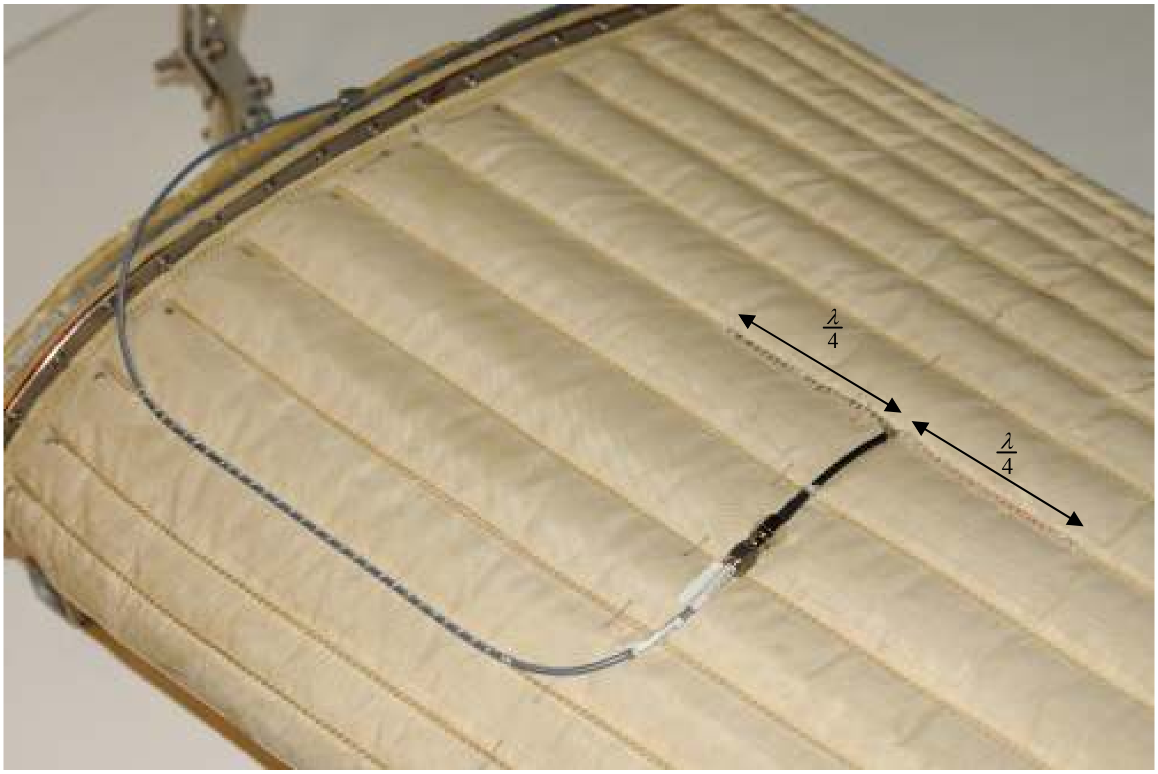

Figure 3.7: Example of Half-wave Dipole

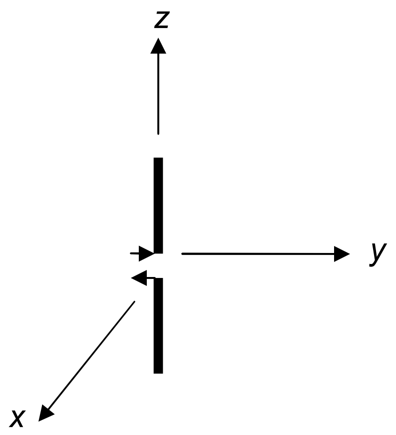

Figure 3.8: Half-wave Dipole

A *z*-directed half-wave dipole is shown in Figure 3.8. The feed point arrows indicate the direction of the current flow. The gain of a *z*-directed half-wave dipole can be evaluated following the analysis in [13]. The total power radiated by the antenna is given by [13]

$$P_{rad} \cong 2.435\eta \frac{|I_o|^2}{8\pi} \tag{3.24}$$

where I_o is the amplitude of the current excitation and η is the intrinsic impedance of the medium. The radiation intensity is [13]

$$U(\theta) \cong \eta \frac{|I_o|^2}{8\pi^2} \sin^3\theta \tag{3.25}$$

Substituting (3.24) and (3.25) into (2.5) to find the directivity yields

$$D_{\frac{\lambda}{2}dipole}(\theta) \cong 1.643 \sin^3\theta \tag{3.26}$$

Since the radiation efficiency of a wire half-wave dipole approaches 100% [13], the gain of (2.8) reduces to

$$G_{\frac{\lambda}{2}dipole}(\theta) \cong 1.643 \sin^3\theta \tag{3.27}$$

3.4.2 Three-element Yagi-Uda Antenna

A Yagi-Uda antenna, commonly called a Yagi antenna, is essentially an array of linear dipole antennas. As shown in Figure 3.9, the Yagi antenna consists of a reflector element, a driven element, and any number of director elements. The driven element is energized directly by a feed transmission line, while the reflector and director elements act as parasitic radiators whose currents are induced by mutual coupling [13]. The driven element is typically a half-wave dipole, which is resonant with its length slightly less than a half-wavelength. In general, the reflector is longer than the driven element and the directors are shorter than the driven element. Depending upon the design, the length, diameter, and spacing of the director elements is not always uniform. The separation between the reflector and the driven element has been found to be optimum around a quarter-wavelength [13].

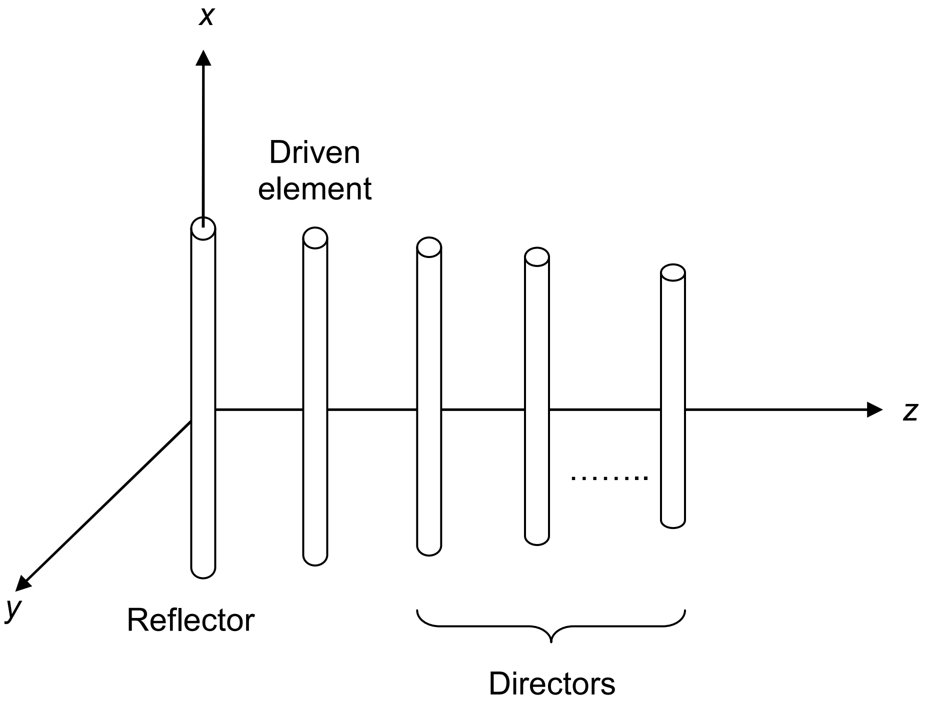

Figure 3.9: Yagi-Uda Antenna

Yagi antennas are quite common in practice because they are lightweight, simple to build, low cost, and provide desirable characteristics for many applications [13]. Figure 3.10 shows an example of a Yagi antenna. This 5-element Yagi was designed for UHF operation at 900 MHz.

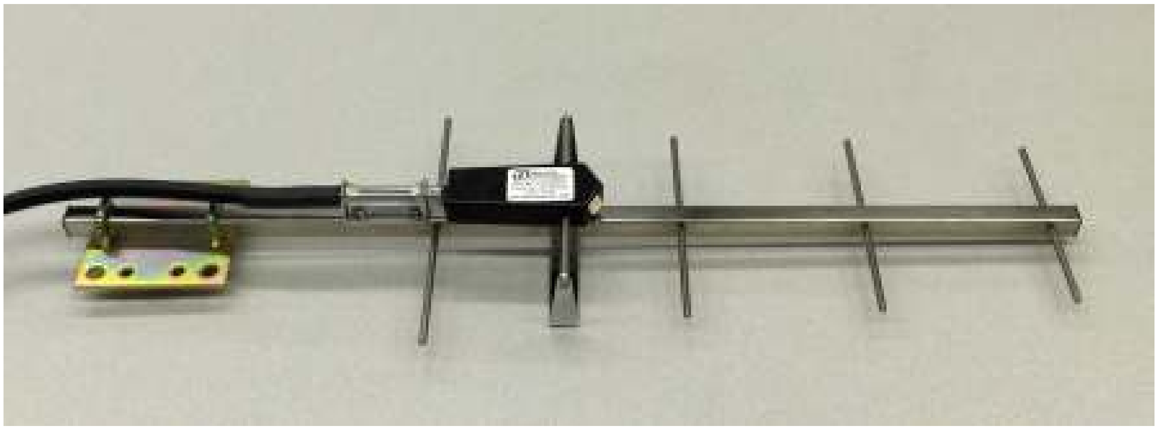

Figure 3.10: 5-element Yagi Antenna

Typically, a method of moments (MoM) computer code is used to evaluate the gain versus angle of the Yagi antenna. This approach is accurate as it includes the mutual coupling effects of the parasitic elements on the driven element. For this study, however, the constantly changing orientation of the UAV in flight necessitates evaluation of the gain at many different angles. Rather than embed a MoM code into the simulation program developed in this study, an approximate method was implemented using the concept of pattern multiplication for linear arrays. The approximate method is efficient as it involves evaluation of an analytical function multiplying the sum of three complex numbers evaluated for each given angle.

In this study, the gain of the Yagi antenna is approximated by treating the antenna as an array of identical half-wave dipole elements and applying linear array theory to find the array factor. Since the lengths of the reflector and director elements are slightly longer and shorter, respectively, than the resonant half-wavelength element, the shape of the current distribution on those elements will deviate from that of the resonant half-wave dipole, which is shown in Figure 3.11.

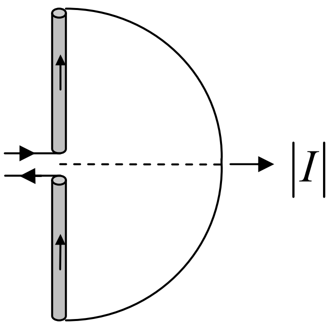

Figure 3.11: Current Distribution on Half-wave Dipole

However, the differences in length for a practical Yagi antenna are not great. The deviations are small enough so that the actual radiation patterns of the elements are closely approximated by the radiation pattern of a half-wave dipole. Then, according to pattern multiplication, the approximate radiation pattern of the Yagi antenna is the product of the array factor and the normalized element pattern, which in this case is that of the half-wave dipole.

The linear array theory presented in Section 2.9 will be applied to find the gain of the 3-element Yagi antenna shown in Figure 3.12a.

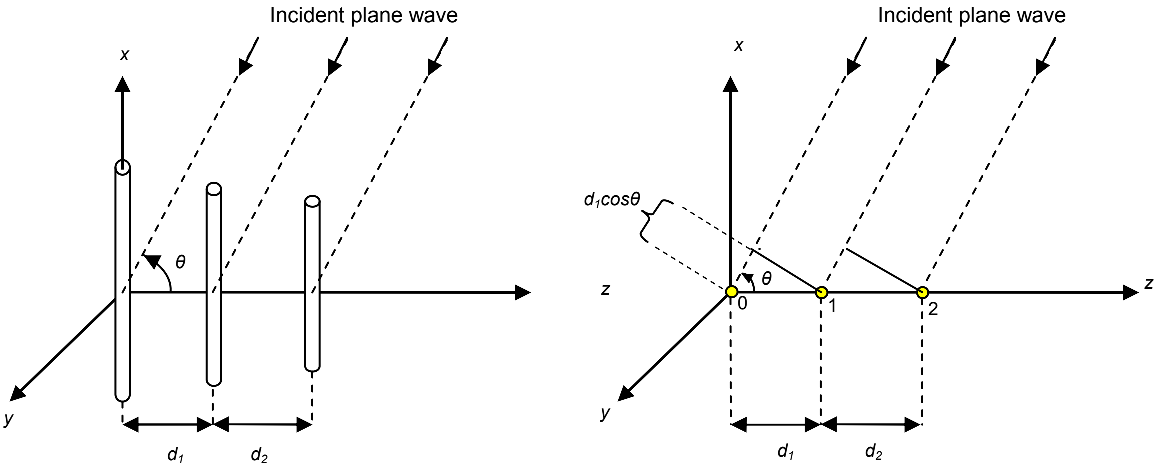

(a) 3-element Yagi antenna

(b) Equivalent array of point sources

Figure 3.12: Linear Array Analysis of Yagi

Replacing each element with a point source as in Figure 3.12b and applying (2.14) yields the array factor as

$$AF = I_0 + I_1 e^{j\beta d_1 \cos\theta} + I_2 e^{j\beta(d_1+d_2)\cos\theta} \tag{3.28}$$

where I_0, I_1, and I_2 are the current excitations at the element centers. The current excitations for each center element are found apriori by running one simulation with a wire antenna program such as the widely used MININEC or the WIRE code written by Dr. William A. Davis of Virginia Polytechnic Institute and State University.

The element pattern in this case is the radiation pattern of an *x*-directed half-wave dipole, which can be found by analogy to an equivalent antenna oriented along the *z*-axis. The radiation pattern of that *z*-directed half-wave dipole is [14]

$$F(\theta,\phi) = \frac{\cos\left(\frac{\pi}{2}\cos\theta\right)}{\sin\theta} \tag{3.29}$$

If an angle γ is defined off the *x*-axis, then it can be related to the spherical angles θ and ϕ by

$$\cos\gamma = \sin\theta\cos\phi \tag{3.30}$$

$$\sin\gamma = \sqrt{1-\sin^2\theta\cos^2\phi} \tag{3.31}$$

The angle γ for the x-directed dipole is equivalent to the angle θ for the z-directed dipole, so (3.30) and (3.31) can be substituted in (3.29) to give the radiation pattern of the *x*-directed dipole as

$$F(\theta,\phi) = \frac{\cos\left(\frac{\pi}{2}\sin\theta\cos\phi\right)}{\sqrt{1-\sin^2\theta\cos^2\phi}} \tag{3.32}$$

The un-normalized radiation pattern of the Yagi antenna is given by the product of (3.28) and (3.32). The directivity of the Yagi antenna is given by

$$D_{Yagi}(\theta,\phi) = D\left|F_{Yagi}(\theta,\phi)\right|^2 \tag{3.33}$$

where F_{Yagi} is the normalized radiation pattern and D is the peak value of the directivity. The gain of the Yagi is

$$G_{Yagi}(\theta,\phi) = e_{cd} D_{Yagi}(\theta,\phi) = G\left|F_{Yagi}(\theta,\phi)\right|^2 \tag{3.34}$$

where $G = e_{cd} D$ is the peak value of the gain. The peak value of the gain is found by simulating the Yagi antenna with the WIRE code previously mentioned.

To illustrate the accuracy of the approximate method, the WIRE code was used to simulate a 3-element Yagi antenna. The Yagi had a reflector length of .49λ, a driver length of .4781λ, a director length of .45λ, a reflector spacing (d_1) of .2λ, and a director spacing (d_2) of .25λ. The radius of the elements was .001λ. The gain of the antenna (E-plane cut) as calculated by the WIRE code and the approximation method is shown in Figure 3.13 below. The gain calculated by the approximation method is very close to the WIRE code gain.

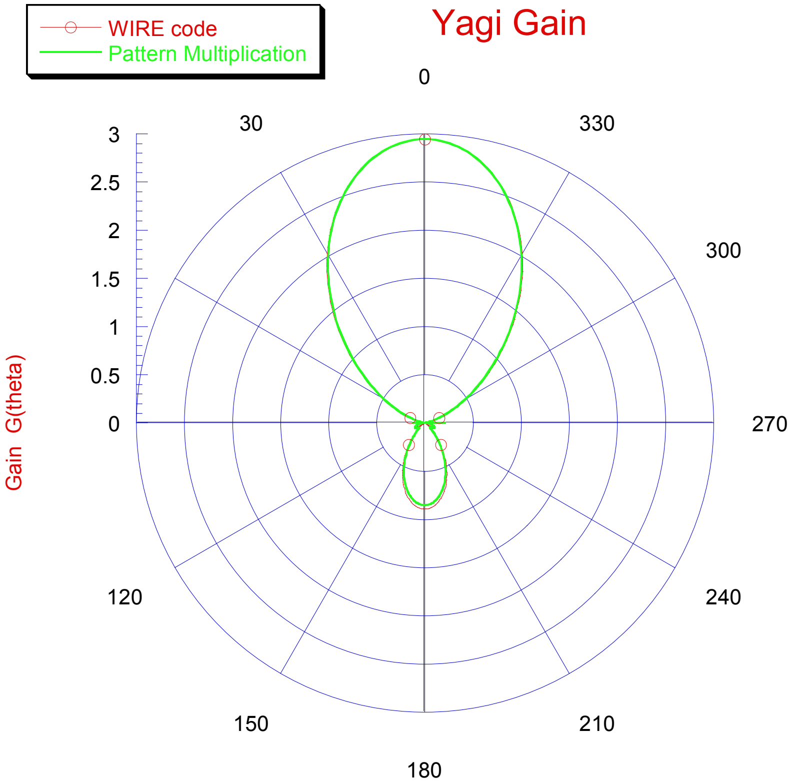

Figure 3.13: Yagi Gain

3.4.3 Rectangular Patch Antenna

Microstrip antennas, often referred to as patch antennas, are usually photo-etched on a dielectric substrate. While patch antennas come in a variety of shapes, the rectangular patch is the most widely used configuration since it is easy to analyze and fabricate and has attractive radiation characteristics [13]. The geometry of a rectangular patch is shown in Figure 3.14 below, where ε_r is the dielectric constant of the substrate and h is the height of the substrate. A rectangular patch antenna can be modeled as an array of two radiating slots, each of width W and height h, separated by a distance L [13]. An example of a rectangular patch along with its microstrip feed line is shown in Figure 3.15.

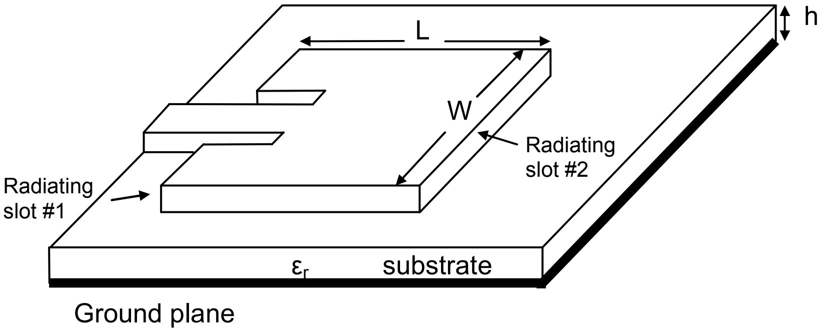

Figure 3.14: Rectangular Patch Layout

Figure 3.15: Rectangular Patch

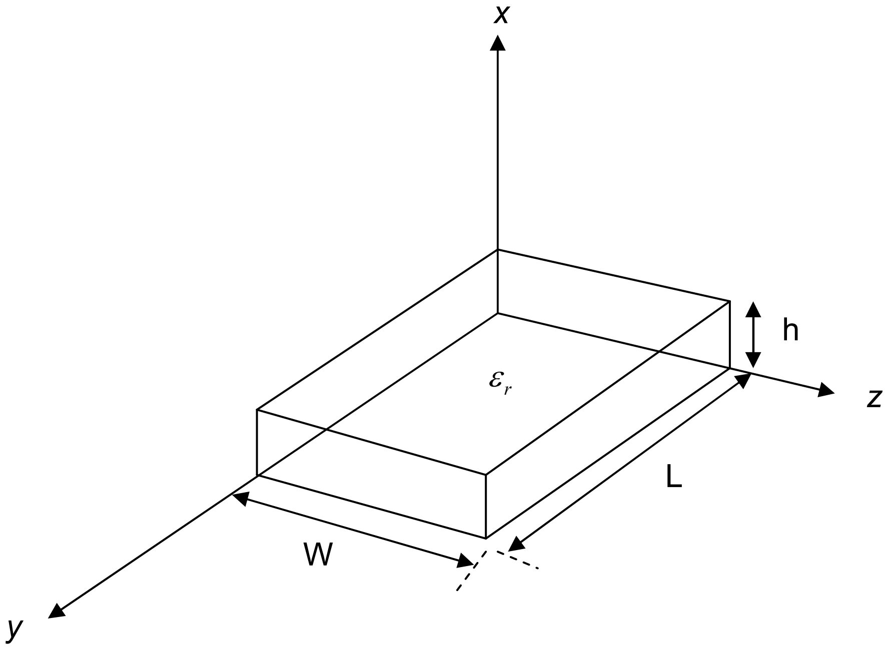

Figure 3.16: Geometry of Rectangular Patch

To evaluate the gain of the rectangular patch of Figure 3.16, the popular transmission-line and cavity models will be considered. A design procedure for calculating the physical antenna dimensions follows from the transmission-line model, which represents the patch antenna by two slots separated by a low-impedance transmission line of length *L* [13]. The cavity model, which represents the patch antenna as an array of two radiating slots, has been used to derive an analytical expression for the far-zone electric field radiated by the antenna [13].

The design procedure determines the width W and the length L of the patch given the dielectric constant ε_r and height h of the substrate, and the desired resonant frequency f_r. The width is given by [13]

$$W = \frac{c}{2f_r}\sqrt{\frac{2}{\varepsilon_r + 1}} \tag{3.35}$$

where *c* is the speed of light in free space.

The effective dielectric constant of the substrate is [13]

$$\varepsilon_{reff}=\frac{\varepsilon_r+1}{2}+\frac{\varepsilon_r-1}{2\sqrt{1+12\frac{h}{W}}} \tag{3.36}$$

The fringing effect extends the physical length L of the patch by [13]

$$\Delta L=0.412h\frac{\left(\varepsilon_{reff}+0.3\right)\left[\frac{W}{h}+0.264\right]}{\left(\varepsilon_{reff}-0.258\right)\left[\frac{W}{h}+0.8\right]} \tag{3.37}$$

The effective length of the patch is [13]

$$L_e=\frac{\lambda}{2}=\frac{c}{2f_r\sqrt{\varepsilon_{reff}}} \tag{3.38}$$

Finally, the physical length of the patch is given by [13]

$$L=L_e-2\Delta L \tag{3.39}$$

The far-zone electric field of the patch antenna of Figure 3.16 is approximated by [13]

$$E_\phi\cong -j\frac{4V_oe^{-jk_0r}}{\pi r}\sin\theta\frac{\sin\left(\frac{k_0W}{2}\cos\theta\right)}{\cos\theta}\cos\left(\frac{k_0L_e}{2}\sin\theta\sin\phi\right) \tag{3.40}$$

provided $k_0h \prec\prec 1$, where V_o is the voltage across the radiating slot and k_0 is the free-space phase constant. The radiation intensity of (2.2) is then [13]

$$U\left(\theta,\phi\right)=\frac{8\left|V_o\right|^2}{\eta\pi^2}\left|\sin\theta\frac{\sin\left(\frac{k_0W}{2}\cos\theta\right)}{\cos\theta}\cos\left(\frac{k_0L_e}{2}\sin\theta\sin\phi\right)\right|^2 \tag{3.41}$$

The total radiated power of (2.3) is given by [13]

$$P_{rad}=\frac{8\left|V_o\right|^2}{\eta\pi^2}\int_0^\pi\int_0^\pi\left|\sin\theta\frac{\sin\left(\frac{k_0W}{2}\cos\theta\right)}{\cos\theta}\cos\left(\frac{k_0L_e}{2}\sin\theta\sin\phi\right)\right|^2\sin\theta d\theta d\phi \tag{3.42}$$

Substituting (3.41) and (3.42) into (2.5) to find the directivity yields [13]

$$D_{rect\_patch}\left(\theta,\phi\right)=4\pi\frac{\left|\sin\theta\frac{\sin\left(\frac{k_0W}{2}\cos\theta\right)}{\cos\theta}\cos\left(\frac{k_0L_e}{2}\sin\theta\sin\phi\right)\right|^2}{\int_0^\pi\int_0^\pi\left|\sin\theta\frac{\sin\left(\frac{k_0W}{2}\cos\theta\right)}{\cos\theta}\cos\left(\frac{k_0L_e}{2}\sin\theta\sin\phi\right)\right|^2\sin\theta d\theta d\phi} \tag{3.43}$$

Finally, the gain of the rectangular patch is [13]

$$G_{rect\_patch}\left(\theta,\phi\right)=e_{cd}D_{rect\_patch}\left(\theta,\phi\right) \tag{3.44}$$

where the radiation efficiency e_{cd} will be derived in the following paragraph.

The efficiency of a rectangular patch antenna ranges typically from 95 to 99 percent [25]. To calculate the efficiency, a quality factor associated with each loss mechanism will be evaluated. The derivation of the efficiency of a rectangular patch follows from [25]. The efficiency is given by [25]

$$e_{cd}=\frac{Q_t}{Q_{rad}}=\frac{\frac{1}{Q_{rad}}}{\frac{1}{Q_t}} \tag{3.45}$$

where Q_t is the total quality factor of the antenna and Q_{rad} is the radiation quality factor. The inverse of the total quality factor is given by [25]

$$\frac{1}{Q_t}=\frac{1}{Q_{rad}}+\frac{1}{Q_{sw}}+\frac{1}{Q_{di}}+\frac{1}{Q_{cu}} \tag{3.46}$$

where Q_{cu} and Q_{di} are the quality factors due to conductor and dielectric loss, respectively, and Q_{sw} is the quality factor of the loss associated with surface wave propagation. The dielectric quality factor is given by [25]

$$Q_{di}=\frac{1}{\tan\delta} \tag{3.47}$$

where $\tan\delta$ is the loss tangent of the dielectric substrate. The conductor quality factor is given by [25]

$$Q_{cu} = \frac{h}{d_s} \tag{3.48}$$

where $d_s = \frac{1}{\sqrt{\pi f_r \mu \sigma}}$ is the skin depth associated with the conductor having conductivity σ. The surface wave quality factor Q_{sw} can be neglected for thin substrates.

The radiation quality factor is given by [25]

$$Q_{rad} = \frac{\pi f_r L W \varepsilon_r \varepsilon_o}{h G_{rad}} \tag{3.49}$$

where G_{rad} is the total conductance associated with the two radiating slots. The total conductance is [13]

$$G_{rad} = 2\left(G_1 \pm G_{12}\right) \tag{3.50}$$

where the conductance of a single slot is given by [13]

$$G_1 = \frac{1}{120\pi^2} \int_0^{\pi} \left(\frac{\sin\left(\frac{k_0 W}{2} \cos\theta\right)}{\cos\theta} \right)^2 \sin^3\theta d\theta \tag{3.51}$$

and the mutual conductance is given by [13]

$$G_{12} = \frac{1}{120\pi^2} \int_0^{\pi} \left(\frac{\sin\left(\frac{k_0 W}{2} \cos\theta\right)}{\cos\theta} \right)^2 J_0\left(k_0 L \sin\theta\right) \sin^3\theta d\theta \tag{3.52}$$

where J_0 is the Bessel function of the first kind of order zero. In (3.50), the plus (+) sign is used for modes with odd (anti-symmetric) resonant voltage distribution beneath the patch and between the slots while the minus (-) sign is used for modes with even (symmetric) resonant voltage distribution [13].

The gain of a rectangular patch with parameters ε_r = 2.2, $k_0 h$ = .1, and f_r = 912 MHz was calculated using the method outlined above. The calculated efficiency of the antenna (e_{cd}) was approximately 95%. The gain of the antenna was plotted as a function of the azimuth angle for several different elevation angle cuts.

The gain of the rectangular patch antenna is shown in Figure 3.17 below.

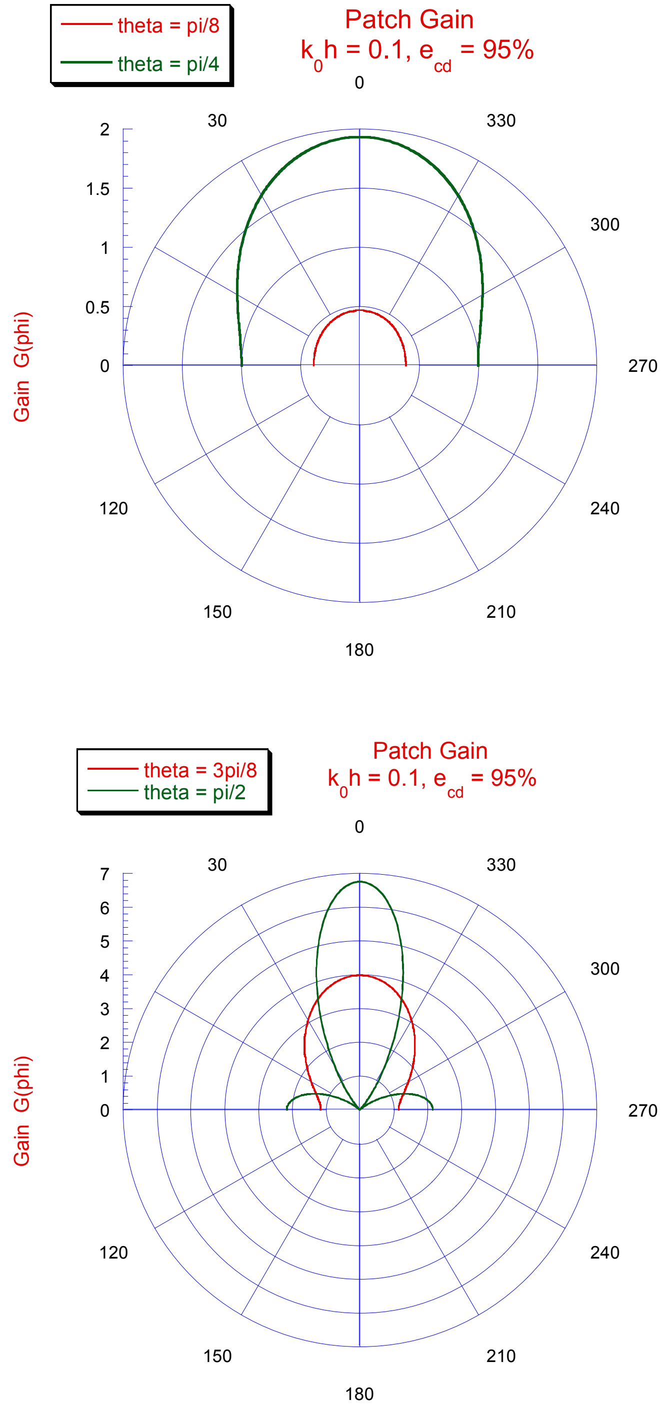

Figure 3.17: Patch Gain

3.5 Polarization Mismatch

A method for evaluating the polarization mismatch will be presented in this section.

3.5.1 Unit Polarization Vectors

The far-zone electric field of a *z*-directed half-wave dipole is given by

$$\vec{E}_{ff} \cong j\eta I_{in} \frac{e^{-j\beta r}}{2\pi r} \frac{\cos\left(\frac{\pi}{2}\cos\theta\right)}{\sin\theta} \hat{\theta} \tag{3.53}$$

where β is the free-space phase constant.

Therefore the unit polarization vector of (2.11) is given by

$$\hat{e}_{dipole} = e_\theta \hat{\theta} = \frac{\dfrac{\cos\left(\frac{\pi}{2}\cos\theta\right)}{\sin\theta}}{\left|\dfrac{\cos\left(\frac{\pi}{2}\cos\theta\right)}{\sin\theta}\right|} \hat{\theta} = \hat{\theta} \tag{3.54}$$

or in vector form

$$\hat{e}_{dipole} = \begin{bmatrix} 0 \\ e_\theta \\ 0 \end{bmatrix} \tag{3.55}$$

The unit polarization vector of the 3-element Yagi antenna of Section 3.4.2 can be derived from the far-zone electric field of an *x*-directed half-wave dipole, since the polarization is characterized by the array elements. The far-zone electric field of an *x*-directed dipole is given by (see Appendix A)

$$\vec{E}_{ff} \cong -j\eta\beta I_{in} \frac{e^{-j\beta r}}{4\pi r} \left[\hat{\theta}\cos\theta\cos\phi - \hat{\phi}\sin\phi\right] \tag{3.56}$$

Therefore the unit polarization vector of the Yagi antenna is

$$\hat{e}_{yagi} = e_\theta \hat{\theta} + e_\phi \hat{\phi} = \frac{\cos\theta\cos\phi}{\sqrt{(\cos\theta\cos\phi)^2 + \sin^2\phi}}\hat{\theta} - \frac{\sin\phi}{\sqrt{(\cos\theta\cos\phi)^2 + \sin^2\phi}}\hat{\phi} \quad (3.57)$$

or in vector form

$$\hat{e}_{yagi} = \begin{bmatrix} 0 \\ e_\theta \\ e_\phi \end{bmatrix} \quad (3.58)$$

The far-zone electric field of the rectangular patch antenna of Section 3.4.3 is

$$\vec{E}_{ff} \cong -j\frac{4V_o e^{-j\beta_0 r}}{\pi r}\sin\theta\frac{\sin\left(\frac{\beta_0 W}{2}\cos\theta\right)}{\cos\theta}\cos\left(\frac{\beta_0 L_e}{2}\sin\theta\sin\phi\right)\hat{\phi} \quad (3.59)$$

Therefore the unit polarization vector is

$$\hat{e}_{rect\_patch} = \frac{\sin\theta\frac{\sin\left(\frac{\beta_0 W}{2}\cos\theta\right)}{\cos\theta}\cos\left(\frac{\beta_0 L_e}{2}\sin\theta\sin\phi\right)}{\left|\sin\theta\frac{\sin\left(\frac{\beta_0 W}{2}\cos\theta\right)}{\cos\theta}\cos\left(\frac{\beta_0 L_e}{2}\sin\theta\sin\phi\right)\right|}\hat{\phi} \quad (3.60)$$

or in vector form

$$\hat{e}_{rect\_patch} = \begin{bmatrix} 0 \\ 0 \\ e_\phi \end{bmatrix} \quad (3.61)$$

The unit polarization vectors are evaluated at the spherical antenna angles calculated in Section 3.3.5.

3.5.2 Polarization Efficiency

In order to evaluate the polarization efficiency of (2.12), the unit polarization vectors of the UAV antenna and the ground station antenna must be referenced to a common coordinate system. The process is as follows:

1) Convert the unit polarization vectors to Cartesian form via a spherical to Cartesian transformation matrix which is given by

$$\begin{pmatrix} \hat{x} \\ \hat{y} \\ \hat{z} \end{pmatrix} = \begin{bmatrix} \sin\theta\cos\phi & \cos\theta\cos\phi & -\sin\phi \\ \sin\theta\sin\phi & \cos\theta\sin\phi & \cos\phi \\ \cos\theta & -\sin\theta & 0 \end{bmatrix} \begin{pmatrix} \hat{r} \\ \hat{\theta} \\ \hat{\phi} \end{pmatrix} \tag{3.62}$$

2) Transform the Cartesian unit polarization vectors from their respective coordinate systems to the ground station interface frame. Using the following notation

3) Evaluate the polarization efficiency as

$$\varepsilon_P = \left| \hat{e}_t^o \cdot \hat{e}_r^{o*} \right|^2 \tag{3.63}$$

3.6 Power Calculation

For the purpose of this program, it is assumed that the transmitting and receiving antennas are both impedance matched to their corresponding transmission lines. In addition, it is assumed that the atmospheric attenuation at the frequency of operation is negligible. Thus, ε_Z and ε_A both have values of unity, and (2.1) reduces to

$$P_R = \frac{P_T G_T\left(\theta_T, \phi_T\right) G_R\left(\theta_R, \phi_R\right) \lambda^2 \varepsilon_P}{\left(4\pi R\right)^2} \tag{3.64}$$

CHAPTER 4 – SIMULATION RESULTS

4.1 Program Overview

A computer program was developed to evaluate the probability of link success for a given flight path. The program is designed to process flight path data logged by an autopilot system during flights. The program loads the data log and prompts the user to select a ground station antenna and a UAV antenna for the communication link analysis. The options for the ground station antenna are a half-wave dipole or a three-element Yagi. The options for the UAV antenna are a half-wave dipole or a rectangular patch. The communication link analysis of the flight path is then performed for that case and the data generated is stored in an output file.

The program algorithm and the input and output program data are described in more detail in the following sections. The flight paths used to generate simulation results will be introduced. The flight paths will be used to simulate the performance of the communication link for the possible cases offered by the types of antennas. The simulation results will be presented in the final section.

4.2 Program Algorithm

As evidenced by the material presented in Chapter 3, the communication link analysis requires many calculations involving vectors and matrices. Due to the convenience of the built-in vector and matrix operations, the computer program was implemented in MATLAB.

The main program script can be divided into three main sections, namely, the pre-loop, the loop, and the post-loop. The algorithm flow of the main script is as follows:

Pre-loop

- Load input data
- Define link parameters: frequency and power level of transmission (i.e. P_T and λ from Equ. (3.64))
- Function call to calculate the reference position of the $x^o y^o z^o$ frame as described in Section 3.3.3
- Define the reference positions for the $x^{gs} y^{gs} z^{gs}$ and $x^a y^a z^a$ frames (i.e. $\vec{r}^{\,o}_{gso}$ and $\vec{r}^{\,u}_{au}$ from Section 3.3.4)
- Prompt user to choose a ground station and a UAV antenna; if selected, run a script to calculate the parameters for a rectangular patch antenna as described in Section 3.4.3
- Define the Euler angle sets for the antenna frames as described in Section 3.3.2
- If a directional antenna is selected, calculate or load the antenna azimuth and elevation angles to simulate tracking with a direction antenna as defined in Section 3.3.2
- Initialize the arrays for the loop calculations
- Function call to calculate the reference position of the $x^u y^u z^u$ frame as described in Section 3.3.3

Loop

- Calculate the vector between the antennas (i.e. $\vec{r}_{ags}^{gs}$) as described in Section 3.3.4
- Calculate the unit vector between the antennas and call function to calculate the look angles as described in Section 3.3.5
- Function calls to calculate the unit polarization vectors as described in Section 3.5.1

Post-loop

- Function call to calculate the polarization efficiency as described in Section 3.5.2
- Function call to calculate the antenna gains using methods described in Section 3.4
- Function call to calculate the Friis Transmission received power P_R as defined in Sections 2.2 and 3.6
- Save output data

4.3 Input Data

The ground station autopilot interface of the Piccolo II Autopilot automatically logs the telemetry received from the avionics in a text file. This data is updated every second. The data log serves as the input for the program. The program loads the individual data fields of the log into vectors for processing.

Nine of the data fields logged are utilized by the program. The hour, minute, and second data fields are used as the time stamp. The latitude, longitude, and height data fields give the location of the UAV in space, as described in Section

3.2. The yaw, pitch, and roll data fields give the orientation of the UAV in space, also described in Section 3.2.

The GPS location of the ground station interface is not logged by the autopilot interface, so that information is hard-coded in the main script. The program input data is summarized in Table 4.1.

Table 4.1 Input Data

Description	Time	Ground station location	UAV location	UAV orientation
Data Fields	Hours Minutes Seconds	Latitude [rad] Longitude [rad] Height [m]	Latitude [rad] Longitude [rad] Height [m]	Yaw [rad] Pitch [rad] Roll [rad]

4.4 Output Data

The program stores seven output variables in a binary file (.MAT file). The variables stored are the time stamp, the received power with units of watts, the received power in units of dBm, the polarization efficiency, the gain of the UAV antenna, the gain of the ground station antenna, and a scalar which gives the length of the vectors of the other six output variables. The output data is summarized in Table 4.2.

Table 4.2 Output Data

Description	Time Stamp	Received power P_r	Polarization	Gain	Vector length
Data Fields	Time [sec]	P_r [watts] P_r [dBm]	Efficiency ε_P	UAV gain Ground station gain	Scalar value

4.5 Flight Paths

Three flight paths will be considered in this study. They are designated as flight paths A, B, and C. These flight paths were logged by the University of Kentucky Aerial Robotics Team while flight testing in preparation for the 4th AUVSI (Association for Unmanned Vehicle Systems International) Student UAV Competition in June 2006 [26]. Flight paths B and C were logged while flight testing at R. J. Corman's air field in Nicholasville, Kentucky. Flight path A was logged while flight testing at the Patuxent River Naval Air Station's Webster Field, where the student UAV competition was held.

The two-dimensional (2-D) and three-dimensional (3-D) paths of each flight are displayed in this section. The maximum distance from the ground station for each flight path is summarized in Table 4.3.

Table 4.3 Maximum Distance from Ground Station

Flight Path	Range [km]	Range [mi]
A	2.5341	1.5746
B	2.9934	1.8600
C	3.1552	1.9606

The 2-D and 3-D plots of flight path A are shown in Figures 4.1 and 4.2 below.

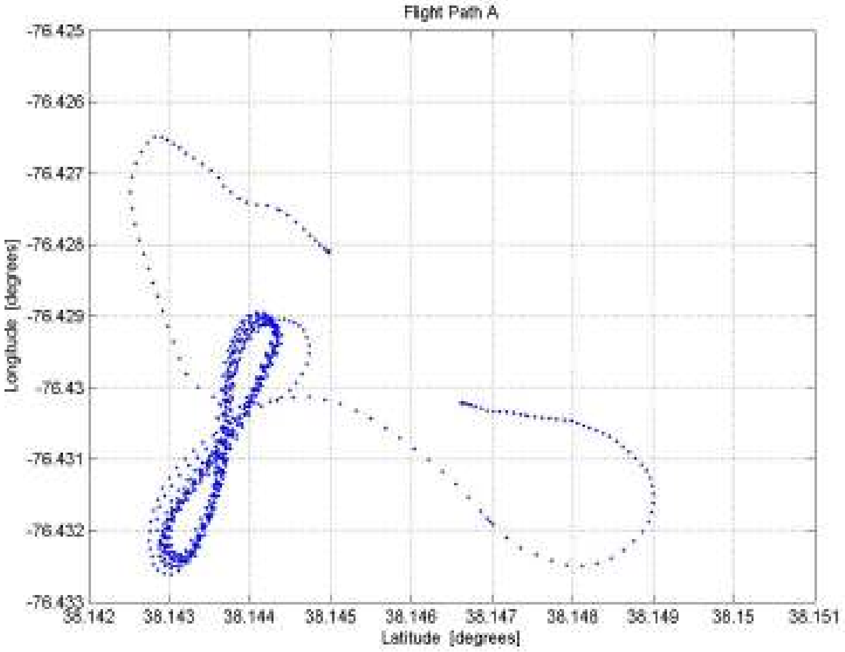

Figure 4.1: 2-D Path for Flight A

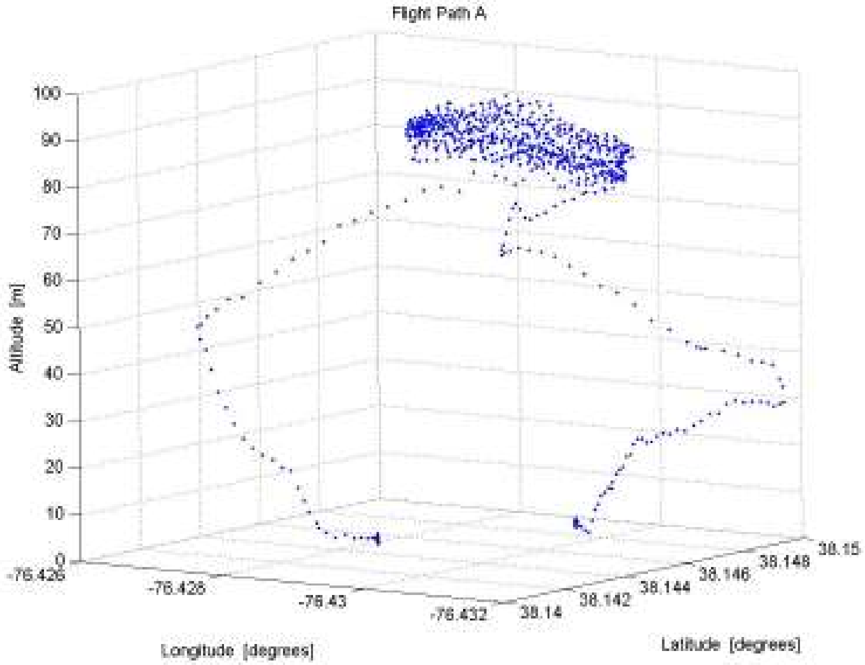

Figure 4.2: 3-D Path for Flight A

The 2-D and 3-D plots of flight path B are shown in Figures 4.3 and 4.4 below.

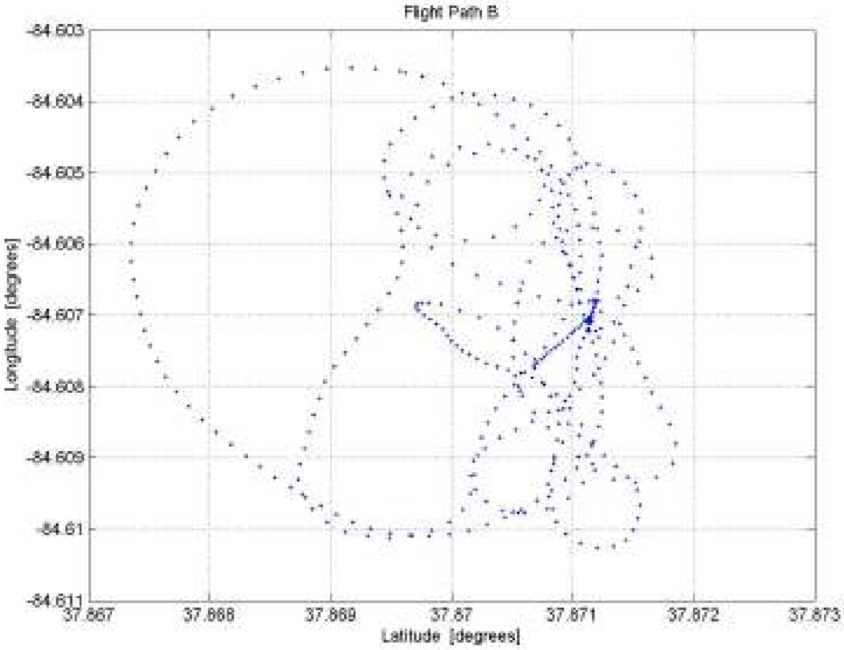

Figure 4.3: 2-D Path for Flight B

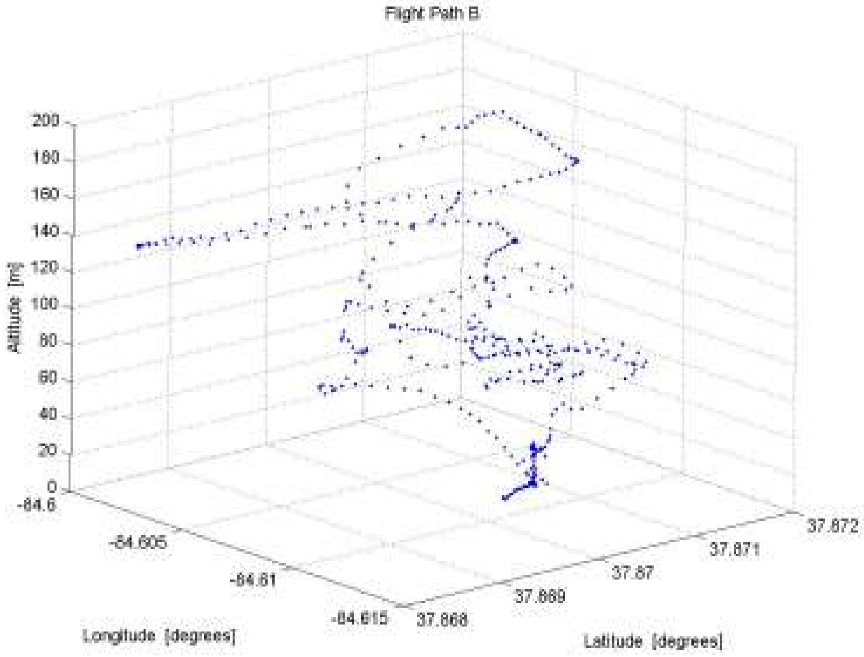

Figure 4.4: 3-D Path for Flight B

The 2-D and 3-D plots of flight path C are shown in Figures 4.5 and 4.6 below.

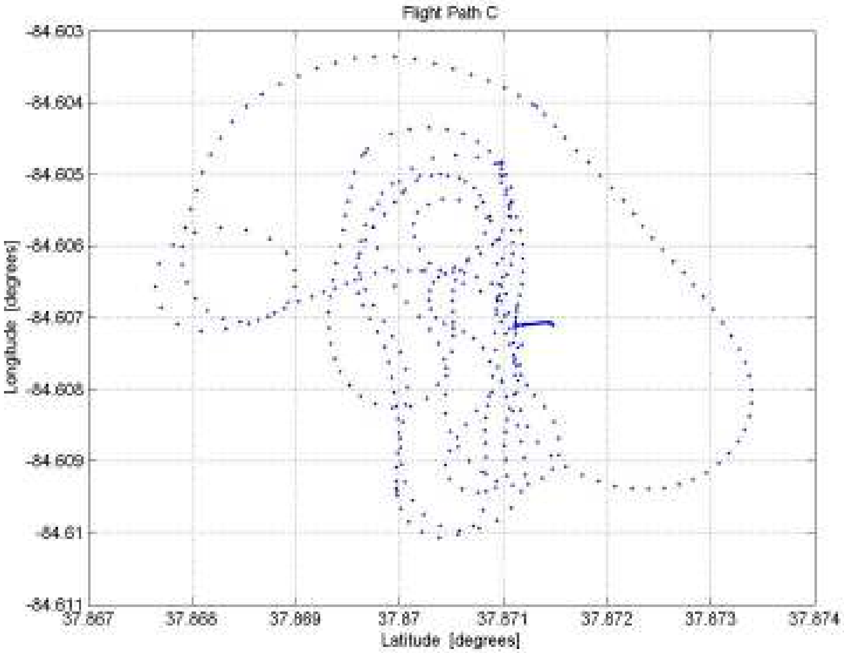

Figure 4.5: 2-D Path for Flight C

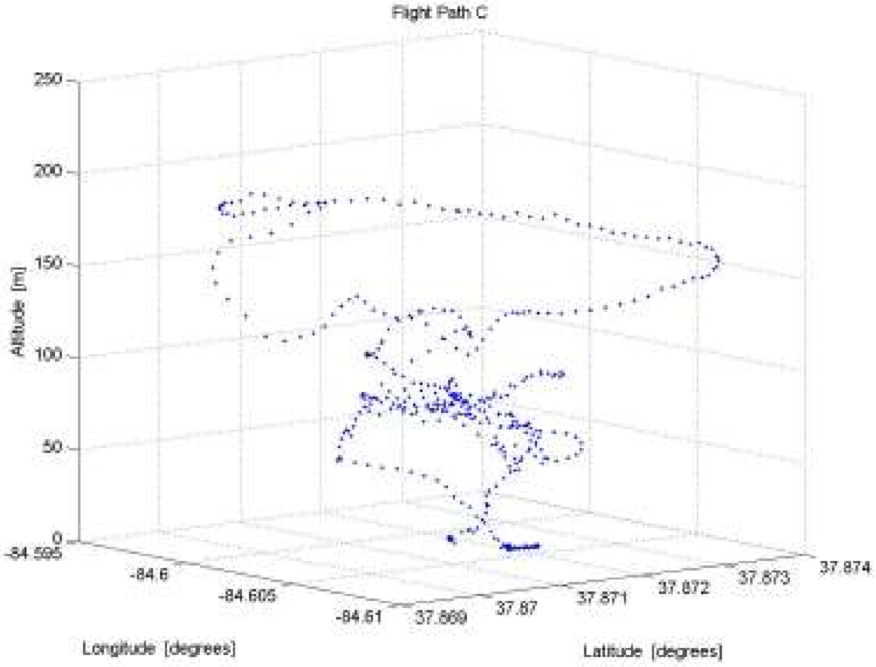

Figure 4.6: 3-D Path for Flight C

4.6 Link

The wireless link for the Piccolo II Autopilot system consists of the MHX-910 radio modem from Microhard Systems Inc. [27]. The radio operates on the 900 MHz ISM frequency band and has up to 40 Kbaud of throughput [27] [28]. The transceiver is a frequency-hopping-spread-spectrum radio which operates at 902-928 MHz and has 64 user selectable hopping patterns. The transceiver has a range of up to 60 miles line of sight and a sensitivity of -108 dBm. The output power is user selectable up to 1 W [24]. The parameters used for this computer program are as follows: frequency of 912 Mhz, transmit power of 0.1 Watt, and receiver sensitivity of -108 dBm.

The MHX radio has a receive signal strength indicator (RSSI) with a range of -71 dBm (strong signal) to -115 dBm (no signal) [24]. The Piccolo autopilot system logs this data along with the other telemetry as discussed in Section 4.3.

4.7 Flight Path Results

The simulation results for each of the three flights will be presented here. Each flight path was simulated for the four possible cases offered by the types of antennas. The cases are summarized below in Table 4.4, and will be referenced by number in the remaining sections of this thesis. Note that the values of the received power were truncated to -110 dBm since the particular numerical values below the receiver sensitivity (-108 dBm) will not be of interest when investigating the probability of success in the following chapter.

Table 4.4 Antenna Combinations

Antenna Location	Case 1	Case 2	Case 3	Case 4
Ground Station	Dipole	Yagi	Dipole	Yagi
UAV	Dipole	Dipole	Patch	Patch

The orientation of the antennas for the simulations is very important. For Case 1 and Case 3, the ground station antenna (dipole) was oriented vertically. Also note that the Yagi antenna tracks the UAV for Case 2 and Case 4 as mentioned in the program algorithm description of Section 4.2. For Case 1 and Case 2, the UAV antenna (dipole) was oriented vertically, as shown in Figure 4.7. The UAV antenna (patch) was oriented parallel to the underside of the fuselage with the radiating side down, as shown in Figure 4.8, for Case 3 and Case 4.

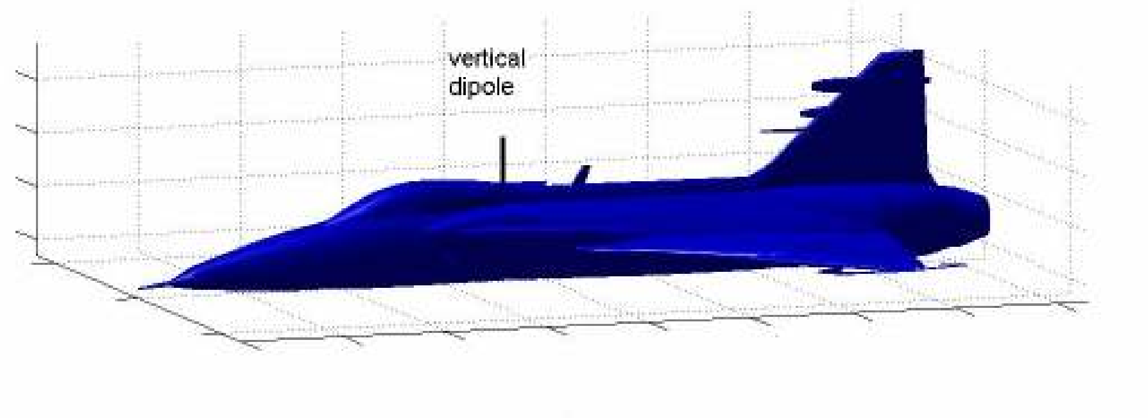

Figure 4.7: Vertically Mounted Dipole

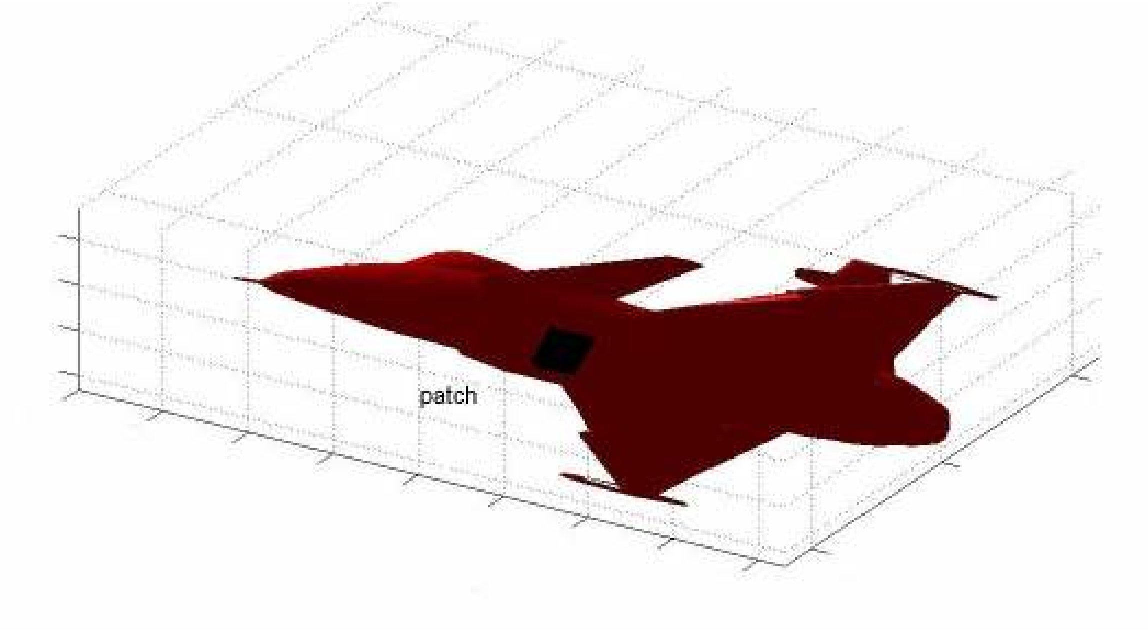

Figure 4.8: Patch Orientation

The received power for flight path A is plotted for cases one through four in Figure 4.9.

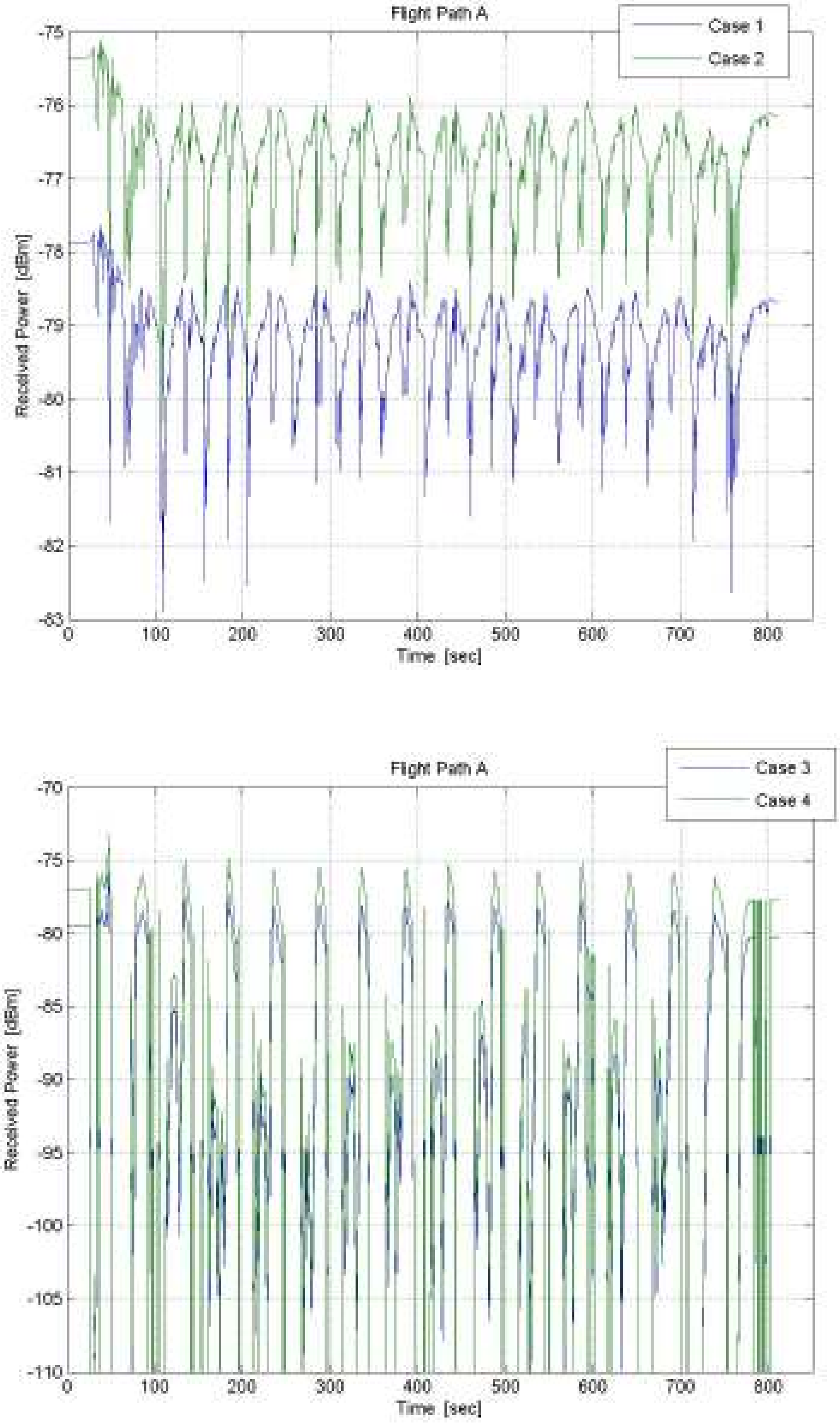

Figure 4.9: Flight Path A Received Power

The received power for flight path B is plotted for cases one through four in Figure 4.10.

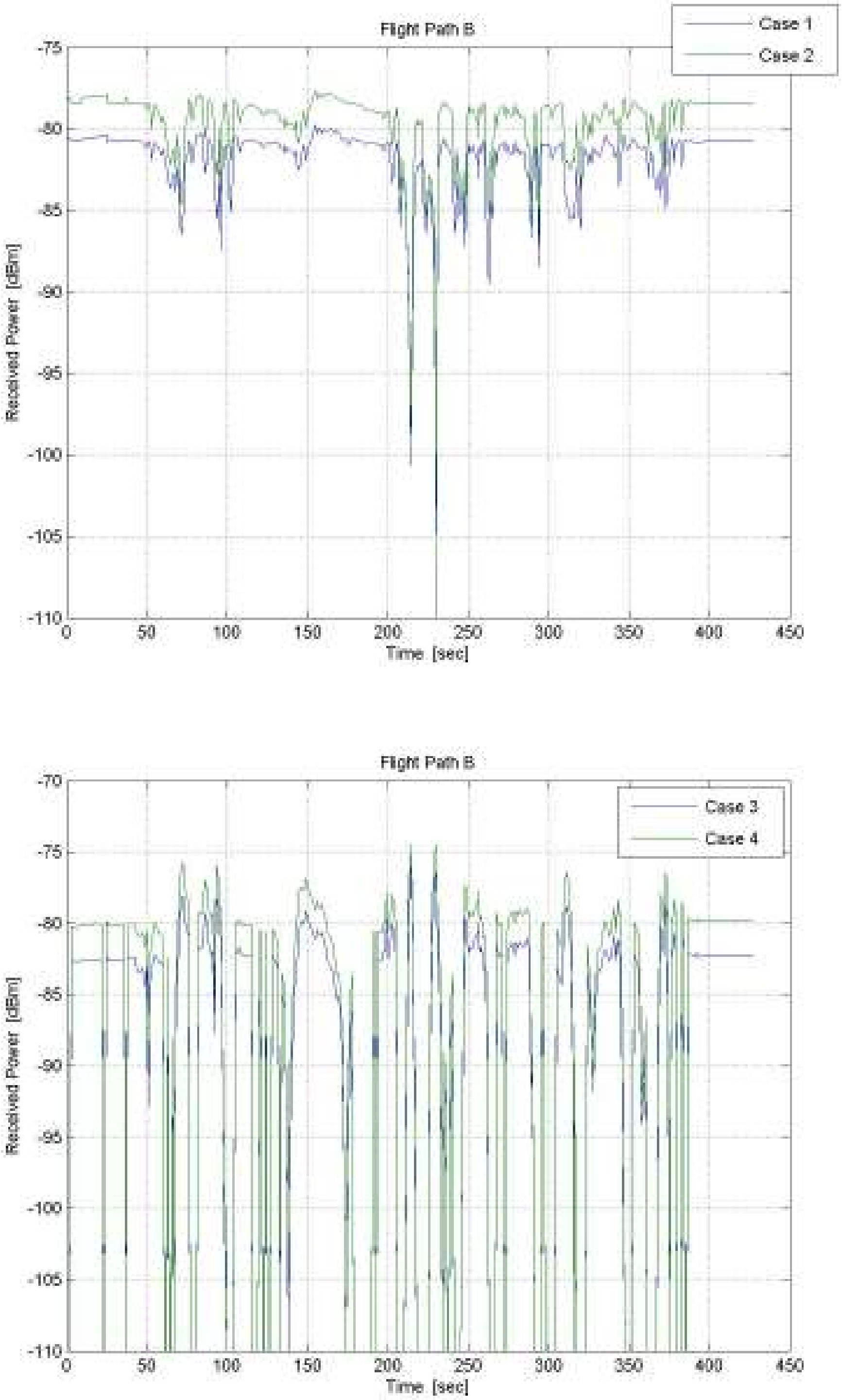

Figure 4.10: Flight Path B Received Power

The received power for flight path C is plotted for cases one through four in Figure 4.11.

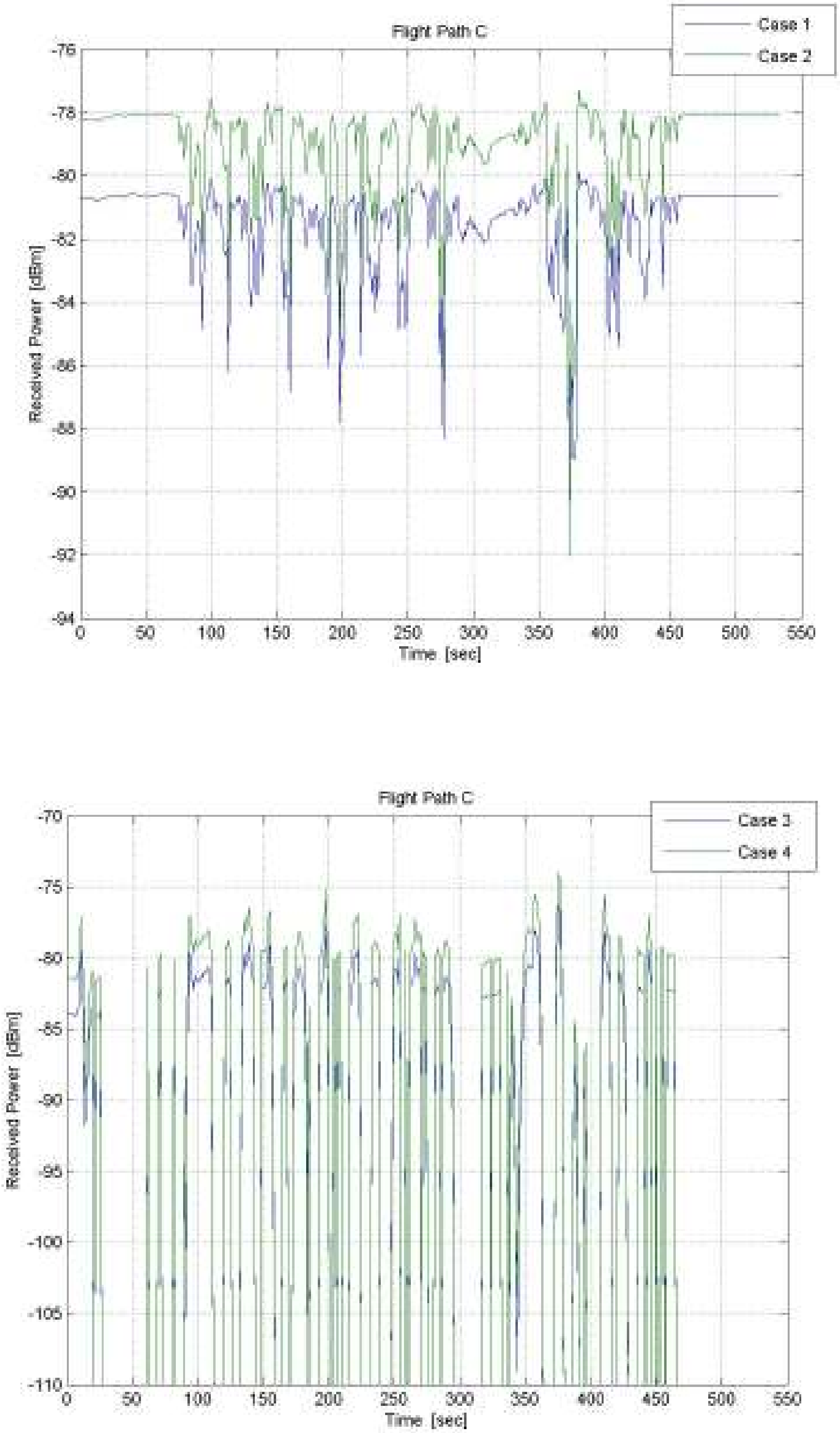

Figure 4.11: Flight Path C Received Power

The receive signal strength indicator (RSSI) data, mentioned in Section 4.6, is also plotted for the three flight paths in this section. This data is presented only for general plot shape comparison with the calculated data of Figures 4.9-4.11. There are three reasons why the RSSI data cannot be numerically compared with the calculated results.

1. The GPS location of the ground station interface during the flight testing was not recorded (see Section 4.3), so a ground station interface position was chosen when generating the simulation results
2. The RSSI data logged by the autopilot is quantized and limited to the range of -71 to -115 dBm (see Section 4.6)
3. The type of antennas used during the flight testing is uncertain and the orientation of the ground station antenna is unknown.

The RSSI data for flight path A is plotted in Figure 4.12 below.

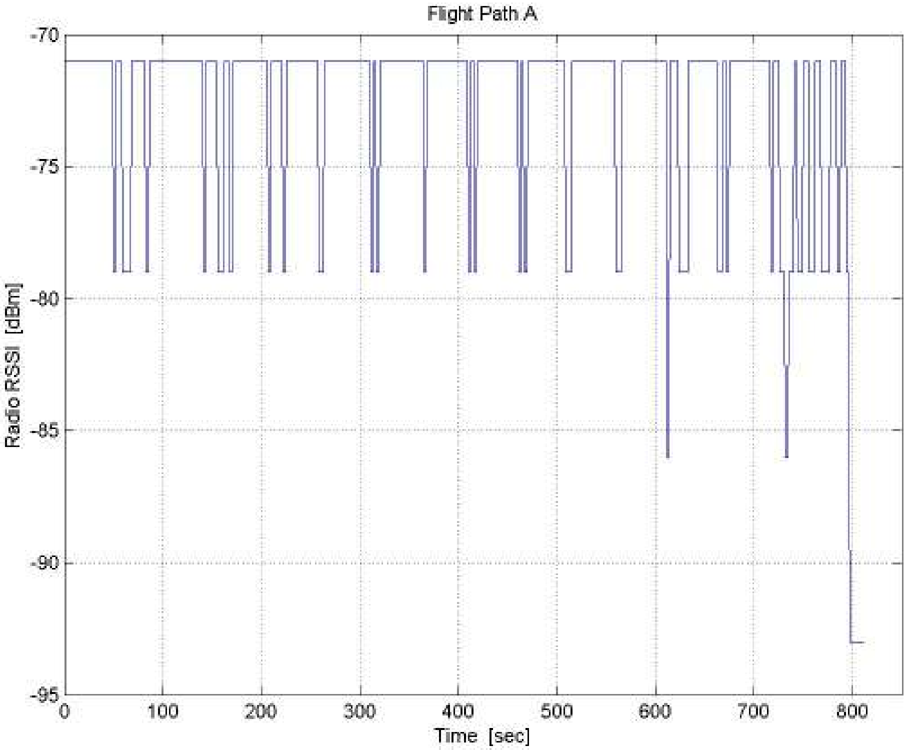

Figure 4.12: RSSI for Flight Path A

The RSSI data for flight path B is plotted in Figure 4.13 below.

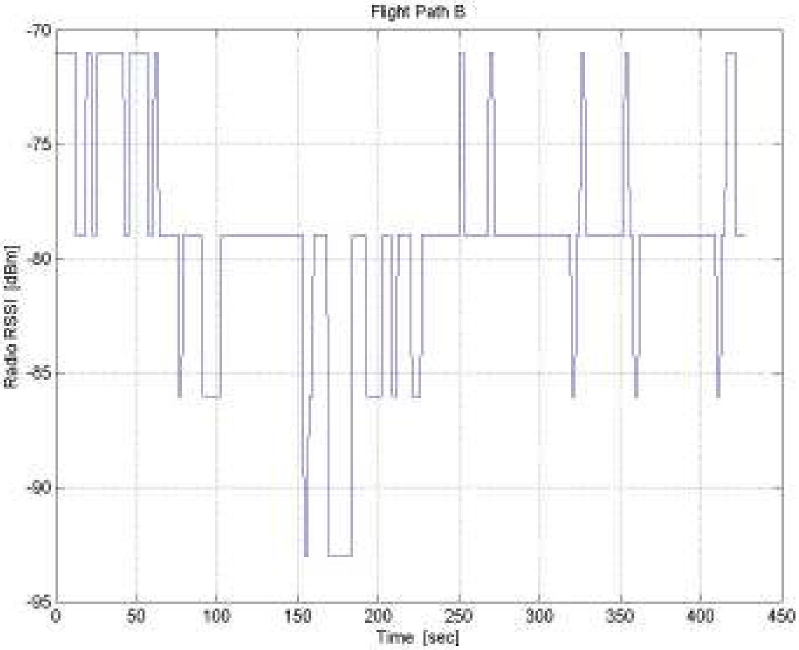

Figure 4.13: RSSI for Flight Path B

The RSSI data for flight path C is plotted in Figure 4.14 below.

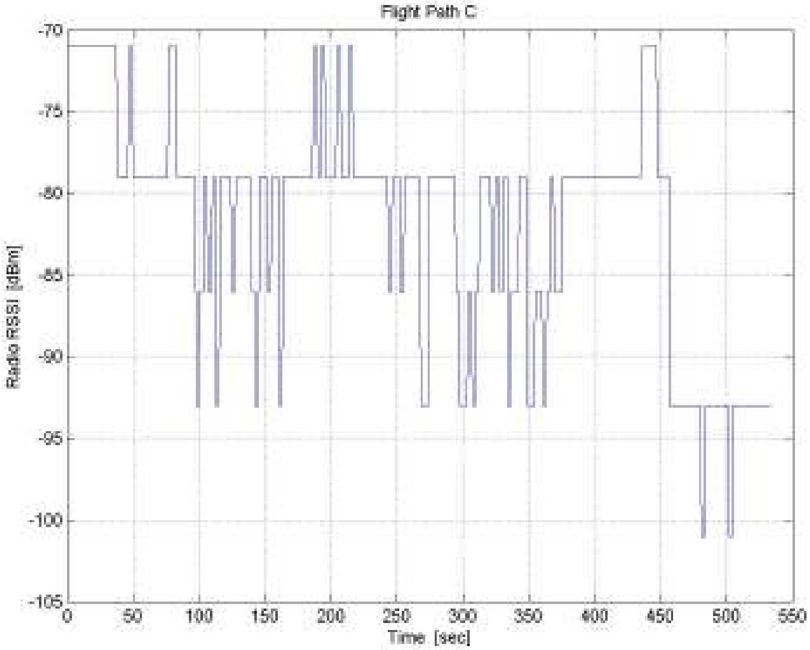

Figure 4.14: RSSI for Flight Path C

CHAPTER 5 – PROBABILITY & RELIABILITY DISCUSSION

5.1 Overview

The objective of the computer program developed for this thesis was to calculate the probability of link success for a given flight path. In order to investigate the probability of success for the communication link, several statistical tools will be defined in the following section. The probability of link success will be defined for this analysis in the subsequent section. The statistics of the flight path results presented in Section 4.5 will be reviewed in the final section of this chapter.

5.2 Statistical Definitions

For the purpose of this study, the *relative frequency* definition of probability will be considered. The relative frequency approach is based on common sense and engineering or scientific observations [29]. The probability of an event *A*, denoted by $P(A)$, is defined in terms of the relative frequency of *A* occurring in *n* trials as

$$P(A) = \lim_{n\to\infty}\left(\frac{n_A}{n}\right) \tag{5.1}$$

where n_A is the number of times that *A* occurs in *n* trials [12].

The concept of a *random variable* is foundational to the statistical tools which will be employed in this study. A real-valued random variable is a real-valued function defined on the events (elements) of the probability system [12].

Given the preceding background definitions, the main statistical functions for this analysis may now be defined. The cumulative distribution function (CDF) of the random variable *x* is defined as

$$F\left(a\right) \cong P\left(x \le a\right) \equiv \lim_{n \to \infty}\left(\frac{n_{x \le a}}{n}\right) \tag{5.2}$$

where $F\left(a\right)$ is a unit-less function [12].

The probability density function (PDF) of the random variable x is defined as

$$f\left(x\right) = \frac{dF\left(a\right)}{da}\Big|_{a=x} = \frac{dP\left(x \le a\right)}{da}\Big|_{a=x} = \lim_{\substack{n \to \infty \\ \Delta x \to 0}}\left[\frac{l}{\Delta x}\left(\frac{n_{\Delta x}}{n}\right)\right] \tag{5.3}$$

where $f\left(x\right)$ has units of 1/*x* [12].

The cumulative distribution and probability density functions posses certain characteristic properties. If any of the properties are violated, the function in question is invalidated. These properties are summarized in Table 5.1.

Table 5.1 Properties of CDF and PDF [12], [29]

CDF	PDF
1. $F\left(a\right)$ is a non-decreasing function	1. $f\left(x\right) \ge 0$ That is, $f\left(x\right)$ is a non-negative function.
2. $F\left(a\right)$ is right-hand continuous, or $\lim_{\substack{\varepsilon \to 0 \\ \varepsilon > 0}} F\left(a+\varepsilon\right) = F\left(a\right)$	2. $\int_{-\infty}^{\infty} f\left(x\right)dx = F\left(+\infty\right) = 1$
3. $F\left(a\right) = \lim_{\substack{\varepsilon \to 0 \\ \varepsilon > 0}} \int_{-\infty}^{a+\varepsilon} f\left(x\right)dx$	3. $P\left(a < x \le b\right) = \lim_{\substack{\varepsilon \to 0 \\ \varepsilon > 0}} \int_{a+\varepsilon}^{b+\varepsilon} f\left(x\right)dx$
4. $0 \le F\left(a\right) \le 1$	
5. $F\left(-\infty\right) = 0$	
6. $F\left(+\infty\right) = 1$	

5.3 Probability of Success

As stated previously, the objective of the computer program was to calculate the probability of link success for a given flight path. The probability of success for the link is the percentage of time the received power exceeds a known minimum received power threshold [30]. For the purpose of this study, the minimum received power threshold will be defined as the receiver sensitivity. The sensitivity is the amount of power which produces the minimum satisfactory performance when delivered to the receiver input terminals [14]. For commercial transceivers, the receiver sensitivity is measured and specified by the manufacturer.

The computer program calculates the amplitude of the link received power for each data point of a flight path. To perform a statistical analysis, the received power P_r in units of watts will be assigned as the random variable. The probability of success for a flight path may then be defined as the percentage of values of P_r which equal or exceed the sensitivity of the receiver. The probability of success may then be found by calculating the probability density function of the random variable P_r and applying property number three from Table 5.1. According to the theorem, the probability that the random variable *x* will take on a value within the range $a < x \leq b$ is calculated by integrating the PDF over that range. It follows that the probability of *x* taking on values greater than or equal to some value ς is given by

$$P(x \geq \varsigma) = \int_{\varsigma}^{\infty} f(x)\,dx \tag{5.4}$$

If we designate *x* to represent the random variable P_r and ς to represent the receiver sensitivity, Equ. (5.4) yields the probability of success for a flight path.

5.4 MATLAB Statistics

The MATLAB Statistics Toolbox may be utilized to perform a statistical analysis of the empirical data. The function *cdfplot(x)* displays a plot of the empirical cumulative distribution function of a random variable *x* [31]. The empirical CDF $F(a)$ is defined as the proportion of *x* values less than or equal to *a* [31]. The function *ksdensity(x)* computes a probability density estimate of the random variable *x* [31]. The probability of success is calculated by a numerical integration of the probability density estimate using the *trapz(Y)* function. This function computes an approximation of the integral of *Y* via the trapezoidal method [31].

5.5 Flight Path Result Statistics

The CDF and PDF, as described in the preceding section, were calculated and plotted for each case presented in Section 4.5. The results for flight path A are plotted in Figures 5.1 and 5.2, the results for flight path B are plotted in Figures 5.3 and 5.4, and the results for flight path C are plotted in Figures 5.5 and 5.6.

The probability of success for the flight paths is summarized in Table 5.2. The threshold value of the received power for these calculations was -108 dBm (see Section 4.6).

Table 5.2 Probability of Success Data

	Flight Path A	Flight Path B	Flight Path C
Case 1	100 %	99.8 %	100 %
Case 2	100 %	99.7 %	100 %
Case 3	77.6 %	84.7 %	62.8 %
Case 4	77.8 %	84.6 %	63.3 %

The CDF for flight path A is plotted for cases 1-4 in Figure 5.1 below.

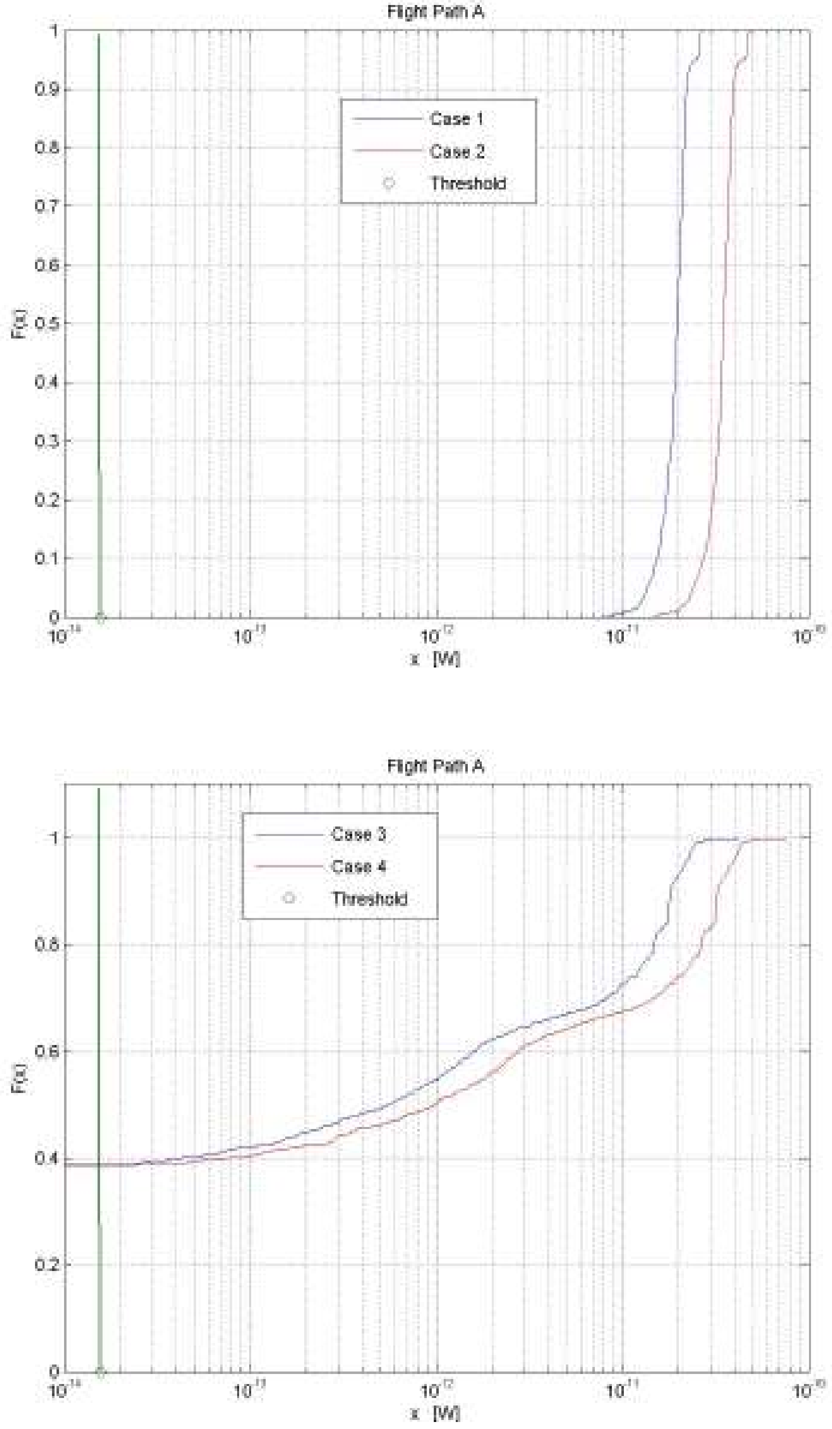

Figure 5.1: CDF for Flight Path A

The PDF for flight path A is plotted for cases 1-4 in Figure 5.2 below.

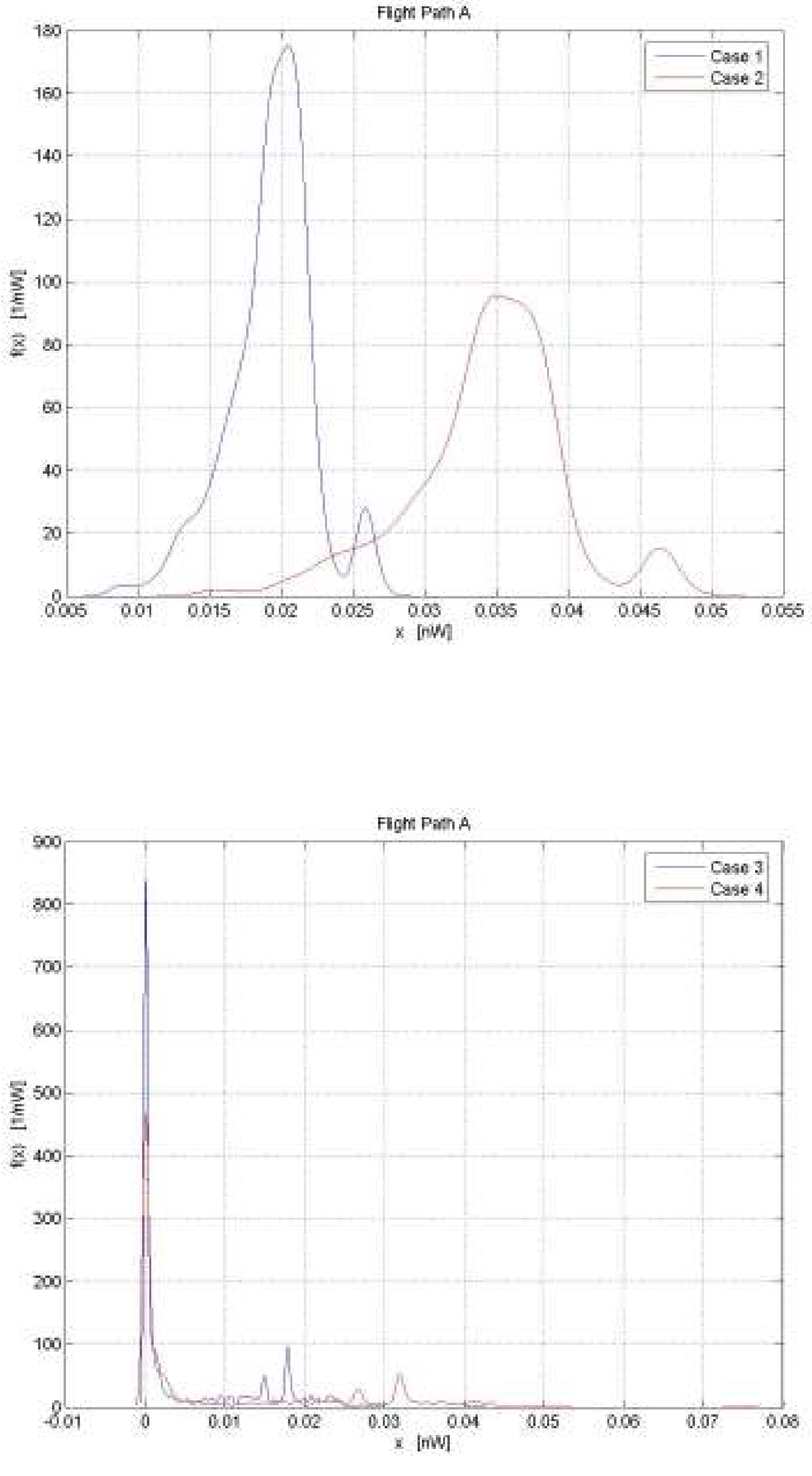

Figure 5.2: PDF for Flight Path A

The CDF for flight path B is plotted for cases 1-4 in Figure 5.3 below.

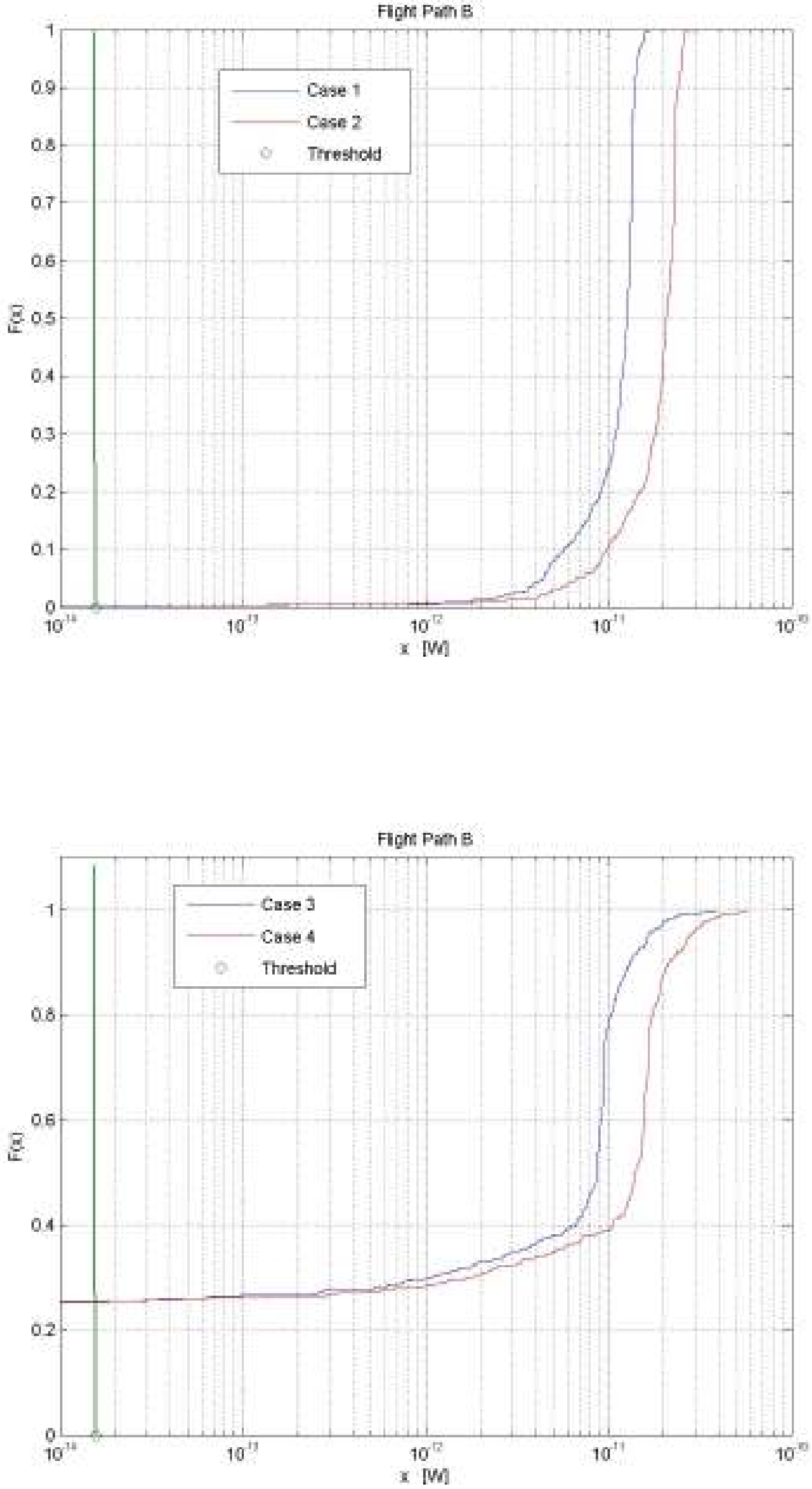

Figure 5.3: CDF for Flight Path B

The PDF for flight path B is plotted for cases 1-4 in Figure 5.4 below.

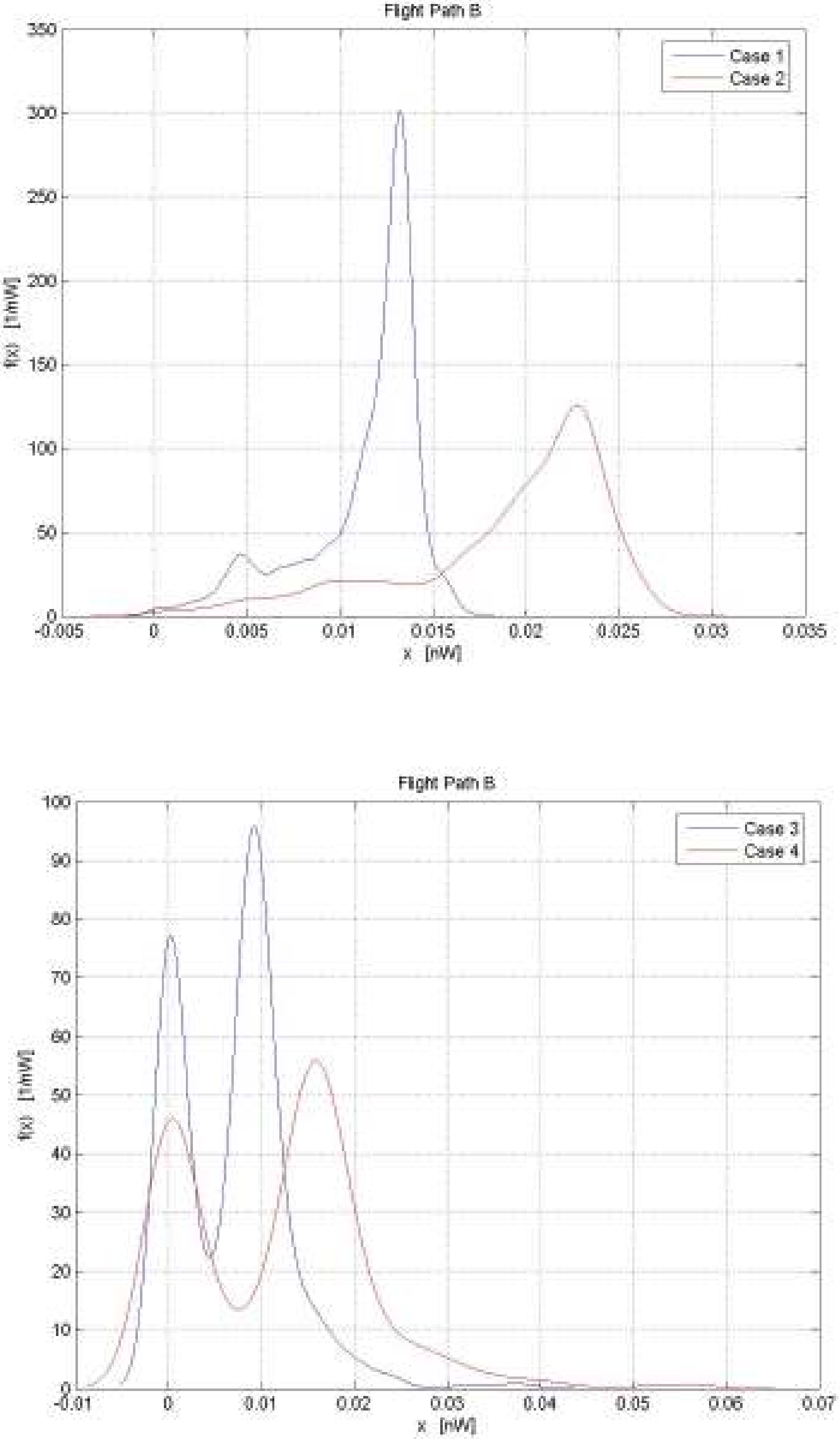

Figure 5.4: PDF for Flight Path B

The CDF for flight path C is plotted for cases 1-4 in Figure 5.5 below.

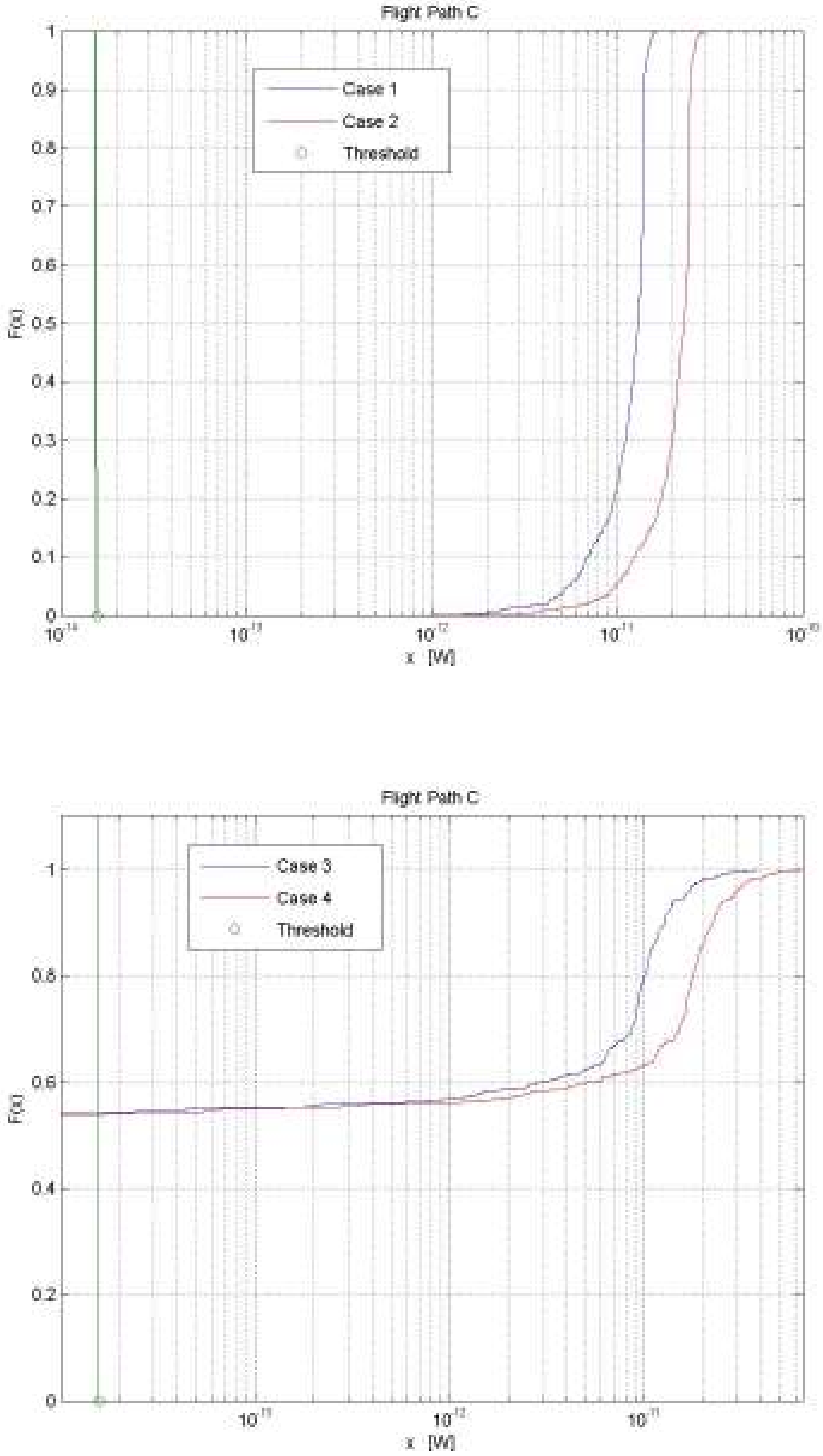

Figure 5.5: CDF for Flight Path C

The PDF for flight path C is plotted for cases 1-4 in Figure 5.6 below.

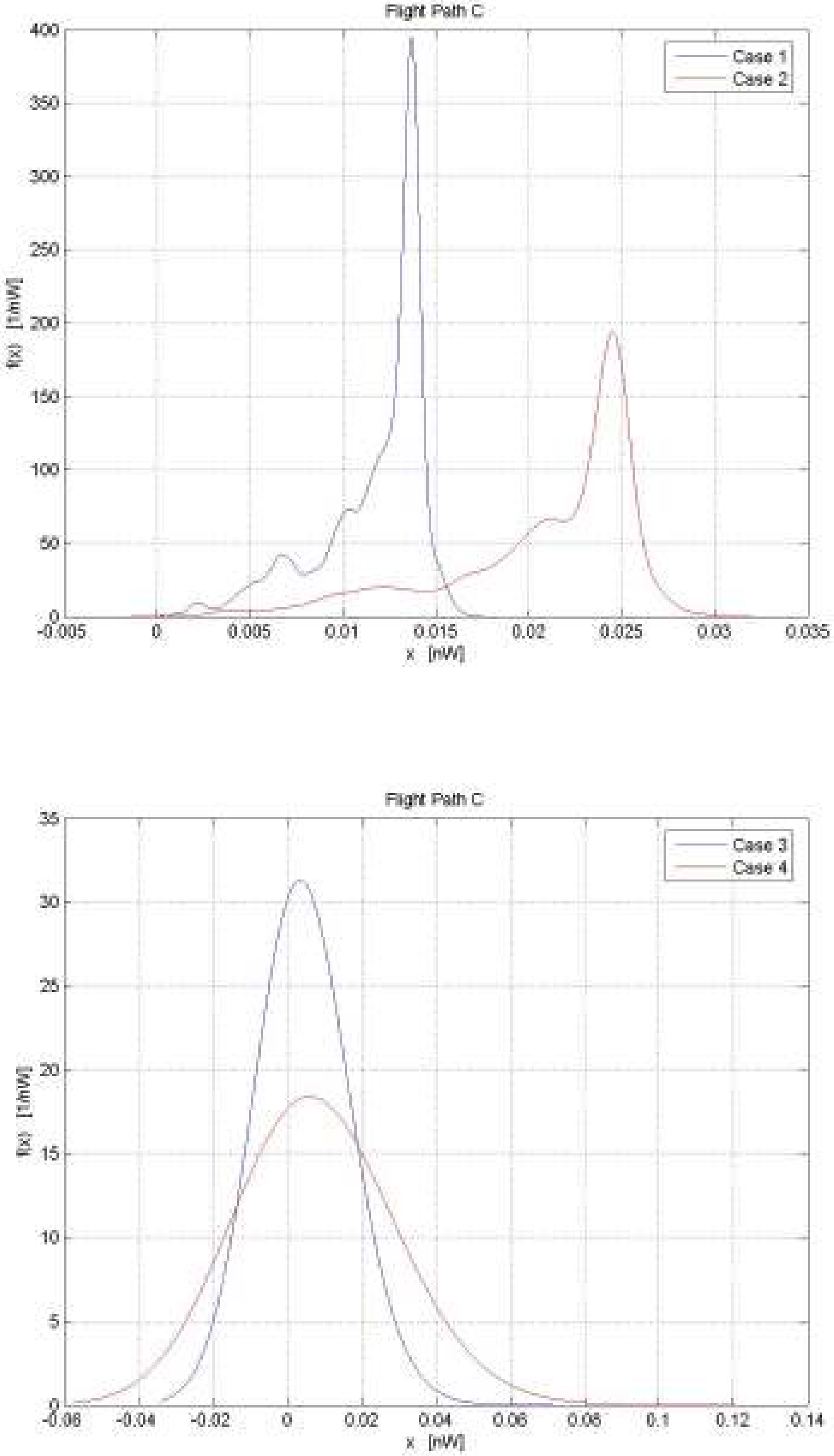

Figure 5.6: PDF for Flight Path C

CHAPTER 6 – SUMMARY & CONCLUSIONS

Since the 1950's, the U.S. military has been developing UAV technology at rates which varied depending upon the political and economic climate. Currently, the U.S. military has numerous UAV programs which cover a wide range of sizes, having weights ranging over four orders of magnitude. While numerous large UAV programs have demonstrated advanced capabilities, small UAV technology remains in the developmental stage.

Small UAV technology has the potential for extensive military and commercial development. There are many service requirements in both military and civilian spheres which could be fulfilled by small UAVs, such as biological and chemical agent detection, airport security, and communications interception. Academic, government, and commercial researchers have demonstrated the utility of small UAVs for various purposes including Homeland Security surveillance and remote sensing for law enforcement, agriculture, and anthropological research.

In order for small UAVs to step into these roles and gain clearance from the FAA to operate in civilian airspace, the reliability of the communication link must be improved. Communication links for small UAVs are adversely affected by factors such as sudden attitude changes and power limitations. These factors can lead to decreased signal strength, degraded signal quality, or complete loss of communication with the ground [3]. In addition, UAV data links are challenged by limited bandwidth.

The objective of this study was to investigate the probability of success for the line-of-sight RF link between a small UAV and its ground station. To achieve this goal, a computer program was developed, based upon the Friis Transmission Equation, to evaluate the probability of link success for planned flight paths.

In summary, the first chapter of this thesis gave a concise background of the U.S. military's UAV technology and introduced the research objective. Chapter Two covered the theory which served as the foundation for the computer program developed in this thesis. The implementation of the theory for the communication link analysis was investigated in Chapter Three. Chapter Four described the program algorithm, the flight path data which was used in the computer program simulations, and the simulation data generated by the computer program. Finally, Chapter Five presented a method for evaluating the probability of link success and results generated by the computer program for several flight paths.

Several general conclusions may be drawn from the results presented in Chapter Five. Based upon the data of Table 5.2, it may be concluded that the performance of the half-wave dipole antenna is comparable to that of the 3-element Yagi antenna for link ranges up to approximately two miles. Additionally, the data indicates that, for link ranges of over 1.5 miles, a half-wave dipole antenna may perform better than a patch antenna when mounted onboard a UAV.

The contributions of this thesis are:

- Developed a framework for a computer analysis of an airborne LOS RF communication link based upon the Friis Transmission Equation and flight path data from a commercial autopilot system. The analysis included consideration for the time-varying position and orientation of the UAV platform, the time-varying orientation (azimuth and elevation angles) of a ground station antenna for tracking purposes, the angular dependence of the antenna gains, and the angular dependence of the polarization mismatch of the link antennas.
- Introduced a method to quantify the probability of success for RF communication links of small UAVs. Here, the probability of success is defined for a particular flight path as the percentage of values of the link received power which equal or exceed the sensitivity of the link receiver. The method utilizes standard functions of the MATLAB Statistics Toolbox.

There are several possibilities for future studies based upon this thesis. They might include:

- Expanding the library of antennas and including consideration for steerable antennas onboard the UAV platform for the purpose of performing in-depth antenna tradeoff studies
- Optimizing planned flight paths for maximum probability of link success for civil and commercial applications
- Investigating the effects of signal fading due to ground multipath and/or diffraction effects on the communication link reliability

Appendix

The far-zone electric field of a half-wave dipole oriented along the *x*-axis, as shown below, will be derived here.

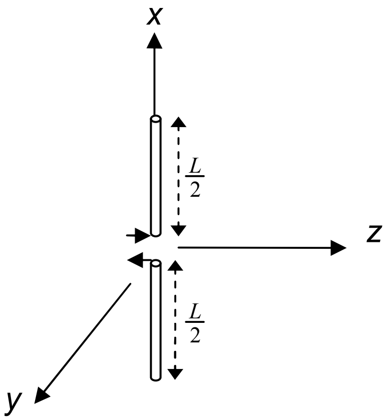

The magnetic vector potential ***A*** due to a linear electric current source **I** is given by [13]

$$\vec{A} = \frac{\mu}{4\pi} \int_C \vec{I}\left(x', y', z'\right) \frac{e^{-j\beta R}}{R} dl' \tag{A.1}$$

where the primed coordinates represent the source and *R* is the distance between the observation point and any point on the source. For the center-fed, *x*-directed half-wave dipole shown above, the vector potential is

$$\vec{A} = \frac{\mu}{4\pi} \int_{-\frac{\lambda}{4}}^{\frac{\lambda}{4}} \vec{I}\left(x'\right) \frac{e^{-j\beta R}}{R} dx' \tag{A.2}$$

The standing-wave current distribution on the center-fed half-wave dipole shown above can be approximated by [13]

$$\vec{I}\left(x\right) = I_m \sin\left[\beta\left(\tfrac{\lambda}{4} - |x|\right)\right]\hat{x} \tag{A.3}$$

for $|x| \leq \frac{\lambda}{4}$. Since the current source is directed solely along the *x*-axis, the vector pointing to the source point is simply

$$\vec{r}' = x'\hat{x} \tag{A.4}$$

Then the distance *R* given by the parallel ray approximation is [14]

$$R \approx r - \hat{r} \cdot \vec{r}' = r - x' \sin\theta \cos\phi \tag{A.5}$$

where $\hat{r}$ is the radial unit vector.

The magnetic vector potential of (A.2) reduces to

$$\vec{A} = \hat{x}\mu I_m \frac{e^{-j\beta r}}{4\pi r} \int_{-\frac{\lambda}{4}}^{\frac{\lambda}{4}} \sin\left[\beta\left(\tfrac{\lambda}{4} - |x'|\right)\right] e^{j\beta x' \sin\theta\cos\phi} dx' \tag{A.6}$$

The integral of (A.6) must be broken into two pieces, or

$$\vec{A} = \hat{x}\mu I_m \frac{e^{-j\beta r}}{4\pi r} \left\{ \int_{-\frac{\lambda}{4}}^{0} \sin\left[\frac{\pi}{2} + \beta x'\right] e^{j\beta x' \sin\theta\cos\phi} dx' + \int_{0}^{\frac{\lambda}{4}} \sin\left[\frac{\pi}{2} - \beta x'\right] e^{j\beta x' \sin\theta\cos\phi} dx' \right\} \tag{A.7}$$

The solution for these integrals has been tabulated in a table of integrals, and is given by [14]

$$\int \sin(a + bx) e^{cx} dx = \frac{e^{cx}}{b^2 + c^2}\left[c \cdot \sin(a + bx) - b \cdot \cos(a + bx)\right] \tag{A.8}$$

where the substitutions $a = \frac{\pi}{2}$, $b = \beta$, and $c = j\beta \sin\theta\cos\phi$ are made. After evaluation and simplification, the integrals of (A.7) reduce to

$$\int_{-\frac{\lambda}{4}}^{0} \sin\left[\frac{\pi}{2} + \beta x'\right] e^{j\beta x' \sin\theta\cos\phi} dx' = \frac{1}{\beta\left(1 - \sin^2\theta\cos^2\phi\right)} \left(j\sin\theta\cos\phi + e^{-j\frac{\pi}{2}\sin\theta\cos\phi} \right) \tag{A.9}$$

and

$$\int_{0}^{\frac{\lambda}{4}} \sin\left[\frac{\pi}{2} - \beta x'\right] e^{j\beta x' \sin\theta\cos\phi} dx' = \frac{1}{\beta\left(1 - \sin^2\theta\cos^2\phi\right)} \left(-j\sin\theta\cos\phi + e^{j\frac{\pi}{2}\sin\theta\cos\phi} \right) \tag{A.10}$$

After collecting terms and applying Euler's identity, the vector potential reduces to

$$\vec{A}=\hat{x}\mu\frac{e^{-j\beta r}}{4\pi r}\frac{2I_m}{\left(1-\sin^2\theta\cos^2\phi\right)}\cos\left(\frac{\pi}{2}\sin\theta\cos\phi\right) \tag{A.11}$$

The far-zone electric field radiated by the antenna is given by [14]

$$\vec{E}_{ff}=-j\omega\vec{A}-\left(-j\omega\vec{A}\cdot\hat{r}\right)\hat{r} \tag{A.12}$$

Applying (A.12) to (A.11) yields

$$\vec{E}_{ff}=-j\eta\frac{e^{-j\beta r}}{4\pi r}\frac{2I_m}{\left(1-\sin^2\theta\cos^2\phi\right)}\cos\left(\frac{\pi}{2}\sin\theta\cos\phi\right)\left[\hat{\theta}\cos\theta\cos\phi-\hat{\phi}\sin\phi\right] \tag{A.13}$$

References

[1] “The U.S. Air Force Remotely Piloted Aircraft and Unmanned Aerial Vehicle Strategic Vision”, 2005, 34 pages.

[2] “Unmanned Aircraft Systems Roadmap 2005-2030”, United States Department of Defense, August 2005.

[3] “Unmanned Aerial Vehicles Roadmap 2002”, United States Department of Defense, December 2002, 195 pages.

[4] “Homeland Security: Unmanned Aerial Vehicles and Border Surveillance”, CRS Report for Congress, February 2005, 6 pages.

[5] UAV Collaborative, http://www.uavapplications.org/projects/homeland_1.html

[6] H. Eisenbeiss, “A Mini Unmanned Aerial Vehicle (UAV): System Overview and Image Acquisition”, International Workshop on Processing and Visualization Using High-Resolution Imagery, Pitsanulok, Thailand, November 2004.

[7] D. Murphy and J. Cycon, “Applications for mini VTOL UAV for law enforcement”, Space and Naval Warfare Systems Center, San Diego, California, 1998.

[8] L.F. Johnson, S. Herwitz, S. Dunagan, B. Lobitz, D. Sullivan, R. Slye, “Collection of Ultra High Spatial and Spectral Resolution Image Data over California Vineyards with a Small UAV”, Proceedings, Int’l Symposium on Remote Sensing of Environment, 2003.

[9] J. Tindall, “Deconvolution of Plant Type(s) for Homeland Security Enforcement Using Remote Sensing on a UAV Collection Platform”, Homeland Security Affairs, vol.2, article 4, April 2006.

[10] C. Chen et al, “System Requirements for a Deep Space Optical Transceiver”, Jet Propulsion Laboratory.

[11] R. E. Collin, *Antennas and Radiowave Propagation*, USA: McGraw-Hill, Inc., 1985.

[12] L. W. Couch, *Digital and Analog Communication Systems*, 6th Ed. Upper Saddle River, New Jersey: Prentice Hall, 2001.

[13] C. A. Balanis, *Antenna Theory: Analysis and Design*, 2nd Ed. New York: John Wiley & Sons, Inc., 1997.

[14] W. L. Stutzman and G. A. Thiele, *Antenna Theory and Design*, 2nd Ed. USA: John Wiley & Sons, Inc., 1998.

[15] C. A. Balanis, *Advanced Engineering Electromagnetics*, USA: John Wiley & Sons, Inc., 1989.

[16] K. Lambeck, *Geophysical Geodesy*, USA; Oxford University Press, 1988.

[17] C. E. Ewing and M. M. Mitchell, *Introduction to Geodesy*, New York; American Elsevier Publishing Co., Inc., 1970.

[18] The Defense Mapping Agency Technical Manual 8358.1, 1st Ed. Fairfax, Virginia; The Defense Mapping Agency, 1990.

[19] National Imagery and Mapping Agency *World Geodetic System 1984 (WGS 84) – Its Definition and Relationships with Local Geodetic Systems*. 3rd Ed. Washington, DC; National Imagery and Mapping Agency, 1997.

[20] T. Soler and L. D. Hothem, "Coordinate Systems Used in Geodesy: Basic Definitions and Concepts", Journal of Surveying Engineering, vol. 114, no. 2, May 1988.

[21] E. L. Houghton and A. E. Brock, *Aerodynamics for Engineering Students*, 2nd Ed. London; Edward Arnold (Publishers) Ltd, 1970.

[22] D. T. Greenwood, *Principles of Dynamics*, Englewood Cliffs, New Jersey: Prentice-Hall, Inc., 1987.

[23] E. W. Weisstein, "Euler Angles", From *MathWorld* – A Wolfram Web Resource, http://mathworld.wolfram.com/EulerAngles.html

[24] B. Vaglienti, R. Hoag, M. Niculescu, Piccolo System User's Guide, version 1.3.2, Hood River, Oregon; Cloud Cap Technology, 2006.

[25] K. R. Carver and J. W. Mink, "Microstrip Antenna Technology", IEEE Trans. Antennas Propaga., vol. AP-29, no. 1, pp. 2-24, Jan. 1981.

[26] UK Aerial Robotics Team, http://www.engr.uky.edu/idea/wiki/doku.php?id=projects:active:pax:public:default

[27] B. Vaglienti and Ross Hoag, "A highly integrated UAV avionics system", Hood River, Oregon; Cloud Cap Technology, 2001.

[28] B. Vaglienti, “Communications for the Piccolo avionics”, version 1.3.2, Hood River, Oregon; Cloud Cap Technology, 2006.

[29] Peebles, P. Z., *Probability, Random Variables, and Random Signal Principles*, 4th Ed. New Delhi, India: Tata McGraw-Hill, 2002.

[30] W. Smith and S. Smith, “Technologies for Unmanned Aerial Vehicle Reliability in Changing Environments”, 2006.

[31] MATLAB Help.

Vita

Personal

Birth Place and Date: 7th July 1978, Lancaster, Pennsylvania, USA

Education

Bachelor of Science (B.S.) in Electrical Engineering, May 2006
Department of Electrical & Computer Engineering
University of Kentucky, Lexington, KY, USA

Work Experience

Graduate Research Assistant: August 2005 – July 2006
Department of Electrical & Computer Engineering
University of Kentucky, Lexington, KY

Research Assistant: Summer 2002, Summer 2003, Summer 2004
Department of Electrical & Computer Engineering
University of Kentucky, Lexington, KY

Laboratory Assistant: August 2003 – May 2005
Physics & Astronomy Department
University of Kentucky, Lexington, KY

Honors

Charles LeGeyt Fortescue Graduate Scholarship, IEEE Awards, 2006-2007
Lexmark Fellowship, University of Kentucky College of Engineering, 2006-2007
Eta Kappa Nu, Electrical Engineering Honor Society, Lifetime member
Tau Beta Pi, Engineering Honor Society, Lifetime member
Oswald Research and Creativity Program, Physical & Engineering Sciences, 2nd place, 19 April 2005

Publications

Zhi Chen, Pangling Ong, Alicia Kay Mylin, and Vijay Singh, "Direct evidence of multiple vibrational excitation for the Si-H/D bond breaking in metal-oxide-semiconductor transistors", *Applied Physics Letters*, vol. 81, no. 17, October 21, 2002, p 3278.